Fracture Behavior of Mortar–Aggregate Interfaces in Concrete

by

Brian Hearing

Submitted to the Department of Civil and Environmental Engineering
in partial fulfillment of the requirements for the degree of

Master of Science in Civil and Environmental Engineering

at the

MASSACHUSETTS INSTITUTE OF TECHNOLOGY

January 1997
[February 1997]

Author ....
Department of Civil and Environmental Engineering
January 17, 1997

Certified by ....
Oral Büyüköztürk
Professor, Department of Civil and Environmental Engineering
Thesis Supervisor

Accepted by ....
Joseph M. Sussman
Chairman, Departmental Committee on Graduate Students

Fracture Behavior of Mortar–Aggregate Interfaces in Concrete

by

Brian Hearing

Submitted to the Department of Civil and Environmental Engineering
on January 17, 1997, in partial fulfillment of the
requirements for the degree of
Master of Science in Civil and Environmental Engineering

Abstract

In this research, novel experimental and analytical methodology based fracture mechanics studies are used to study interfacial fracture in concrete composites. First, interfacial slab inclusion specimens are tested in both mode I and mixed mode loading to investigate interfacial fracture toughness K_i, energy release rate G_i, and specimen load–displacement behavior. A Hillerborg–type cohesive force analytical model is used to test different strain softening models to simulate the interfacial behavior of these specimens during fracture. While bilinear strain–softening models have been shown to successfully model constituent materials, a linear model is shown to best model interfacial strain–softening behavior. Next, physical circular inclusion specimens are tested with various mortar strengths and granite inclusions with both smooth and sandblasted surface roughness. Influences of interfacial parameters on the ductility of the composite specimens are investigated. The cohesive model is extended to simulate the circular inclusion specimens using the results of a finite element investigation into the stress intensities created by a crack propagating around a circular inclusion. A parametric study is conducted to investigate the influence of relative fracture parameters of the interface, mortar, and aggregate on the ductility of the specimen. Based on the behavior and knowledge developed from the composite studies, the ductility of normal and high strength real concrete is investigated for various aggregate types, volume fractions, and sizes. An analytical procedure is conducted to quantitatively assess the influence of these parameters on the ductility of the concrete. A constituent property based energy formula is developed to predict the fracture energy of real concrete. These results are used to make practical recommendations for manufacturing high performance concretes with desired properties.

Thesis Supervisor: Oral Büyüköztürk
Title: Professor, Department of Civil and Environmental Engineering

Acknowledgments

I would like to thank Professor Oral Büyüköztürk for his guidance and support in the completion of this thesis. His diligence and perseverance have provided an excellent example to me and others under his supervision.

This research was supported by the National Science Foundation through Grant Number MSS-9313062. I would like to thank Dr. John Scalzi for his support in this program. I would also like to thank W. R. Grace and Boston Sand and Gravel for providing the materials used in this project.

Contents

List of Figures

List of Tables

Chapter 1

Introduction

Use of cementituous materials can be traced back to the days of Greek, Roman, and even earlier civilizations. What is commonly referred to now as 'concrete' began development and achieved widespread use around the early part of the nineteenth century. It was the development of portland cement and consistent, reliable production methods that signaled the institutionalization of concrete as a construction material. By 1910 the German Committee for Reinforced Concrete, the Austrian Concrete Committee, the American Concrete Institute, and the British Cement Association had been established.

The latter part of the twentieth century has also experienced the development of high–strength concrete. Many significant shortfalls of normal strength concrete can be overcome with high–strength concrete. Cross–sectional areas of columns and beams can be reduced. High early strengths can shorten concreting cycles and construction times. Higher Young's modulus can result in less elasticity and less creep. High–strength concrete is also more durable with respect to aggressive environments and freeze–thaw cycles.

Today, a massive amount of research and theoretical devleopments have necessitated a simplified approach to the use of concrete as a construction material. Common codes in use today include the American Concrete Institute's Standard Building Code and the British Cement Association's BS 8110. However, it is the development of these simplified national and global design methods that distance the designing engineer from a true knowledge of the material behavior of local concretes. Properties and characteristics can vary according to locally available materials and production techniques. Consequently, the development of high–strength concretes has been met with trepidation from the construction industry and widespread use has still not been achieved. For this reason, to give the engineer an understanding of the behavior of local concretes it is necessary to characterize engineering behavior through the relative properties of the constituent materials of the concrete.

The structure of concrete can be described as a nonhomogeneous union of different materials with different mechanical properties. The relationships between these materials can affect the performance of concrete in sometimes drastically different ways. Characterization of a composite material's properties based on the properties of its constituents requires an advanced understanding of the interaction and role of each constituent in the behavior of the global system. This work contributes to the basic understanding of the performance and failure behavior of concrete, both normal and high–strength.

1.1 Background

1.1.1 Development of High–Strength Concrete

It is currently held that high–strength concrete (HSC) is defined as any concrete with compressive strength of over 10,000 psi (69 MPa). However, only 17 years ago in a Chicago convention of the American Concrete Institute it was defined as any concrete with compressive strength of over 6,000 psi (41 MPa). Clearly, research in this area has rapidly improved the production of concrete with higher strengths. It is now common to achieve strengths of up to 80 MPa on the construction site and strengths up to 107 MPa in the laboratory. The pace of development of higher strength concretes has accelerated and will continue to increase into the next century.

Two methods are commonly used to produce high–strength concrete. First, lowering the water/cement ratio along with improved quality of constituent materials can increase strength; however, results are inconsistent and the use of superior materials may increase production costs. A second method employs chemical admixtures such as superplasticizers, fly ash, and silica fume. Chemical retarders are used to retard the setting time and high–range water reducers are added to improve workability. The use of silica fume has been widely accepted as an efficient admixture for high–strength concrete mixes [44].

Silica fume is a by–product that has received much attention by the concrete construction and manufacturing industry. It is a pozzolanic material resulting from the use of high–purity quartz with coal in the electric–arc furnace in the production of silicon and ferrosilicon alloys. It is an ideal cement replacement because of the fine spherical particles of silicon dioxide and a higher relative surface area to particle weight ratio. It has been successfully used in many applications where an increased strength and reduced permeability concrete is needed.

One of the aims of concrete mix designs is to produce concrete with good workability while maintaining strength and other desired properties. Universally accepted methods for mix proportioning normal strength concrete include the American Concrete Institute's recommended practice for selecting proportions [1]. However, there are no quantitative guidelines for the mix design of high strength concrete in widespread use. Frequently, empirical mix proportions derived from the local availability of materials is the basis for many commercial high strength concretes. As a result, consistency and reliability can vary in different geographical areas.

The use of high–strength concrete has increased dramatically in the last few decades. The increased use has demonstrated many benefits of HSC as a construction material; however, it has also revealed some undesirable characteristics. Most notably, major problems include a low relative tensile strength and a lower ductility. The low relative tensile strength is a concern for the designer when HSC is to be used in flexural members and special applications like plates and shells. Consideration of the lower ductility of HSC is also important in these members, but presents an additional obstruction for widespread use in fracture critical members. Furthermore, lack of ductility presents a safety problem, especially in inhabited structures, because of

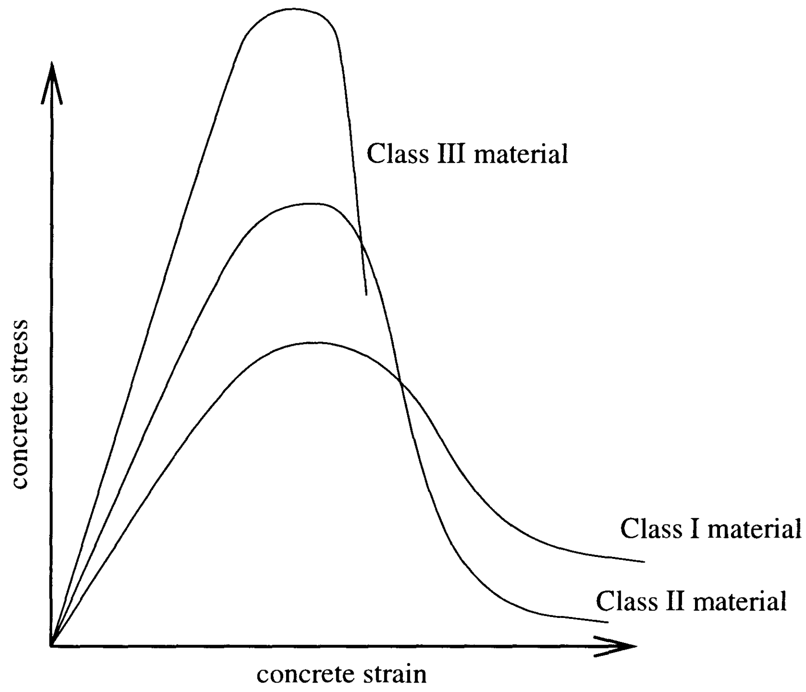

Figure 1-1: Mechanical stress–strain response of different concretes

the brittle nature of failure. This problem is a major motivation for the development of high–performance concretes with improved ductility characteristics.

1.1.2 Mechanical Behavior of Concrete

Knowledge of the mechanical behavior of concrete is necessary to develop analytical and design procedures for use as an engineering material. Concretes can usually be categorized into three classes by their stress–strain response to uniaxial compression. Figure 1-1 illustrates the differences between classifications. Class I materials exhibit nonlinear behavior at an ultimate load, followed by a long post–peak strain softening curve. Class II materials exhibit linear behavior at first followed by a steeper post–peak portion with a relatively shorter length. Class III materials have a steeper post–peak descent and are often characterized by brittle and explosive failure.

Concretes with special additives like fiber reinforcements can achieve the post–peak ductility associated with Class I concetes. Normal–strength concretes without special additives, including all concretes under 41.0 MPa (6,000 psi), are generally considered a Class II material. Concretes with compressive strengths greater than 41.0 MPa begin to approach a Class III–type material and often exhibit more brittle failure. Strengths over 79.0 MPa (11,500 psi) fail in a violently explosive manner; it is this behavior that is the most significant problem with high–strength concrete. The change in failure behavior from ductile to brittle is the product of differences between the damage processes of normal and high strength concretes.

1.1.3 Damage Processes in Concrete

It is generally agreed that the damage process in failing concrete is initiated by microcracks far ahead of a propagating crack which, with additional load, ultimately link together to form continuous cracks [26, 48, 10, 39, 52]. The development of bond cracks at the mortar-aggregate interfaces is often cited as the initiator of microcracks; it has been shown that interfacial zones are the "weak link" in crack formation [10, 11, 58]. Therefore, interest in the study of mortar-aggregate interfaces has increased with the need for the development of cementitious materials with improved performance.

Mortar–aggregate interfaces, which can be so weak as to represent discontinuities, are often regarded as the "weak link" in the structure of normal–strength concrete. In high–strength concrete, however, superior bond strength is acheived through a densification of this interface and the "weak link" theory may no longer be valid [55]. This additional interface strength may be stronger than the aggregate, depending on relative fracture energies, aggregate shape, and a variety of additional factors. At this point the interface may no longer play a role in the fracture processes of high–strength concrete and the crack will likely propagate through the aggregate with reduced crack–trapping effects by the aggregate, resulting in brittle failure.

Mortar–aggregate interfacial zones are defined as the layer which includes all natural and artificial anomalities in the vicinity of the surface of the aggregate. Many feel that the interfacial zone is a theoretical concept in that it is a two–dimensional boundary between two different materials [36]. Under this theory limited properties such as bond strength and fracture toughness can be assigned to the interface; however, this is not sufficient for a description of the mechanical behavior and influence of the interface on crack propagation in this area. This study will consider the "interface" as the two dimensional boundary and the thin layer of mortar matrix surrounding it; this layer is composed of several layers of different minerals that are bled out from the mortar. This definition of interface allows a more accurate description of mechanical behavior to be assessed; namely, constitutive properties such as strain–softening behavior and modulus of elasticity can now be defined.

Many factors affect the microstructure of the interface, including the mixing rate, admixtures, water content, and material properties of the cement and aggregate. Perhaps the most influential admixture concerning interfacial zones is silica fume, which has been shown to densify the interface by dispersing water more closely to the aggregate, thus improving hydration and an increase in bond strength [55]. The fine particles of silica fume have also been shown to be helpful in improving pore refinement and consistency.

1.2 Motivation for Research

Performance of concrete is not only measured by mechanical properties but also by failure behavior. The failing process of most materials, including concrete, can be characterized by fracture mechanics, a mechanical theory that describes the complex processes of a propagating crack. The fracture properties of concrete are closely related to its mechanical properties and are influenced by its chemical constituents and micro-, mezo- and macrostructures [49].

Failure processes and mechanical properties of concrete depend on various internal structures and porosities found in the mortar matrix. Fracture processes in this matrix are influenced by nonhomogeneous particles and voids in a scale of nanometers. Sands, fine aggregates and rough aggregates can contribute to nonhomogeneities in the scale of micrometers to millimeters, as shown in Figure 1-2. At this scale interfacial cracks and millimeter–sized 'weak zones' surrounding these interfaces are considered major defects in the material structure of concrete. It is generally agreed that at this scale these interfacial cracks dictate the stability of fracture processes in concrete.

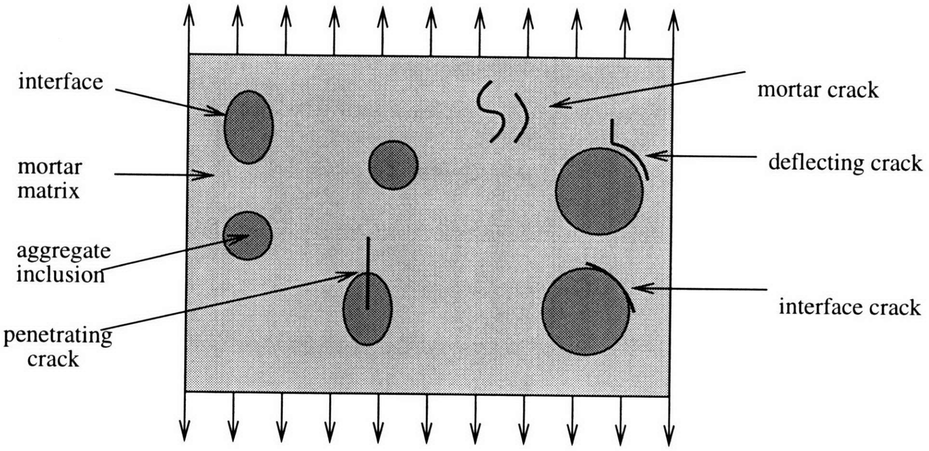

Figure 1-2: Two–phase concrete composite cracking modes

The shift towards more brittle failure in high–strength concretes is caused by densification of the interfacial layer between the mortar matrix and the aggregate particles, as shown in Figure 1-3. In normal strength concretes, the interfacial layer is usually weaker than the strength of the aggregate. Consequently, during the fracture process of normal strength concrete these interfaces fail far ahead of a propagating crack, enlarging the damage process zone and diverting the course of the crack. In higher strength concretes, the mortar matrix becomes stronger and increases the strength of the interfacial layer. When a crack approaches an interfacial region in high strength concrete the interface may maintain integrity, and the damage process zone may be significantly reduced in size. The propagating crack often is not diverted and failure can occur extremely fast and brittle.

Improving the fracture behavior of higher strength concretes is the focus of much research in the construction materials industry. It is commonly agreed that interfacial densification is the leading cause of brittleness in high–strength concrete. Therefore, the development of high–strength concrete with improved fracture toughness and ductility requires a fundamental knowledge of the behavior of mortar–aggregate interfaces. It is the aim of this research to contribute to the fundamental understanding of mortar–aggregate interfaces and to assess their influence on the performance of high–strength concretes. Specifically, the research will concentrate on a rigid definition and

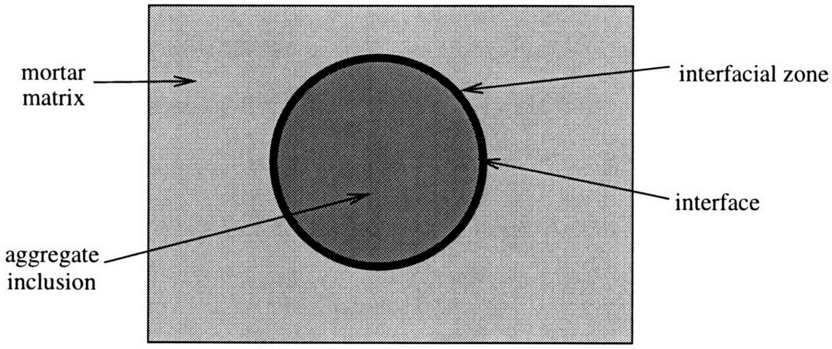

Figure 1-3: Two–phase concrete composite interface and interfacial zone

assessment of the role that the interface plays in influencing the fracture behavior of concrete. To assess this influence, significant knowledge must be gained about the behavior of the interfacial region. To date, it is known that several parameters affect fracture in the interfacial region:

- $D = \frac{\Gamma_i}{\Gamma_a}$ The ratio of interfacial fracture energy to the fracture energy of the aggregate; it has been shown to have strong influence on the behavior of a composite [35]. Ratios of D less than a critical value will influence the crack to deflect into the interface; greater values will force the crack to penetrate into the aggregate. It is this ratio that can often drastically influence ductility, especially in high–strength concrete.

- l_{ch} The characteristic length of the concrete and its constituents. It is a measure of the ultimate deformation a cohesive bond across a propagating crack can sustain before failure. It may be the most well–known quantitative measure of ductility used today [31, 33].

- $F = \frac{\Gamma_i}{\Gamma_m}$ The ratio of interfacial fracture energy to the fracture energy of the mortar. This ratio has been shown to influence deflection of cracks out of the interface and into the mortar, thus increasing crack length and perhaps increasing concrete ductility [38].

- V_f The aggregate volume fraction. This fraction will influence the global fracture energy of the concrete and may alter ductility.

- *MSA* The maximum aggregate size. This measure, in conjunction with the aggregate volume fraction, may also alter the global material fracture energy of the concrete and consequently its ductility.

An advanced understanding of the interaction and influence of these parameters on the global ductility of concrete, both normal strength and high strength, is necessary in designing high–performance concretes with improved engineering qualities. Quantitative studies of these parameters can offer great potential in understanding the global concrete behavior, leading to a knowledgeable development of advanced materials.

1.3 Objectives and Approach

This research presents a fundamental study of the influence mortar–aggregate interfaces have on the fracture behavior and performance of concrete. Specifically, the objectives of this research are:

1. To study and characterize the fracture behavior of mortar–aggregate interfaces in concrete through interfacial fracture experiments and analytical models.
2. To experimentally and analytically investigate the influence interface fracture parameters have on localized fracture of concrete.
3. To establish, through analysis and experimentation, design guidelines for the development of concretes with desired fracture behavior and ductility.

Tests and analyses on two types of two–phase composite models provide data on the interfacial fracture properties and effects on local cracking propagation. A sandwich test specimen is used to determine the mechanical constitutive behavior of interfaces during fracture. A circular inclusion test specimen is then used to simulate crack propagation around an inclusion in concrete. Test parameters include aggregate type, surface roughness, and mortar strength. Numerical analyses based on fracture mechanics concepts are performed to simulate the cracking scenarios. Numerical analyses based on fracture mechanics concepts are performed to develop code–type formulation of concrete ductility based on constituent parameters.

The results of these studies are used in a parametric investigation of real high–performance concrete design. Test parameters include aggregate type and size, volume fraction, and mortar strength. Results are compared to previously tested models and conclusions with respect to design specification are drawn. This research provides valuable design guidelines for high–performance cementitious materials, thus enabling the application of high–performance concretes in a wider variety of uses. Figure 1-4 shows the research approach for the design of concrete based on fracture properties and ductility.

1.4 Report Organization

The organization of this report is as follows:

Chapter 1 has provided the general background and motivation of this work. The objectives and organization are presented.

Chapter 2 reviews pertinent literature on fracture in concrete and describes the fracture process of concrete in the interfacial zone. Interfacial properties influencing the performance of concrete are also discussed.

Chapter 3 reviews the interface fracture mechanics concepts useful for mortar–aggregate interfaces as a theoretical basis for analytical models.

Chapter 4 discusses the theory behind cohesive fracture propagation in the interfacial region and presents experimentation to investigate strain–softening behavior of the interface. A computational simulation of cohesive fracture is created and the results of an investigation into the strain–softening behavior of the interface are discussed. Interfacial constitutive relationships are given for a variety of interfaces during crack propagation.

Chapter 5 details an experimental and analytical investigation with beam specimens containing circular aggregate inclusions. The results of a finite element investigation

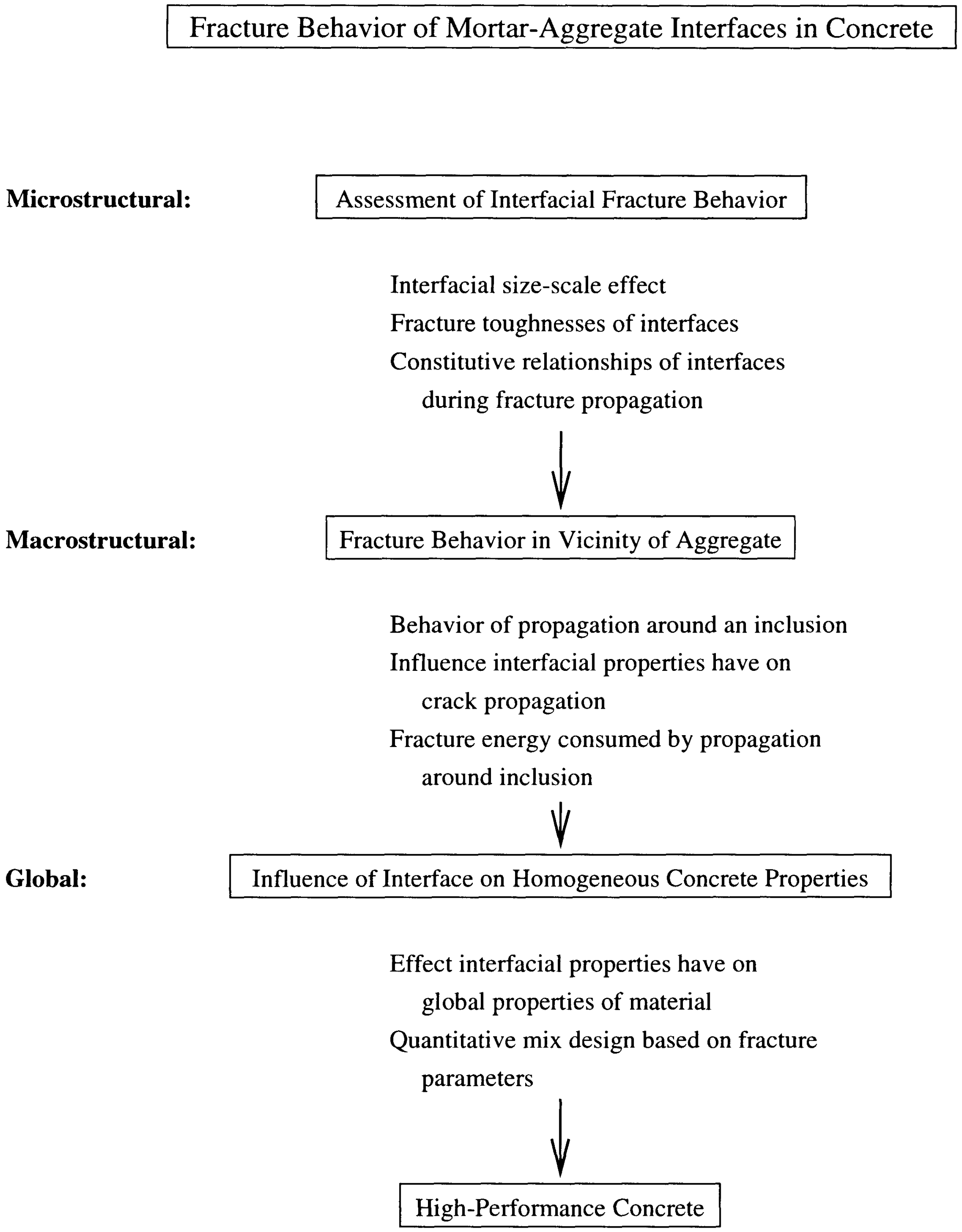

Figure 1-4: Mechanical stress–strain response of different concretes

are employed into a simulation of fracture around a circular aggregate inclusion. The results are verified by experiment through physical specimens.

Chapter 6 describes the experimental investigation into the design of high performance concretes through testing of real concrete samples.

Chapter 7 summarizes the results of this work and lists conclusions and recommendations for future work.

Chapter 2

Review of Fracture in Concrete

2.1 Introduction

Cementituous constituents can be classified into paste, mortar, and concrete categories. 'Paste' is defined as the mixture of cement and water, 'mortar' is the mixture of small aggregate, such as sand, with paste, and 'concrete' is the composite created when a larger aggregate, such as gravel or stones, is mixed with mortar. The cement found in these constituents hydrates when mixed with water, forming a hard matrix after curing. While in a liquid form, however, this paste fills the space among aggregates, both large and small, and bonds them together to form mortar or concrete. In addition, a variety of admixtures are used with concrete to improve global behavior, both wet and dry.

During the curing and hardening phases of the hydration process a loss of moisture occurs in the cement paste, causing shrinkage. Shrinkage is a major cause of weak tensile strengths found in concrete, and is also the cause of many internal flaws and cracks that exist in concrete prior to loading. These flaws govern the mechanical behavior of the global concrete material as the flaws initiate and propagate cracks during the application of stresses. Mechanical responses are influenced by the fracture processes of these flaws under loading.

The stress–displacement relationship for concrete subjected to uniaxial tension has been divided into four stages based on initiation and propagation of internal cracks and flaws [49]. The first stage includes all loads less than 30% of the peak load; initiation of internal cracks is negligible during this first stage. The second stage spans all loads from the first stage to less than 80% of the peak load. The internal cracks initiate and propagate during this stage; these cracks are generally isolated and randomly distributed. The third stage includes loads over 80% and up to the peak load. At this point macrocracks and flaws begin to link into large, continuous propagating cracks. This phenomenon is known as *damage localization* or *strain localization*. The large cracks propagate only when the load increases, up until the peak load. At this loading point the crack length is referred to as the critical crack length. After the peak load is applied major cracks continue to propagate even though the load may decrease. The tensile strain of the material within the damage zone increases while stress relaxation may occur in material outside this area.

A similar characterization has been reported where the distribution of compressive strain was uniform over the specimen up to approximately 80% of peak load [47]. This method of describing the damage process indicates that internal cracking of up to 80% of the peak load is more or less random and uniform. Examination of the distribution of internal cracks in the tested specimens confirm that strain localization usually appears only after 80% of the peak load has been applied.

Since it has been concluded that the fracture behavior of concrete can be characterized by the phenomemon of strain localization, permitting the use of fracture mechanics to describe damage processes in concrete [49]. The argument stems from the observation that a localized damage band can be physically simulated by a crack; it was therefore concluded that the presence of the strain localization allows the use of fracture mechanics to describe failure of concrete on a macroscopic level. Furthermore, since the damage zone of high–strength concrete is relatively smaller than in normal–strength concrete and the damage band is physically similar to a crack in brittle materials, it was concluded that fracture mechanics is also be applicable to high–strength concrete.

2.2 Influences on the Fracture Behavior of Concrete

A list of influences on fracture in concrete has been developed [16]. It was concluded that the number, location, and extent of pre–existing cracks depend mainly on:

- type of cement;
- mineralogical nature of aggregate;
- geometry of aggregate;
- water/cement ratio;
- curing conditions.

It was also concluded that the evolution of pre–existing cracks under loading depends mainly on:

- aggregate/matrix stiffness ratio;
- type of matrix–aggregate bond;
- percentage of voids in the matrix.

Mechanical damage of cementitious materials reduces both the load resistance and the stiffness of the material. A useful quantitative approximation of these two effects are embodied in an analytical approach termed the *strain softening* model. This analytical model depicts the Young's modulus and the maximum allowable stress of the material as a decreasing function of the number of loading cycles. For example, consider the concrete specimen illustrated by Carpinteri [12], shown in Figure 2-1. The stress vs. strain envelope of the material under cyclic loading describes the strain–softening behavior of the material as a function of loading cycles. The same behavior is found in concrete specimens tested in tension with monotonic strain variation by using a strain–controlled testing machine. For this reason, a decrease in the elastic modulus and load relaxation in material in the vicinity of a crack tip can be expected.

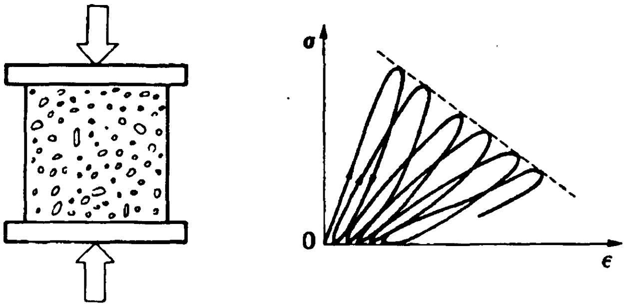

Figure 2-1: Concrete specimen subjected to repeated compression, as considered by Carpinteri (1986)

A strain localization occurs at the crack tip during crack formation, localizing the damage zone as the loading capacity of the material at the crack tip decreases. While this material within the fracture process zone softens, the stress and strain behavior of material outside the fracture zone remains in a proportional manner like undamaged concrete. As a result, strains accumulate in the fracture zone while the remaining part of the body unloads.

More precisely, when a concrete specimen is tested in uniaxial tension, damage is assumed to occur in a fracture zone as the strain exceeds the strain capacity. By observing tensile tests on concrete specimens, it can be shown that damage zone increasingly localizes with decreasing load capacity [12]. Stresses at this softening stage will be a softening function of the width of this fracture zone, independent of the geometry of the structure; it is from this theory that size effects in fracture mechanics are derived.

The softening behavior of stresses at the crack tip as unstable fracture begins is an important influence on the performance of the material during the failure process. Consider the stress vs. strain diagram of a material given in Figure 2-2. The area under the σ vs. ϵ curve represents the energy dissipated per unit area, having the dimensions of surface energy. How this energy is dissipated as a function of the crack opening displacement can influence the behavior of the material during fracture. It is a key element in the measurement of the ductility of a material, in that materials with a

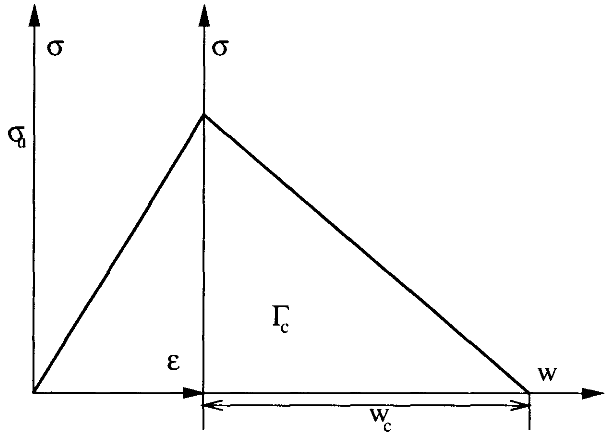

Figure 2-2: Stress–strain and stress–displacement constitutive laws

larger critical crack opening displacement w_c will exhibit greater ductility. Analytical models using various constitutive relations to simulate this strain–softening behavior appear later in this report.

2.3 Microcracking in Concrete

Concrete is often considered a heterogeneous material in engineering design and construction, yet is in reality a composite consisting of mortar matrix and aggregate inclusion phases. Upon closer inspection, voids are apparent, as the cement paste is actually a mixture of different types of crystalline structures at various degrees of hydration with trapped and entrained air voids. Most researchers simplify concrete as a two–phase composite consisting of mortar and aggregate; to complete the model, defects known as 'microcracks' are introduced in the system. The failure process is initiated when minute bond cracks form at mortar–aggregate interfaces, while small cracks may also occur in the mortar and aggregate phases separately. Fracture of these microcracks give concrete the semblence of ductility; it is the brittle propagation of many microcracks that form a semi–ductile propagation of a macrocrack and ultimately lead to material failure. This fracture process is illustrated in Figure 2-3.

In practice, concrete as an engineering material is generally designed for use in

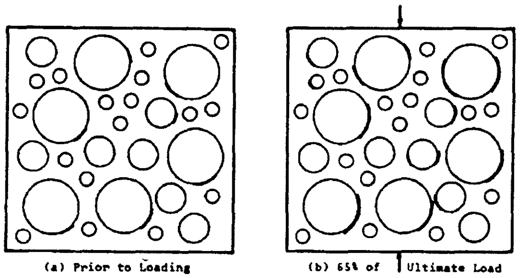

(a) Prior to Loading (b) 65% of Ultimate Load

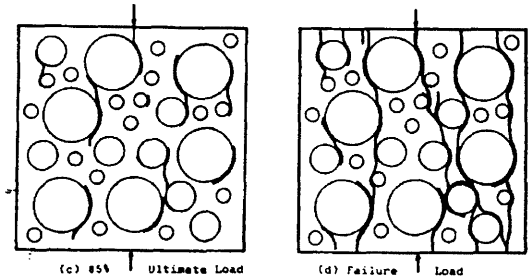

(c) 85% Ultimate Load (d) Failure Load

Figure 2-3: Progressive cracking under uniaxial loading (Liu, 1972)

compression and the tensile strength is usually neglected; however, predominent failure in concrete is through tension alone or in combination with shear. For example, the compressive test for concrete strength is actually testing the formation of longitudinal tensile cracks through the compression specimen. The low tensile strength of concrete is frequently described as the controlling factor of much of the behavior of the material. Microcracks in existence before any loading are largely responsible for these low tensile strengths, and ultimately the behavior of the material. For this reason an advanced understanding of the initiation and propagation of microcracks is essential in the study of the failure behavior of concrete as a composite material.

2.4 Importance of Mortar–Aggregate Interfaces in Concrete

A common initiator of microcracks in concrete are interfacial bond cracks between the mortar matrix and aggregate particles. The interfacial region is often the weakest zone in normal strength concretes and in some specially designed high strength concretes. This interfacial zone plays a large role in the determination of the mechanical properties of the concrete as a whole. Good mechanical performance of concrete as a composite can only be realized through effective stress transfer between its constituents; interfaces can control the degree of contact and cohesive forces between them. Three mechanisms for the transfer of forces between constituent materials have been suggested [59]:

- **Physical Interaction** This includes all mechanical friction between the aggregate and the cement paste,
- **Physical–Chemical Interaction** Strong chemical bonds can occur between the cement paste and the aggregate, allowing increased transfer of forces,
- **Mechanical Interlocking** For porous aggregates or aggregates with rough surfaces, mechanical "hooking" may occur to help transmit forces.

Strong interfaces are important for a cohesive composite material; however, interfaces may become too strong and alter the fracture scenario of failure in the composite, causing increased brittleness in material such as higher strength concretes.

2.4.1 Interfacial Cracking

It is generally agreed that the strength and deformation properties of concrete are closely related to the characteristics of the interface between the aggregates and the mortar. In normal strength concrete, the interface is usually considered the weakest link in the composite. Over the past twenty years, considerable research has been conducted to study the microcrack development, the nonlinear deformation behavior, and the failure mechanisms of normal strength concrete. It has been generally established that the development of bond cracks at the interfaces between mortar and aggregates plays a significant role in the inelastic deformation behavior [9, 10, 39, 52].

Although a strong bond at the interface between the matrix and the aggregate may enhance the overall strength and stiffness of the concrete, the increase in the interfacial bond may cause a brittle deformation and failure behavior. In general, crack propagation can be characterized by mechanical properties of each phase. They include:

- E = Young's modulus;
- K_{I_c} = Critical stress intensity factor;
- $\sigma - w$ = Stress–crack opening displacement constitutive relationship;
- v = Volume fraction of each phase of the material;
- Γ_i = Interfacial fracture toughness.

Using these parameters, simulations of material behavior have been performed using variations on a two–parameter fracture model [30, 35]. In the composite fracture model proposed by Jenq, all phases of the composite model are assumed to follow linear elastic fracture mechanics; Kitsutaka took a similar approach and incorporated a bilinear constitutive model. In both models, however, interfacial fracture and the incorporation of interfacial mechanical properties into the model were ignored. The incorporation of these important factors and fracture processes including interfacial crack propagation are essential in an accurate model and description of failure processes in concrete.

2.4.2 Assessment of Interface Fracture Parameters

Characterization of the interfacial fracture parameters such as the fracture toughness as a property of the mortar–aggregate interface is essential for the incorporation of mortar–aggregate interfaces into an accurate model of concrete behavior. An early experimental study [23] reported limited test results of mortar–aggregate fracture parameters under mode I loading conditions. Since cracking of mortar–aggregate interfaces involves mixed–mode fracture due to differences in properties of the constituent materials, a novel approach was needed. A sandwich specimen to test mixed–mode fracture parameters was reported by Buyukozturk et al. [9].

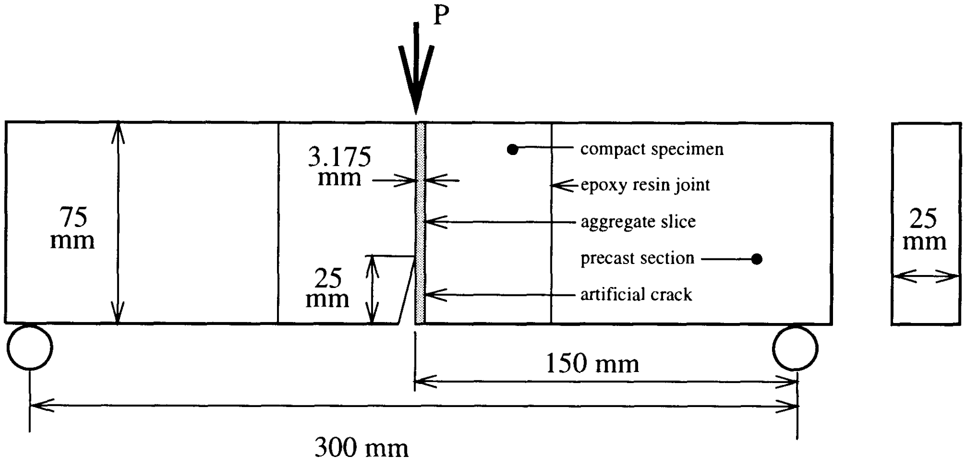

Figure 2-4: Sandwich specimen for interfacial fracture parameter testing

An interface crack model including a thin layer of aggregate sandwiched in a homogeneous body of mortar is shown in Figure 2-4. An initial crack lies along one of the interfaces coincident with the x_1 axis with the tip at the origin. If the thickness of the sandwich layer h is small compared to the crack length and to all other relevant in–plane length quantities, a universal asymptotic relation between the interface intensity factors, K_I and K_{II}, for the homogeneous problem, is given by Equation 2.1

$$Kh^{i\epsilon} = \sqrt{\frac{1-\alpha}{1-\beta^2}}K^{\infty}e^{i\omega(\alpha,\beta)} \tag{2.1}$$

The universal relation given in Equation 2.1 may be applied to any sandwich specimen. Proper techniques are required to sandwich an aggregate layer into the specimen and ensure that the crack stays along one of the interfaces. Residual stresses in the layer do not contribute to K in the sandwich specimen and, in calibrating such a specimen, only the external loading is accounted for. Using this procedure the fracture characteristics of a variety of interfaces have been investigated and will be described in the next chapter.

2.5 Conclusion

It is now well established that concrete, a brittle material, fails in combinations of tension and shear regardless of the loading conditions. Thus, tensile and shear cracking control the initiation, propagation, and culmination of loading failure in concrete. It has been shown that significant damage processes occur between the transition from microcracking to macrocracking, with changes and differences in material behavior during the transition. It has also been shown that mortar–aggregate interfacial cracking contributes significantly to the microcracking behavior of concrete, and can strongly influence the cracking scenarios and global behavior of the material. Thus, the importance of the study of interfaces in concrete has been demonstrated and the need for the characterization and assessment of mechanical properties of these interfaces has been established.

Chapter 3

Fracture Mechanics of Mortar–Aggregate Interfaces

3.1 Introduction

The term *fracture mechanics* defines the study of the response and failure of structure as a result of crack initiation and propagation. It is particularly useful to quantify the intense and often singular crack tip stress fields and to define and apply fracture based failure criteria. When considering a crack between two different materials, fracture mechanics ideology can be used to characterize the interfacial resistance to crack propagation as a material property, called the *fracture toughness*. This chapter reviews the fundamental concepts of interfacial fracture mechanics as applied to mortar–aggregate interfaces. It is based on the recent works of Hutchinson and co–workers [53, 46, 18, 29]. This chapter is also a combined review of similar chapters in K. M. Lee's PhD thesis [36] and U. Trende's MS thesis [55]. It also describes previous work in the continuing project that this thesis contributes to.

3.2 Bimaterial Elasticity

A composite is defined by a continuous system containing two or more homogeneous materials; in a localized view, portions of this system can be termed bimaterial. In

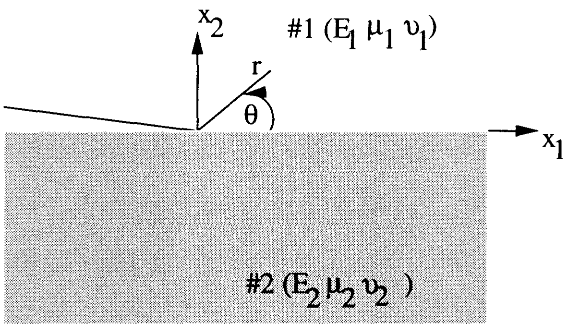

Figure 3-1: Geometry and conventions for an interface crack

this chapter, only plane strain deformations in isotropic bimaterials will be discussed. Figure 3-1 shows reference labels given to an interface crack configuration between two dissimilar materials *material 1* and *material 2*, with an interface on the x_1 axis. Let E_1, μ_1, and v_1 define the Young's modulus, shear modulus, and Poisson's ratio of material 1 as the substrate. Similar quantities E_2, μ_2, and v_2 can be defined for material 2.

For many elastic plane problems in bimaterials the elastic moduli mismatch can be characterized by two non–dimensional combinations of the elastic parameters [17]. Using the convention established in Figure 3-1, the moduli mismatch parameters, α and β, are

$$\alpha = \frac{\overline{E}_1 - \overline{E}_2}{\overline{E}_1 + \overline{E}_2} \tag{3.1}$$

$$\beta = \frac{1}{2}\frac{\mu_1(1-2\nu_2) - \mu_2(1-2\nu_1)}{\mu_1(1-\nu_2) + \mu_2(1-\nu_1)} \tag{3.2}$$

where $\overline{E} = E/(1-\nu^2) = 2\mu/(1-\nu)$, μ_i and ν_i are the shear modulus and Poisson's ratio of material i. The parameter α measures the relative stiffness between the two materials and asymptotically approaches 1.0 for high relative stiffness of material 1 compared to material 2 and -1.0 for low relative stiffness. In plane strain β vanishes when both materials are incompressible ($\nu_1 = \nu_2 = 1/2$).

3.3 Crack Tip Fields

Consider a semi–infinite, traction–free crack along the interface between two homogeneous isotropic half–planes with material 1 above and material 2 below, as in Figure 3-1. This is a homogeneous boundary problem, the solutions of which were presented first by England [1965], Erdogan [1965], and Rice and Sih [1965]. Their solutions here are presented using the notations of Rice because they reduce to conventional notation when the mismatch vanishes. For plane problems normal and shear stresses of the singular field acting on the interface at a distance r ahead of the tip are given in Equation 3.3.

$$\sigma_{22} + i\sigma_{12} = \frac{K}{\sqrt{2\pi r}} r^{i\epsilon} \tag{3.3}$$

where $K = K_1 + iK_2$, the complex interface stress intensity factor, $i = \sqrt{-1}$, and ϵ is the oscillation index, given as a function of β in Equation 3.4.

$$\epsilon = \frac{1}{2\pi} \ln(\frac{1-\beta}{1+\beta}) \tag{3.4}$$

It is noted also that K_1 and K_2 do not strictly measure the normal and shear singularities on the interface ahead of the crack tip due to the term $r^{i\epsilon}$ in Equation 3.3.

The associated crack face displacements at a distance r behind the crack tip, $\delta_i = u_i(r, \theta = \pi) - u_i(r, \theta = -\pi)$, are given in Equation 3.5.

$$\delta_2 + i\delta_1 = \frac{8K}{E^*(1 + 2i\epsilon)\cosh(\pi\epsilon)} \left(\sqrt{\frac{r}{2\pi}}\right) r^{i\epsilon} \tag{3.5}$$

The energy release rate per unit area crack extension is given in Equation 3.6 [42].

$$G = \frac{1}{E^* \cosh^2(\pi\epsilon)} |K|^2 \tag{3.6}$$

where E^* is defined as an average stiffness and given by Equation 3.7.

$$\frac{1}{E^*} = \frac{1}{2}\left(\frac{1}{\overline{E}_1} + \frac{1}{\overline{E}_2}\right) \tag{3.7}$$

Finally, the phase angle $\hat{\psi}$, a measure of the contribution of shear vs. opening mode, is defined in Equation 3.8.

$$\hat{\psi} = \tan^{-1}\left(\frac{Im(K\hat{L}^{i\epsilon})}{Re(K\hat{L}^{i\epsilon})}\right) \tag{3.8}$$

where $\hat{L}$ is a reference length.

3.4 Interfacial Fracture Toughness

Differences in elastic moduli at an interface disrupt the symmetry, even when geometry and loading are symmetric with respect to the crack plane, causing mixed fracture mode. Furthermore, an interface is frequently more brittle than the constituent materials. Also, because of low relative fracture energies, an interface crack may propagate into regions of the interface with much higher loading angles. As a result, a fracture toughness curve depicting fracture toughness vs. phase angle is necessary to fully characterize the interfacial toughness.

Let $\hat{L}$ denote a length characterizing the size of the fracture process zone or the typical size of the plastic zone at fracture, and let $\hat{\psi}$ be associated through Equation 3.8. Given the choice $\hat{L}$, the criterion for interface cracking can again be stated as

$$G = \Gamma_i(\hat{\psi}, \hat{L}) \tag{3.9}$$

This relationship has been investigated extensively using sandwich beam specimens and disk specimens [36]. These testing specimens are demonstrated in Figure 3-2. The dimensions of the sandwiched beam specimens were 152.0 mm × 50.8 mm × 38.1 mm, and the radius and thickness of the sandwiched Brazilian disk specimens were 38.1 mm and 25.4 mm, respectively. The thickness of the aggregate layer, h, was 2.54 mm for both specimens. The relative crack size (a/R) in the disk specimen was fixed to be 0.25 and the relative crack size (a/d) in the beam specimen was 0.375.

By using the measure values of the critical load, P, the fracture energies of the

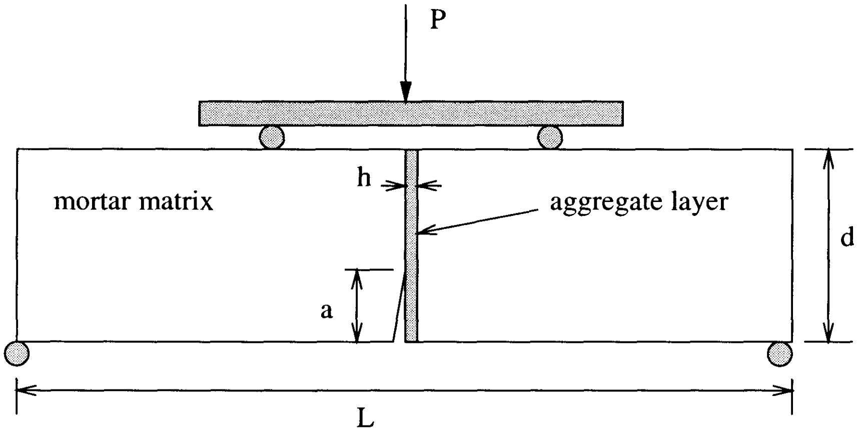

(a) Sandwiched four–point bending specimen

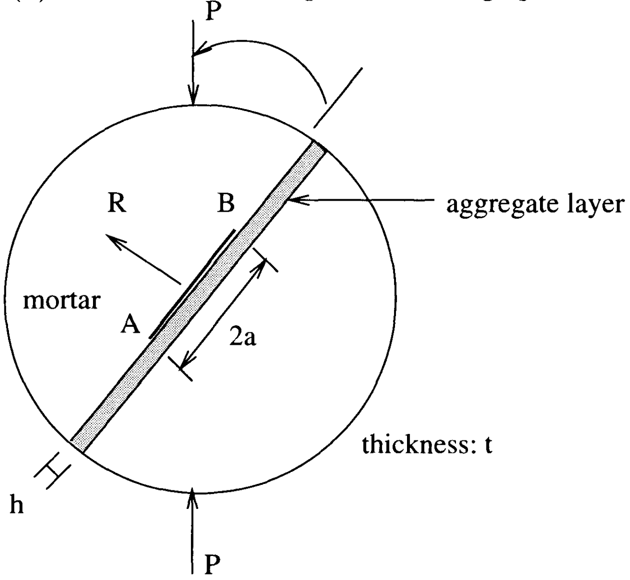

(b) Sandwiched Brazilian disk specimen

Figure 3-2: Testing specimens used by Lee (1993) mortar–aggregate interfaces were calculated for the sandwiched Brazilian disk specimens, the loading phase angles were calculated and the fixed length $\hat{L}$ was selected to be 2.54 mm, the thickness of the aggregate layer. Sample interfacial toughness curves are plotted in Figure 3-3. It is observed that the fracture energy markedly increases as the loading phase increases. It was also concluded that fracture energy curves for interfaces also depend on interfacial properties such as mortar strength, aggregate composition, and aggregate surface roughness, as well as the specimen testing size, which will be discussed in the next section.

3.5 Size Effects

Size scale effect[1] is defined as the change in normalized failure stresses among geometrically similar structures depending on their relative sizes. Most materials exhibit some size effect, but it is most remarkable in composite materials and structures; therefore, it is of significant importance in the study of mortar–aggregate interfaces. Linear elastic fracture mechanics (LEFM) is useful in describing and analyzing failures in terms of size effects. Figure 3-4 shows a plot of a relative measure of the size of a structure against a normalized failure stress. Typical engineering strength criterion usually incorporate no size effect, as shown by the horizontal line. LEFM analysis maintains a constant size effect, represented by the line with the slope of $-\frac{1}{2}$. The curve approaches the horizontal line for very small structures and the inclined line of linear fracture mechanics for very large structures.

A nominal failure stress, used to describe the size effect, can be given by

$$\begin{aligned} \sigma_N &= c_n \tfrac{P_u}{bd} \quad \text{for two–dimensional similarity} \\ \sigma_N &= c_n \tfrac{P_u}{d^2} \quad \text{for three–dimensional similarity} \end{aligned} \tag{3.10}$$

where P_u is maximum load, b is the specimen thickness, d is a characteristic length, and c_n is a material and structure dependent factor. The factor c_n can give various

---

[1] Hereafter referred to as 'size effect'.

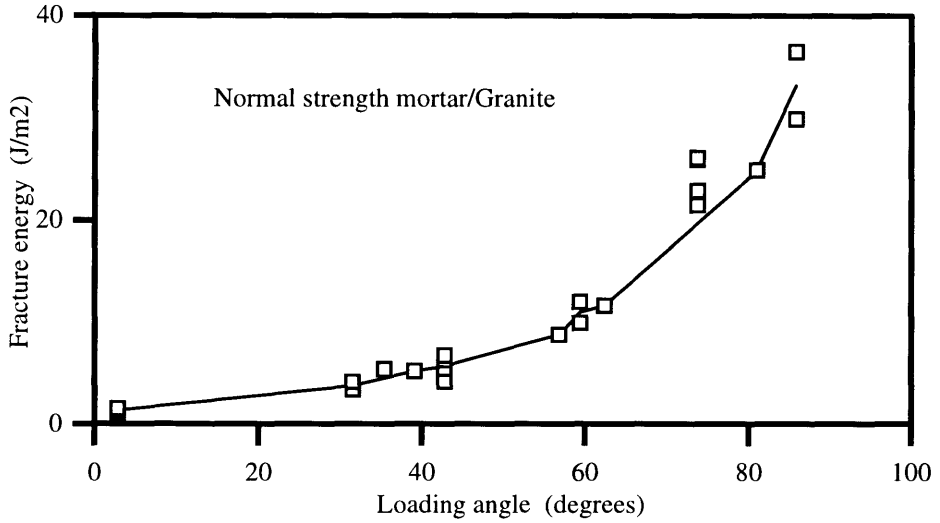

(a) Fracture energy curve for normal strength mortar/granite interface

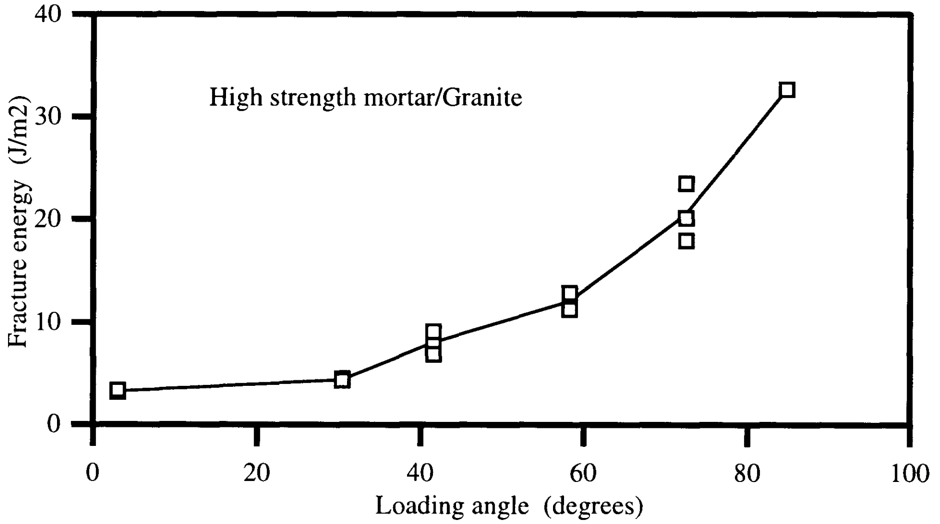

(b) Fracture energy curve for high strength mortar/granite interface

Figure 3-3: Fracture energy curves obtained by Lee (1993)

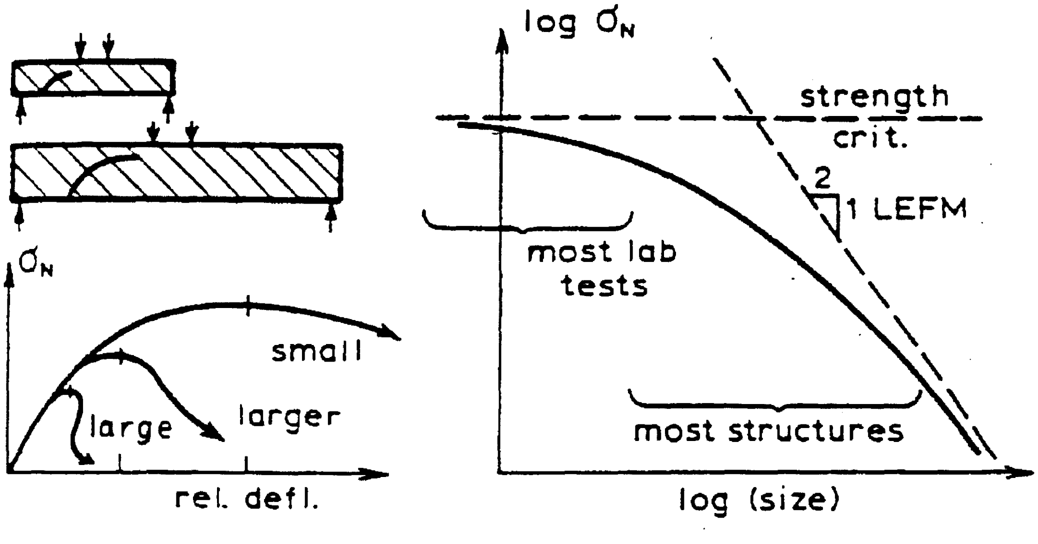

Figure 3-4: Size effect of concrete structures (Ashby and Jones, 1980)

stress descriptions such as the exact stress for a simply supported beam, plastic bending stress, and fracture stress dependent on crack length. It has been concluded that the energy dissipated at failure is a continuous function of the specimen size and the fracture process zone width, which may be considered constant [5]. Furthermore, it has been shown that by simple similitude arguments and dimensional analysis the nominal stress can be described by

$$\sigma_N = Bf_t' \left\{\beta\left[1+\beta^{-1}+A_1\beta^{-2}+\ldots+A_n\beta^{-n}\right]\right\}^{-\frac{1}{2}} \quad \text{with } \beta = d/d_0 \tag{3.11}$$

where B, d_0, $A_1 \ldots A_n$ are empirical coefficients, f_t' is a measure of the material tensile strength, and $\beta = d/d_0$ is the relative structure size. Reducing Equation 3.11 to the linear term leads to the most well known size effect law

$$\sigma_N = Bf_t' \left(1+\frac{d}{d_0}\right)^{-\frac{1}{2}} \tag{3.12}$$

where B and d_0 are empirical coefficients depending on failure mode and specimen geometry [4, 3]. If these coefficients for a particular failure type and geometry are known the nominal stress at failure can be calculated for any relative specimen size

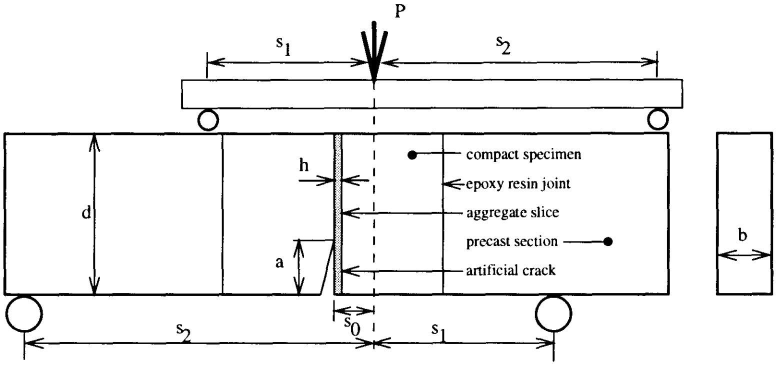

Figure 3-5: Setup for four-point bending test

within the applicable range of 1:20.

Equation 3.12 demonstrates that for structures with large (d/d_0) the size effect approaches that of linear elastic fracture mechanics of the form $\frac{1}{\sqrt{d}}$. Similarly, for very small structures the size effect approaches that of plastic limit analysis. Therefore, the size effect law of Equation 3.12 provides a transition from the plastic limit analysis to the fracture mechanics analysis, shown as the solid line in Figure 3-4.

Size scale effects in mortar–aggregate interfaces have been studied in detail by Trende (1995). Sandwiched beam specimens, shown in Figure 3-5, with variations in aggregate surface roughness and mixed mode loadings were tested in three different sizes. The resulting size effect data for the tests are summarized in Figure 3-6 with the test data and the size effect law plotted together with the strength criteria for comparison. It was concluded that interface fracture of high–strength mortar/granite composties demonstrates a strong size effect and that this effect complies with an established size effect law. Furthermore, increased aggregate roughness was found to increase the interfacial fracture energy.

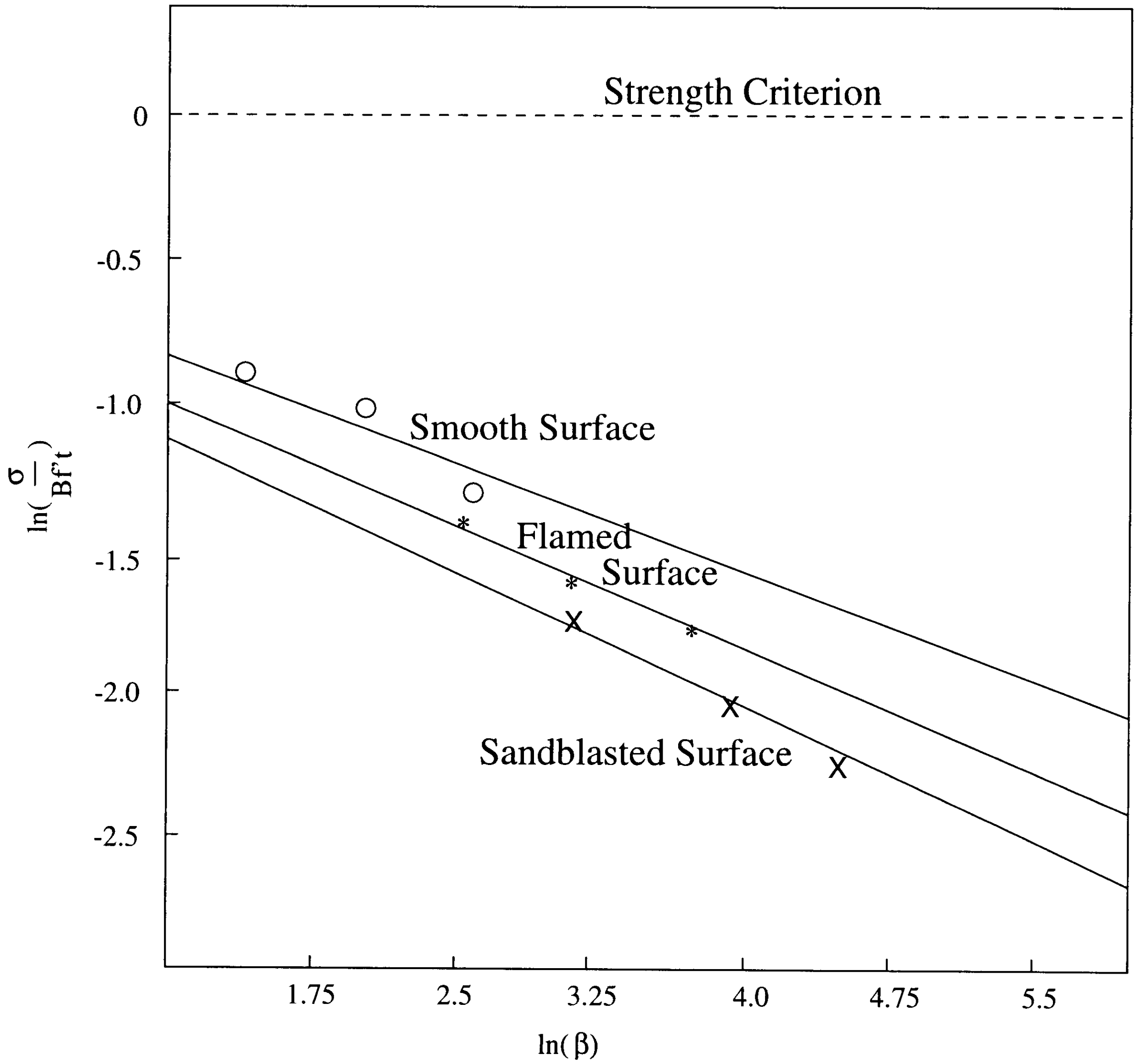

Figure 3-6: Size effect linear regression plot of mortar–aggregate interfaces

3.6 Crack Behavior Approaching the Interfacial Region

The behavior of a crack approaching an interfacial region has also been studied [36]. In concrete a crack impinging a mortar–aggregate interface may advance by either penetrating into the aggregate or deflecting along the interface. Let Γ_i be the fracture energy of the interface as a function of the phase angle $\hat{\psi}$ and let Γ_1 be the mode I fracture energy of the constituent material under consideration. The impinging crack is likely to be deflected if

$$\frac{\Gamma_i}{\Gamma_1} < \frac{G_d}{G_p^{max}} \tag{3.13}$$

where Γ_1 and Γ_i are material properties, which can be measured by fracture testing, and G_d is the energy release rate of the deflected crack and G_p^{max} is the maximum energy release rate of the penetrated crack.

For complex geometries the ratio G_d/G_p^{max} can be calculated using numerical analysis schemes. However, the ratio for a semi–infinite crack problem as functions of the angle of the approaching crack and elastic moduli mismatch parameters has been computed [22]. For example, when $\alpha = 0$ and the crack approaching angle γ is perpendicular to the interface, i. e. $\gamma = 90°$, G_d/G_p is approximately 0.25, indicating that the crack will deflect into the interface if the interface toughness is less than one quarter of the toughness of the material ahead of the crack.

These theories were tested through an experimental procedure by Lee (1993). Composite beam models shown in Figure 3-7 were tested to study crack propagation in interfacial regions and to verify the crack path criteria introduced above. Three mortar strengths (low, medium, and high) for matrices and two types of aggregates (granite and limestone) for the slab inclusions were used.

A finite element simulation was presented to investigate a crack path criterion in two–phase composite beams consisting of an aggregate inclusion embedded in a mortar matrix. The numerical predictions were compared with an experimental series results and correlation was obtained. This study represented an initial step for the use

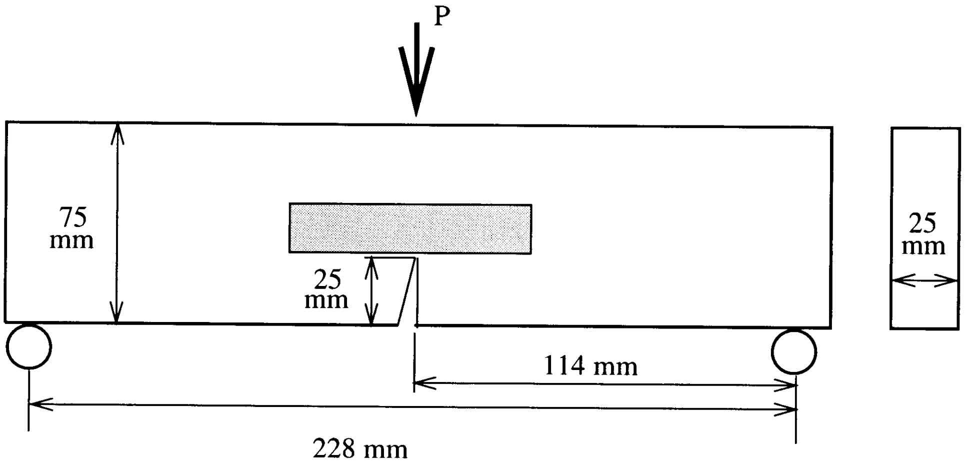

(a) Three–point bending slab inclusion specimen

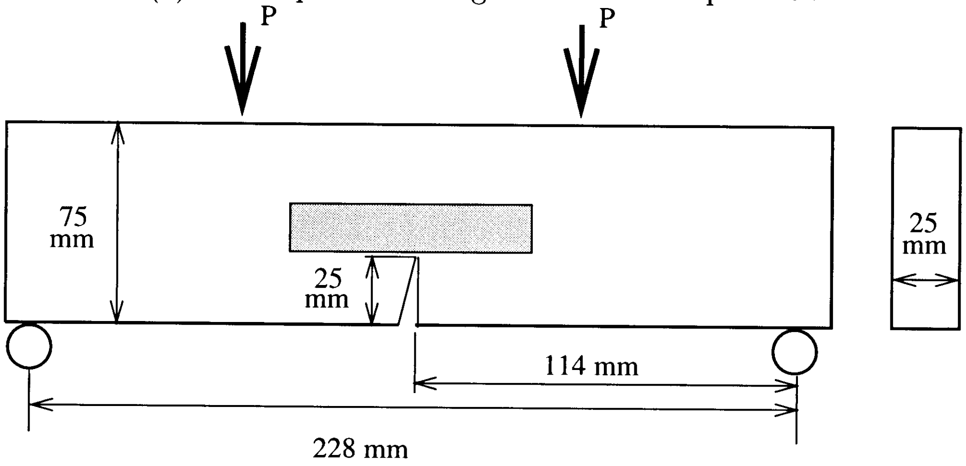

(b) Four–point bending slab inclusion specimen

Figure 3-7: Loading and specimen configurations of such methods in providing a fundamental understanding of the fracture criterion governing crack paths in mortar–aggregate interfacial zones.

3.7 Influence of Interfacial Parameters on Specimen Behavior

The influence of interfacial fracture parameters on the performance of a compressive block concrete specimen has been studied [45]. The goal of the investigation was to qualitatively assess the influence that these parameters have on the behavior of composite block specimens. For this reason, specimens composed of an aggregate inclusion embedded in a mortar matrix were tested under uniaxial compression. Specifically, material combinations that resulted in both interfacial crack propagation and aggregate crack penetration were utilized to provide parametric comparison of the composite performance.

Composite beams shown in Figure 3-8 were tested to study the influence of interfacial fracture parameters relative to the aggregate fracture parameters in composite performance. Three mortar strengths (low, medium, and high) for matrices and two types of aggregate (granite and limestone) were used for the circular inclusions.

Specimens that failed through interfacial propagation resulted in higher failure loads and higher strength mortars were shown to have stronger interfaces than normal strength interfaces. A finite element analytical procedure was conducted on the model specimens to examine the applicability of theoretical work to mortar–aggregate interfaces. The variation of fracture energy ratios as a function of elastic moduli mismatch parameters found from the numerical analysis was shown to agree closely with the theoretical work. This study represented an initial investigation into the assessment of the influence of mortar aggregate interfaces on the behavior of cementitious composites.

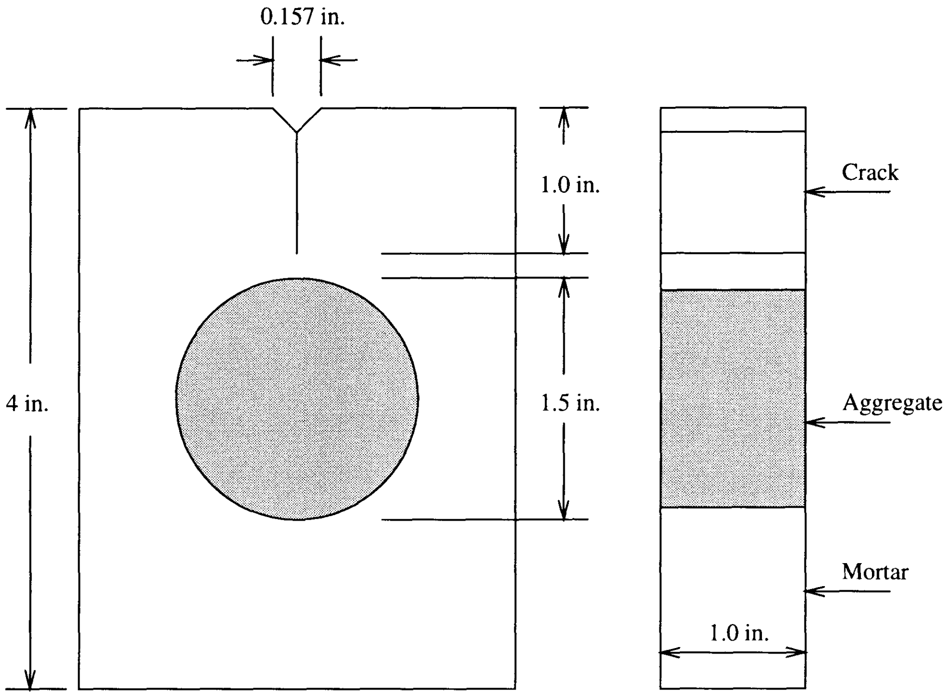

Figure 3-8: Dimensions of block specimen

3.8 Influence of Aggregate Parameters on Specimen Behavior

The influence of aggregate fracture parameters on the performance of three–point bending specimens has also been studied [35]. Experimental and numerical investigations of two–phase concrete composite models were conducted to study the fracture behavior of high strength concrete models subjected to mode I type loading. For this reason, three–point bending tests on pre–notched mortar beams with circular aggregate inclusions were performed. Models with normal strength mortar failed with interfacial cracking and the load displacement curves of the beams were not significantly affected by the aggregate types. In contrast, high strength matrix composite models failed by aggregate cracking and the shape of the load displacement curves were strongly affected by the aggregate strength.

An analytical cohesive model of transgranular cracking was proposed to simulate fracture in specimens where the crack propagated through the aggregate. The model was used to predict the load–displacement curves based on a multi–phase cohesive force model. Results of the analysis were shown to be in agreement with experimental results of the beams that exhibited aggregate cracking. The model prediction was used to study in a qualitative manner the effect of relative fracture energy of aggregate G_f^a to mortar G_f^m as $F_a = \frac{G_f^a}{G_f^m}$ and relative tensile strength of aggregate σ_t^a to mortar σ_t^m as $T_a = \frac{\sigma_t^a}{\sigma_t^m}$ on the composite behavior. Figure 3-9 shows the results of the parametric study for the load versus LLD curves of the beam specimens. In this analysis, two parameters T_a and F_a were varied and transgranular cracking was assumed for all cases. In general, with fixed T_a, larger F_a resulted in higher peak loads and larger fracture energy. This indicated that the improvement of the fracture energy of the inclusion is an important factor to improve the ductility of the composite. By increasing T_a with fixed F_a, the same tendency was obtained but the post–peak response becomes steeper, indicating more brittle behavior.

3.9 Summary

This chapter has introduced the basic concepts used in the study of fracture in a bimaterial interface. Terms relevant to bimaterial elasticity were presented, and then used in the description of the crack tip field around an interfacial crack. The crack tip stress intensity factors were introduced which lead to the definition of the interfacial fracture energy release rate. The phase angle was also defined and results from previous research were reviewed to demonstrate the interfacial fracture energy curve with respect to the phase angle. Size scale effect theory was reviewed and the motivation was presented for study into size effects exhibited by mortar–aggregate interfaces. Previous work in the continuing project was reviewed, introducing the work performed by the author in the next chapters.

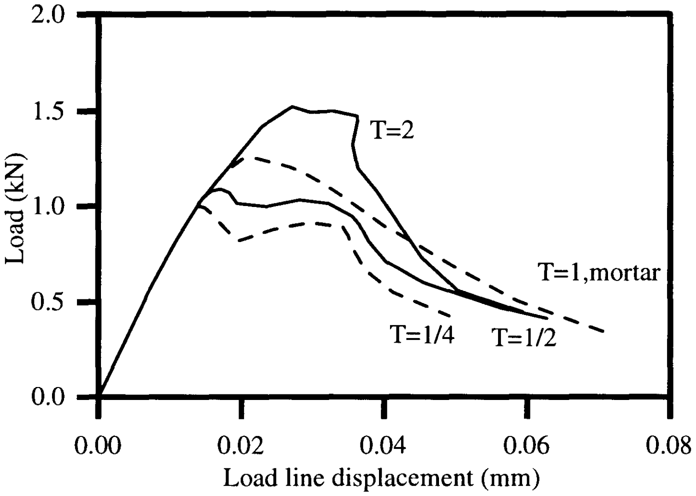

(a) Magnification of post-peak zone for parameter T_a study

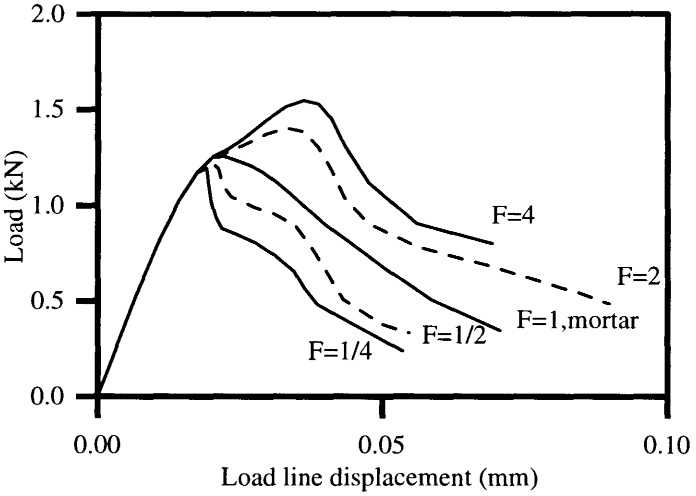

(b) Results of parametric study for parameter F_a

Figure 3-9: Results of parametric studies for transgranular cohesive model simulations

Chapter 4

Cohesive Fracture Propagation in Mortar–Aggregate Interfaces

4.1 Introduction

It is generally agreed that the damage process in failing concrete is initiated by microcracks far ahead of a propagating crack which, with additional load, ultimately link together to form continuous cracks [26, 48, 10, 39, 52]. The development of bond cracks at the mortar-aggregate interfaces is often attributed to the initiation of microcracks; it has been shown that interfacial zones are the "weak link" in crack formation [10, 11, 58]. Interest in the study of mortar-aggregate interfaces has increased with the need for the development of high–performance cementitious materials.

Several investigators and models have successfully described the complex failure mechanisms of concrete as a composite material. Perhaps one of the simplest yet most widely accepted model of crack propagation in concrete is the Hillerborg single discrete crack model [24]. Using this model, many fracture mechanics approaches have accurately described the highly nonlinear strain–softening behavior of concrete and its constitutive materials during fracture [19, 51]. It has been used to predict ductility of concrete as a homogeneous material [40] and as a composite where crack propagation occurs through its constitutive materials [35].

This chapter uses a modified Hillerborg analytical model to investigate crack propagation within the interface of mortar and aggregate in concrete. It provides additional work to support and confirm interfacial fracture data obatined from previous researchers and uses the results in a new analytical model of the interfacial fracture process. At issue are the fracture properties of the interface and how they are affected by concrete characteristics like mortar strength and aggregate surface roughness investigated in the previous chapter. The modified Hillerborg model is employed to investigate the cohesive behavior of interfacial cracking in mode I (tensile stresses) and mixed mode (shear and tensile stresses) crack growth. To verify the accuracy of the model, the failure behavior and the load/load–line displacement curves of the tested composite beams are simulated. Several strain–softening material relationships are examined in this simulation to model the strain–softening behavior of the interfacial region. Such a quantitative study of fracture in the interfacial region will yield an accurate deformation model of the "weak link" in concrete failure.

4.2 Experimental Program

Investigations into cohesive strain–softening behavior have used a multitude of testing geometries. Among others, recent work has included the compact–tension specimen [41, 23], the double cantilever beam specimen [19], and the three point bending specimen [40, 35, 56]. The three point bending specimen has shown several recent reliable analyses and has also been successfuly used in interfacial testing [27, 36, 56].

For the study described in this chapter, sandwiched beam specimens were tested to investigate interfacial fracture in concrete composites under three point bending mode I (tensile stresses) and mixed mode (shear and tensile stresses) loading. These geometries have been analyzed [57] and repeatedly proven successful testing specimens [27, 56]. Three different mortar strengths were used with a slice of granite sandwiched between the mortar sections. An initial crack was introduced at the interface between the granite slice and the mortar.

The testing parameters in this study were the mortar strength, the mode of crack propagation, and the aggregate surface roughness. All specimens were made using

Table 4.1: Mix proportions of mortars

Mix	W/(C+SF)	S/C	SF/C [%]	HRWR/C [%]
Low strength	0.50	2.0	0.0	0.0
Med strength	0.35	2.0	5.0	1.0
High strength	0.283	2.0	10.4	2.2
W-water, C-cement, S-sand, SF-silica fume, HRWR-high range water reducer				

Table 4.2: Material properties

Material	σ_c [MPa]	E [GPa]	ν
Low strength mortar	40.0	27.8	0.2
Med strength mortar	48.6	32.5	0.2
High strength mortar	83.8	33.3	0.2
Granite	123.0	42.2	0.16

Type III cement to produce high early strength mortars. To study both mode I and mixed mode propagation, tests were conducted in mode I and in a mixed mode loading chosen with a shear to tensile stress ratio given by Equation 3.8 of 0.27 at the crack tip. Smooth and sandblasted aggregate surface roughnesses were used to investigate how surface properties of the aggregate affect brittleness in the interfacial zone.

4.2.1 Materials

Three different strength mortars were combined with the granite slices to create the specimens. The mortars tested had strengths of 40.0 MPa, 58.6 MPa, and 83.7 MPa for low, medium, and high strength specimens. The medium and high strength mortars were made using a naphtalene sulfonate type superplasticizer and condensed silica fume in slurry form. The granite chosen was Chelmsford Granite, quarried by Fletcher Granite Co., Chelmsford, MA. The mix proportions of the mortars are given in Table 4.1 and the properties of the materials are reported in Table 4.2.

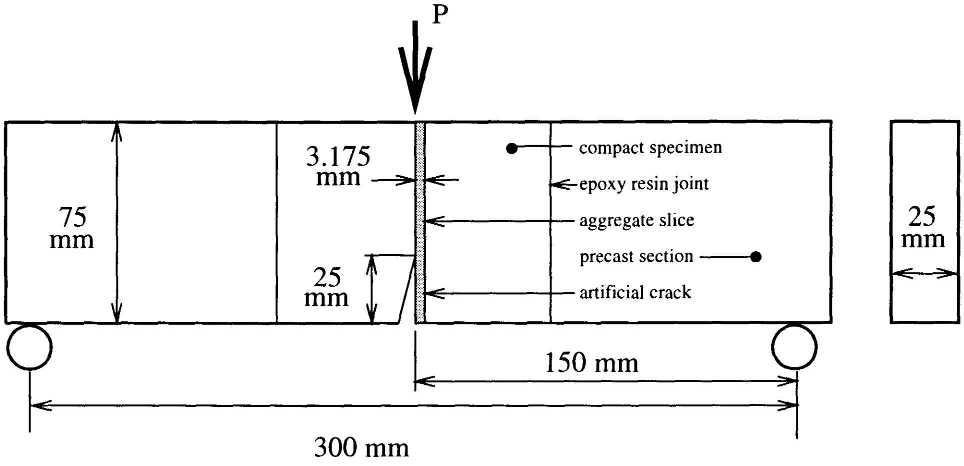

Figure 4-1: Three point bending mode I loading specimen

The two roughnesses of the granite were characterized optically. Smooth surfaces were acheived solely by the diamond saw cut; the surface was smooth to the touch with no visible scratches. The sandblasted surface achieved a pit depth of about 0.5 mm with an average grain diameter of about 3.0 mm.

4.2.2 Test Configuration and Loading

For mode I testing the three point bending configuration shown in Figure 4-1 was used. For mixed mode testing the three point bending loading shown in Figure 4-2 was used. In the mixed mode tests the ratio of shear to torsion stresses at the crack tip was 0.27. This ratio is known as the loading angle, with pure mode I (tension) as 0°; the ratio used for mixed mode loading in this study corresponds to 15°, as given by Equation 3.8.

For each series of specimens six testing beams were cast. The relative initial crack length was held constant at 1/3 the beam depth. This crack was created by epoxy resin hardened onto the aggregate surface before mortar was cast. The specimens were tested at the age of 7 days on a 1-kip INSTRON testing machine, shown in Figure 4-3. The load/load-line deflection curves from this Instron machine were obtained with 0.1 mm accuracy. Peak failure loads were used to calculate the fracture parameters

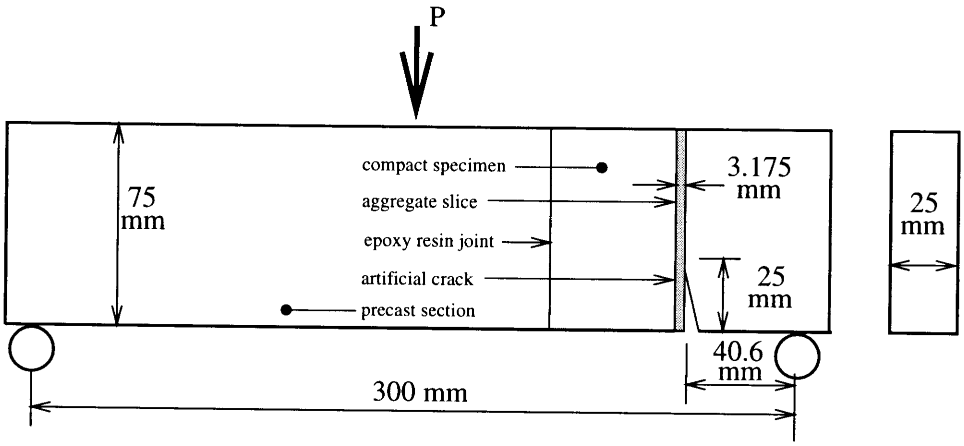

Figure 4-2: Three point bending mixed mode loading specimen

used in the analysis.

4.3 Results of Experimental Program

The average failure loads P_u^{avg} for the valid tests are reported in Table 4.3. A sample of a fractured central portion of a testing specimen is shown in Figure 4-4. Also reported are a sample failure load P_u^{smpl} used in the ductility analysis below. Fracture toughnesses for the interface are calculated from the stress intensity factors. For mode I loading, the three point bending is computed by [50]

$$K_I = \frac{3SP}{2tW^2}\sqrt{a}F_I(\alpha), \qquad \alpha = a/W$$

where $F_I(1/3) = 1.08228$, a/W is the relative crack length, t is the specimen width, W is the specimen height, and S is the distance between supports.

For a mixed mode loading, both mode I and mode II fracture toughnesses are computed. They are given by

$$K_I = \frac{f_b M}{tW^{3/2}}$$

and

$$K_{II} = \frac{f_s Q}{tW^{1/2}}$$

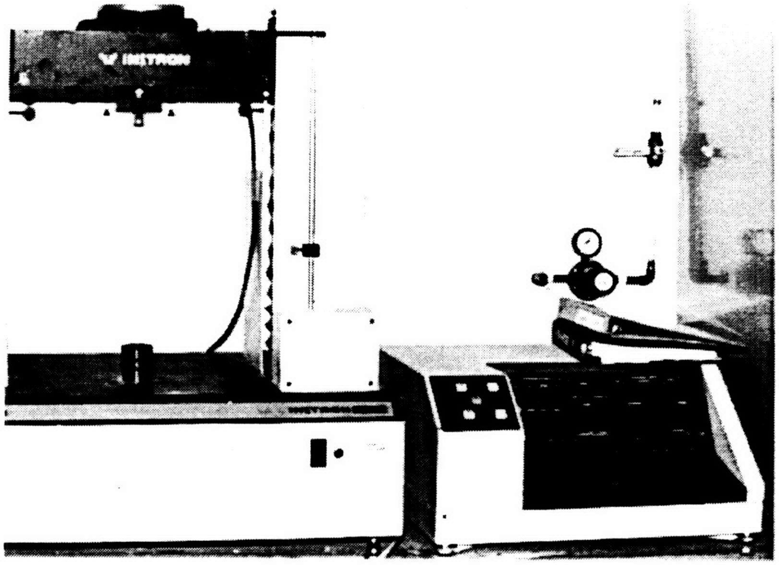

Figure 4-3: 1–kip INSTRON used in the testing series

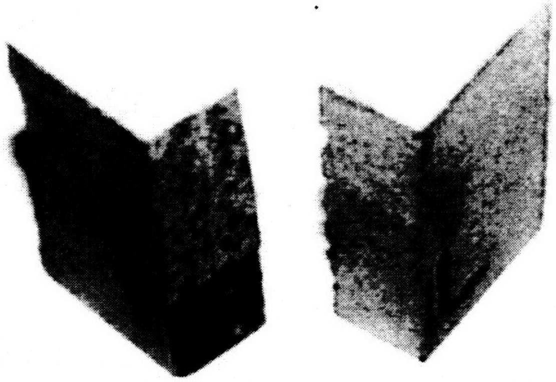

Figure 4-4: Sample tested specimens from the tested series

Table 4.3: Fracture loads and energy release rates

Mode I testing ($\phi = 0^\circ$)

Series	P_u^{avg} [kN]	P_u^{smpl} [kN]	G_f^{avg} [J/m^2]	G_f^{smpl} [J/m^2]	$f_t'^{smpl}$ [kPa]
Low strength	0.215	0.227	1.423	1.596	1.584
Med strength	0.154	0.178	0.739	0.976	1.242
High strength	0.310	0.226	2.949	1.568	1.575
High strength/ sandblasted	0.331	0.332	3.362	3.382	2.313

Mixed mode testing ($\phi = 15^\circ$)

Series	P_u^{avg} [kN]	P_u^{smpl} [kN]	G_f^{avg} [J/m^2]	$G_{I_f}^{smpl}$ [J/m^2]	$G_{II_f}^{smpl}$ [J/m^2]	$f_t'^{smpl}$ [kPa]	$f_s'^{smpl}$ [kPa]
Low strength	0.904	0.857	2.146	1.799	0.130	1.594	0.332
Med strength	0.616	0.642	0.997	1.010	0.073	1.194	0.249
High strength	1.207	1.097	3.824	2.946	0.212	2.040	0.425
High strength/ sandblasted	1.116	1.095	3.270	2.935	0.212	2.037	0.424

where the factors f_b and f_s were computed for a relative crack length of $a/d = 0.333$ as $f_b = 7.03$ and $f_s = 1.00567$ [57]. Here M is the bending moment and Q is the shear force at the crack tip.

Interface testing introduces a modification of the crack stress distribution. The mismatch of elastic properties of the two materials at the interface cause a slight shift in the loading angle. This mismatch is expressed in Dundur's parameters

$$\alpha = (\bar{E}_1 - \bar{E}_2)/(\bar{E}_1 + \bar{E}_2)$$

and

$$\beta = \frac{\mu_1(1-2\nu_2) - \mu_2(1-2\nu_1)}{2(\mu_1(1-2\nu_2) + \mu_2(1-2\nu_1))}$$

where $\bar{E}_1 = E_1/(1-\nu_1^2)$ and $\bar{E}_2 = E_2/(1-\nu_2^2)$, in which E_i is the modulus of elasticity, ν_i is Poisson's ratio, and μ_i is the shear modulus of material i [17]. The shift in the loading angle due to the elastic mismatch ω was reported by Suo and Hutchinson [53] as a function of α and β. For most mortar–aggregate interfaces, β and its influence on the loading angle shift ω is very small and can be nglected [9, 38]. For the mixed mode specimen, the crack tip stress intensities are

$$K_1 = \sqrt{1-\alpha}(K_I \cos\omega - K_{II} \sin\omega)$$

and

$$K_2 = \sqrt{1-\alpha}(K_{II} \cos\omega - K_I \sin\omega)$$

Finally the critical interface fracture energy release rate is computed by

$$G_i = G_I + G_{II} = (K_I^2 + K_{II}^2)/\bar{E}_1$$

The ultimate tensile strength f_t' and ultimate shear strength f_s' of the interface is also reported in Table 4.3. They are calculated by

$$f_t' = \frac{M_{cr}(\frac{W}{2})}{I_{cr}}$$

and

$$f_s' = \frac{V_{cr}}{A_{cr}}$$

where M_{cr} and V_{cr} are the critical moment and shear at failure and I_{cr} and A_{cr} are the moment of inertia and area of the section reduced by the initial crack.

The interface energy release rate G_i was computed for each specimen from the measured failure loads to compare the effects of different material combination, aggregate surface roughness, and loading angle. The resulting values agree strongly with previous work by Trende [55] and Lee [36]. The fracture energies and bond strengths increase with mortar strengths and also increase with rougher aggregate surfaces. Medium strength mortars did not follow this trend; however, their ductility parameters will be shown to comply with a similar pattern.

Load/load–line displacement curves for samples from each tested series are shown in Figure 4-5. The post–peak failure shape of these curves provide a qualitative comparison of the ductility of the various interfaces. For example, in Figure 4-5(a) mode I loading deflections show a decrease in post peak behavior with stronger mortars. These interfaces can be said to be more brittle. It is also observed that more ductile post–peak behavior is demonstrated by samples with sandblasted surfaces.

In Figure 4-5(b), mixed mode load–displacement curves show a similar increase in brittleness with stronger mortars. However, sandblasted surfaces demonstrate a significant additional post–peak behavior, perhaps attributable to the increased shear resistance of the rougher surface.

4.4 Cohesive Fracture Analytical Model

To investigate increased interfacial brittleness with stronger mortars a model is proposed to study the cohesive behavior of the interfaces. The interface is assumed to have a brittle cohesive behavior that fails at stresses and displacements significantly less than those of their constitutive materials. The tensile strength of the interface has been shown to be many orders of magnitude lower than the tensile strength of the mortar; the fracture energy of the interface is also orders of magnitude less than

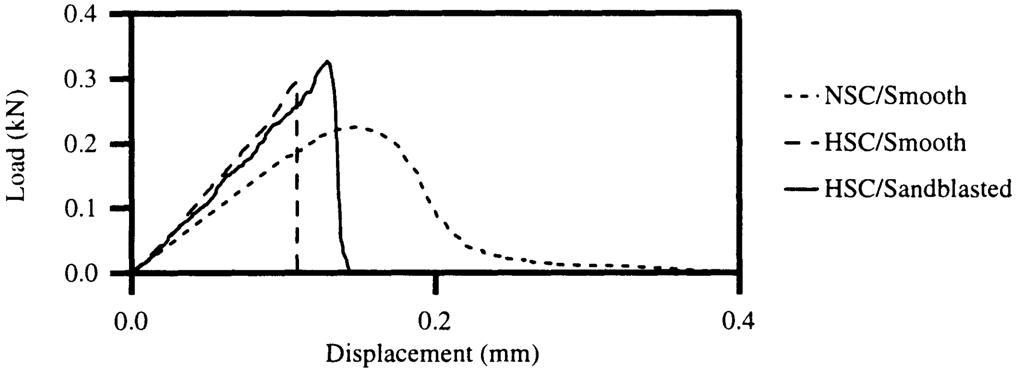

(a) Interface specimens in mode I loading

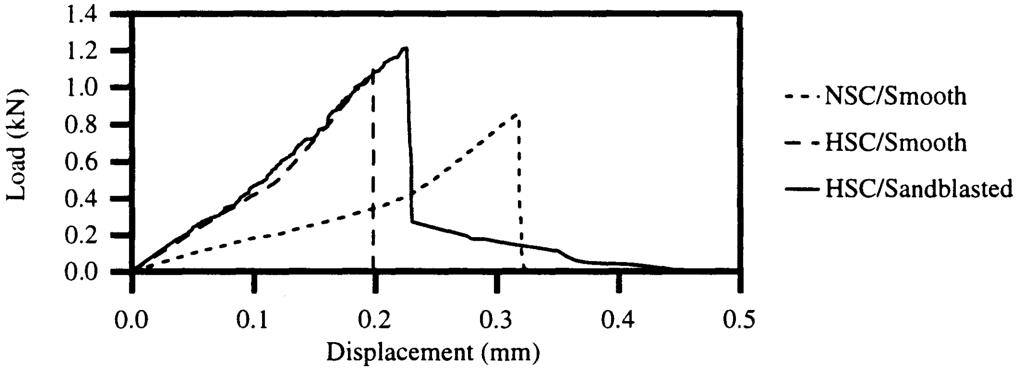

(b) Interface specimens in mixed mode loading

Figure 4-5: Sample load/load-line displacement curves of interfacial specimens

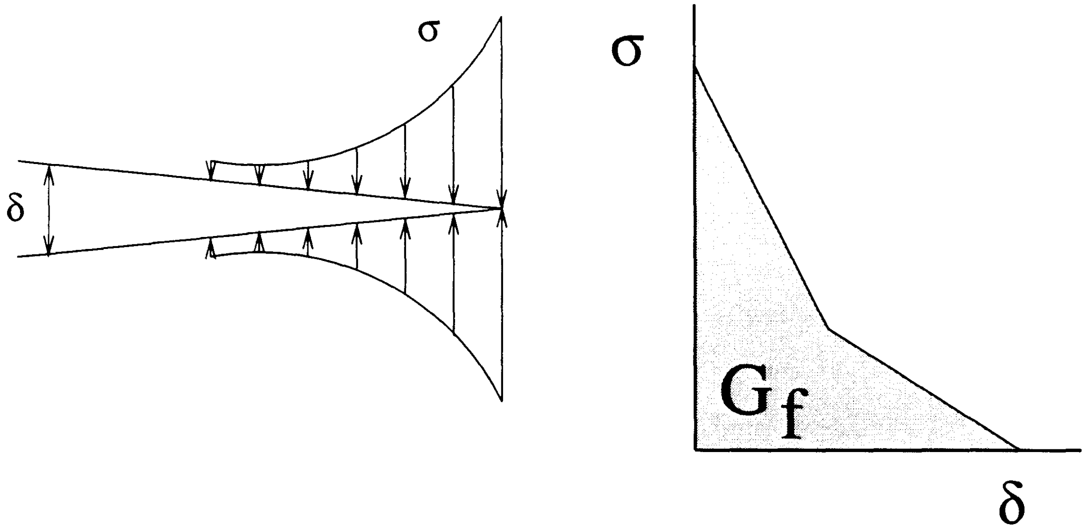

Figure 4-6: Hillerborg single discrete crack model and bilinear constitutive relationship

the mortar.

Cohesive models have been used to model mortars, aggregates, and even concrete as a homogeneous material [35, 19, 40]. The damage process is modeled with cohesive forces trailing the crack tip to simulate material plasticity, as illustrated in Figure 4-6. It is the post peak constitutive relationship that determines the success of the model. It has been concluded repeatedly that a bilinear strain–softening relationship best models these materials.

In this investigation both linear and bilinear strain–softening relationships were used to model the interfacial specimen load–deflection curves. Crack propagation in the interfacial three–point bending specimens was modeled by a fictitious crack with a Hillerborg type single discrete crack model. This model was modified to investigate interfacial crack propagation and was applied to both the mode I and mixed mode testing configurations.

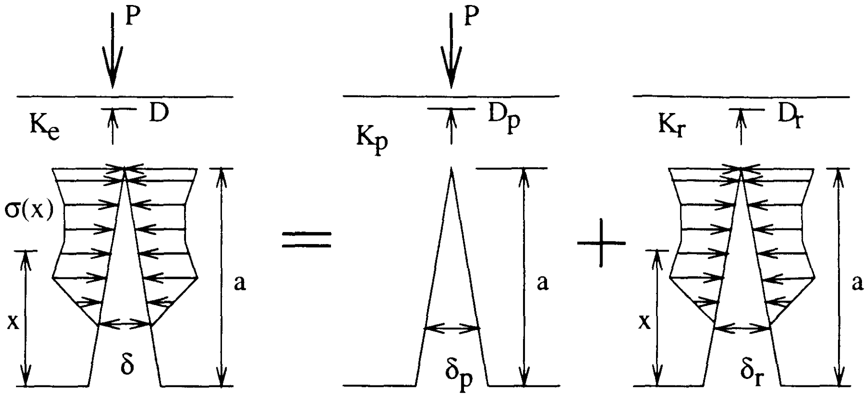

Figure 4-7: Mode I K–superposition

4.4.1 Mode I

The investigation of the mode I strain–softening behavior of interfacial crack propagation incorporated the modified Hillerborg model and both linear and bilinear constitutive relationships. Simulations of the load/load–line displacement diagram of a sandwiched specimen in pure mode I loading was made available through an iterative computer model.

The relation of external load and displacement is obtained by solving the equations of the net stress intensity factor (K_e), the equilibrium of crack opening displacement (COD) at crack surface, and the constitutive function of the COD and cohesive stress. For the calculation of the crack opening displacements a K–superposition method was employed [19]. Figure 4-7 shows that there are two contributions to K_e. One is the stress intensity factor due to the applied load (P), K_p; the other, K_r, is due to the cohesive forces $\sigma(x)$ acting across the crack faces in the process zone where the material is softening. Hence we have

$$K_e = K_p + K_r = 0$$

The assumption here is that K_e is sufficient to characterize the singularity at the crack tip.

The equilibrium of crack opening displacement at the crack surface is given by

$$\delta = \delta_p - \delta_r$$

where δ_p is the COD due to the three point bending load and δ_r is the COD due to the cohesive stress. These displacements are derived by Castigliano's theorem

$$\delta_y = \delta_0 + \frac{2}{E^*} \int_0^a K \frac{\partial K_F}{\partial F} da$$

Two equations are therefore available relating the three point bending load to the cohesive stresses. Solving the stress intensity equilibrium for the three point bending load and substituting it into the COD equilibrium, we obtain a relationship between the COD and the cohesive stresses

$$\delta(a, x) = \frac{1}{E^*} \int_0^a \sigma(a, c) H(a, x, c) dc$$

where

$$H(a, x, c) = \frac{K_r \delta_f}{K_p} - \delta_r$$

A constitutive relationship for the material is needed to solve the problem. It is given by an equation relating the COD to the cohesive stresses

$$\sigma = f(\delta)$$

By substituting this into the COD/cohesive stress equation the crack opening displacements, $\delta(a, x)$, can be solved for any given crack length and cohesive forces.

The solution is iterative, however, as the cohesive forces are initially assumed. When the COD is solved the resulting cohesive forces are compared to the assumed forces; when the COD and cohesive forces finally agree, the crack is in equilibrium for that advancement. At this point the external force P and load–line displacement D are solved.

4.4.2 Mixed Mode

Hillerborg observed that the model is also valid for mixed mode loading [24]. The cohesive force model was further developed to simulate the load/load–line deflection diagram of the sandwich specimen in mixed mode three–point bending loading. A similar iterative computer model was created using the same theory as mode I loading. Portions of this computer program script are given in Appendix A. In mixed mode loading the K–superposition will include both tensile and shear cohesive forces. Figure 4-8 shows that now there are four contributions to K_e. Here the external load (P) is divided among load for mode I COD and load for mode II COD. Now the mixed mode stress intensity factor may be expressed as

$$K_e = (K_{p_I} + K_{r_I}) + i(K_{p_{II}} + K_{r_{II}})$$

Following in a similar manner the COD is given by

$$\delta = (\delta_{P_I} + \delta_{r_I}) + i(\delta_{P_{II}} + \delta_{r_{II}})$$

Utilizing Castigliano's theorem similar equations can be derived relating the mixed mode three point bending load to the cohesive stresses. Again substituting the stress intensity equilibrium into the COD equilibrium the relationship between the COD and cohesive stresses is obtained

$$\delta = \delta_I + i\delta_{II} = \frac{1}{E^*}[\int_0^a \sigma(a,c)H_I(a,x,c)dc + i\int_0^a \tau(a,c)H_{II}(a,x,c)dc]$$

where

$$H_I(a,x,c) = \frac{K_{r_I}\delta_{P_I}}{K_{p_I}} - \delta_{r_I}$$

and

$$H_{II}(a,x,c) = \frac{K_{r_{II}}\delta_{P_{II}}}{K_{p_{II}}} - \delta_{r_{II}}$$

Two constitutive relationships for the material now are needed. The tensile relationship (similar to the relationship used in the mode I analysis) and the shear

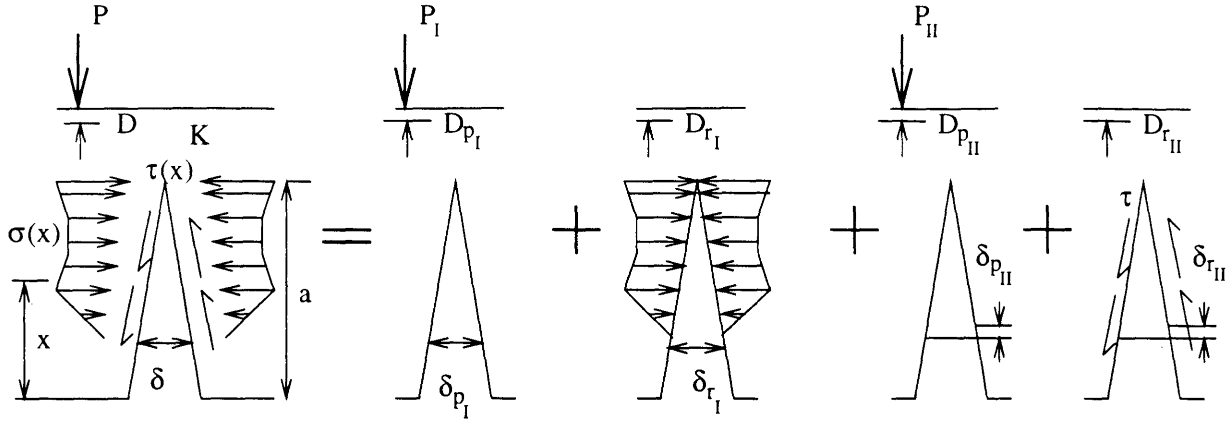

Figure 4-8: Mixed mode K–superposition

relationship are given by

$$\sigma = f(\delta_I)$$

and

$$\tau = f(\delta_{II})$$

Now the crack opening displacements can be solved for a given crack length and cohesive forces.

Again the solution here is iterative in the same manner as the mode I simulation. An agreement can be found between the crack opening displacements and the cohesive stresses. When they are in equilibrium the external three point bending load is found as the sum of the load creating mode I stresses and the load creating mode II stresses.

$$P = P_I + P_{II}$$

Similarly the three point bending displacement is found as the sum of the displacement due to mode I tractions and the displacement due to mode II tractions.

$$D = D_I + D_{II}$$

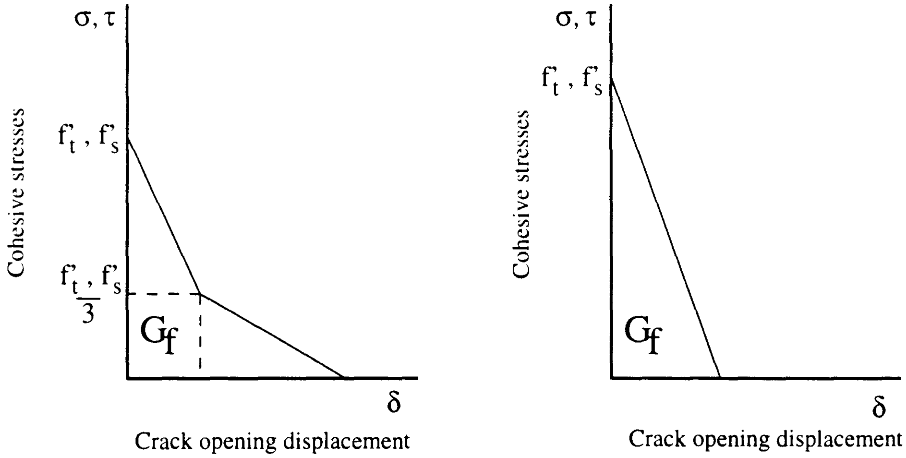

Figure 4-9: Bilinear and linear constitutive models

4.5 Method and Results of Experimentation

4.5.1 Methodology

The load/load–line deflection curves for the mode I interface tests were simulated first. Two strain softening relationships were investigated for mode I tensile behavior. They were the bilinear and linear models depicted in Figure 4-9. The bilinear model used was the same that found success in modeling concretes, mortars, and aggregates [35, 19, 40]. The area enclosed by the $\sigma - \delta$ relationship is given as the energy release rate (G_f) of the material and the initial tensile stress (f_t') is the modulus of rupture of the material.

From each set of tests a representative sample was chosen to model. The chosen sample was closest to the fracture load and ductility behavior of the group it came from. From this chosen sample the fracture energy (G_f^{smpl}) and the rupture stress $(f_t^{\prime smpl})$ was calculated by using the cross section of the beam reduced by the crack. These material constants were used as parameters in the modeling program. The results from the mode I simulation are shown in Figures 4-10 through 4-12. The linear strain–softening relationship was plotted with dashed lines while the bilinear relationship was plotted as a dotted line.

From the mode I simulations the linear constitutive relationship was found to

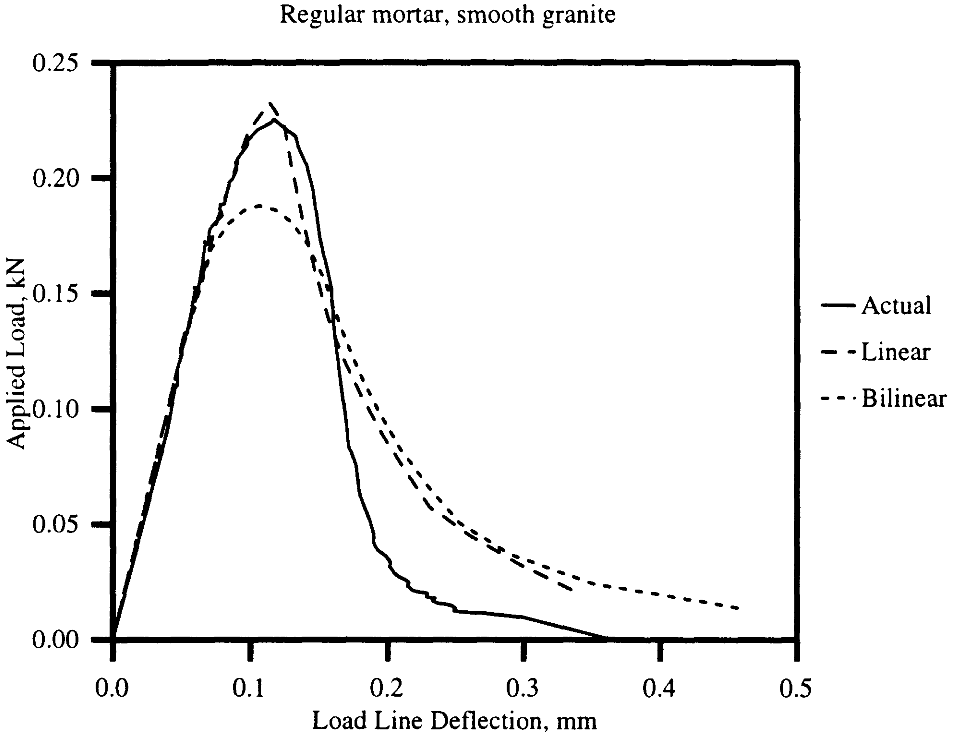

Figure 4-10: Low strength mortar/smooth interface in mode I loading

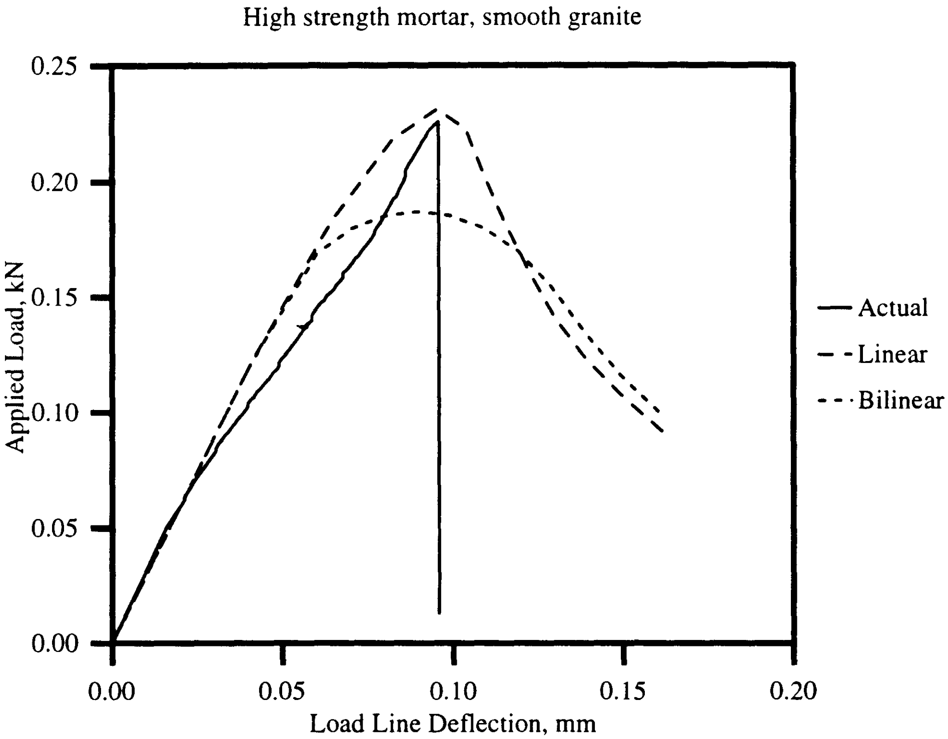

Figure 4-11: High strength mortar/smooth interface in mode I loading

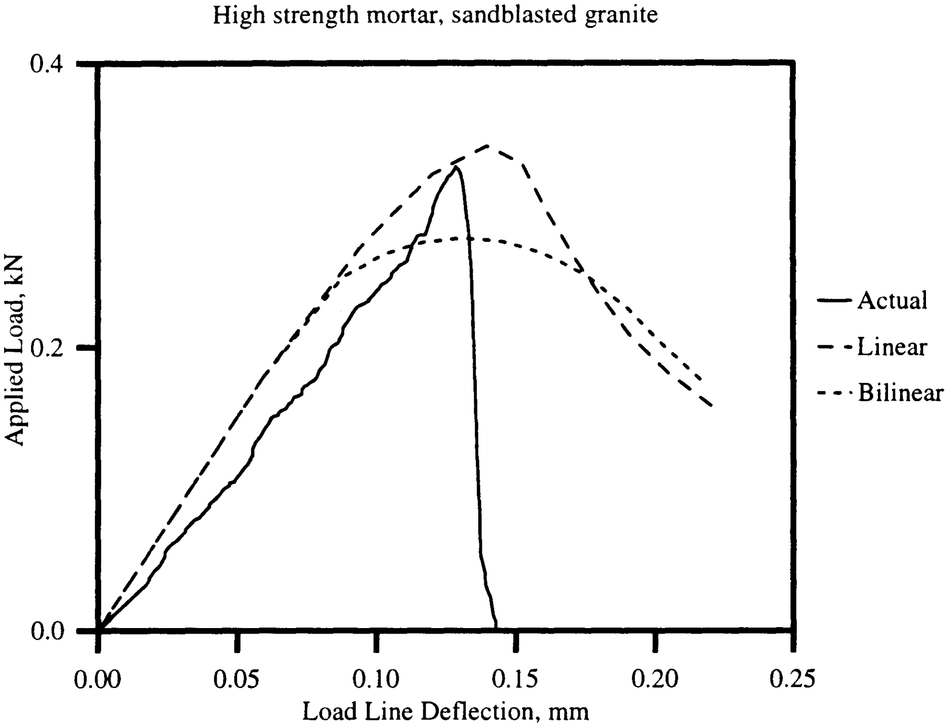

Figure 4-12: High strength mortar/sandblasted interface in mode I loading

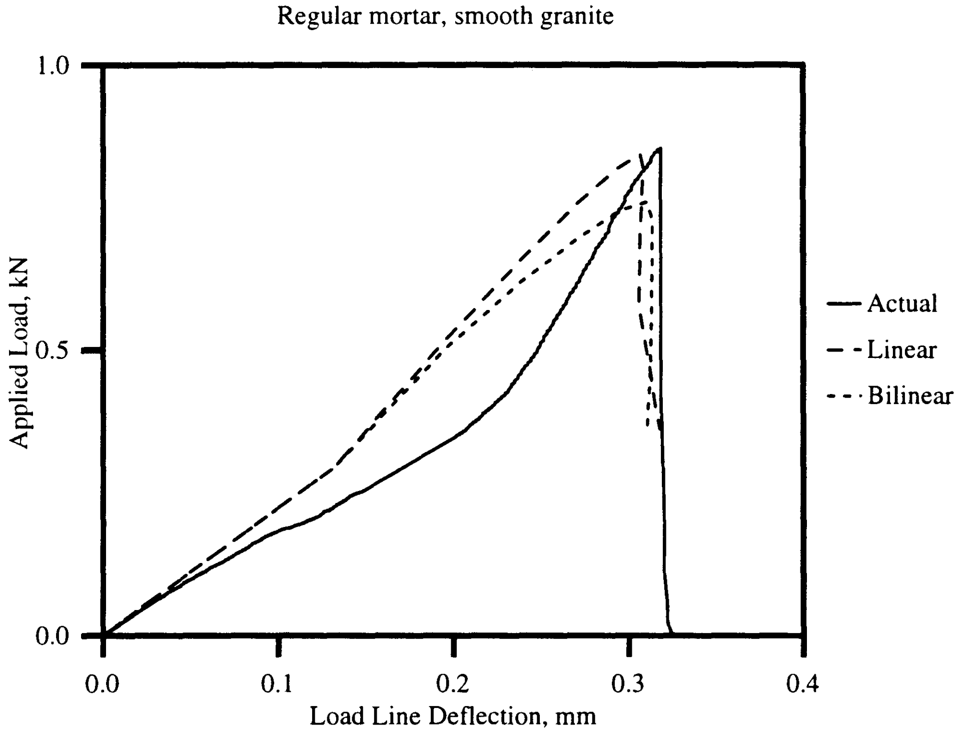

Figure 4-13: Normal strength mortar/smooth interface in mixed mode loading

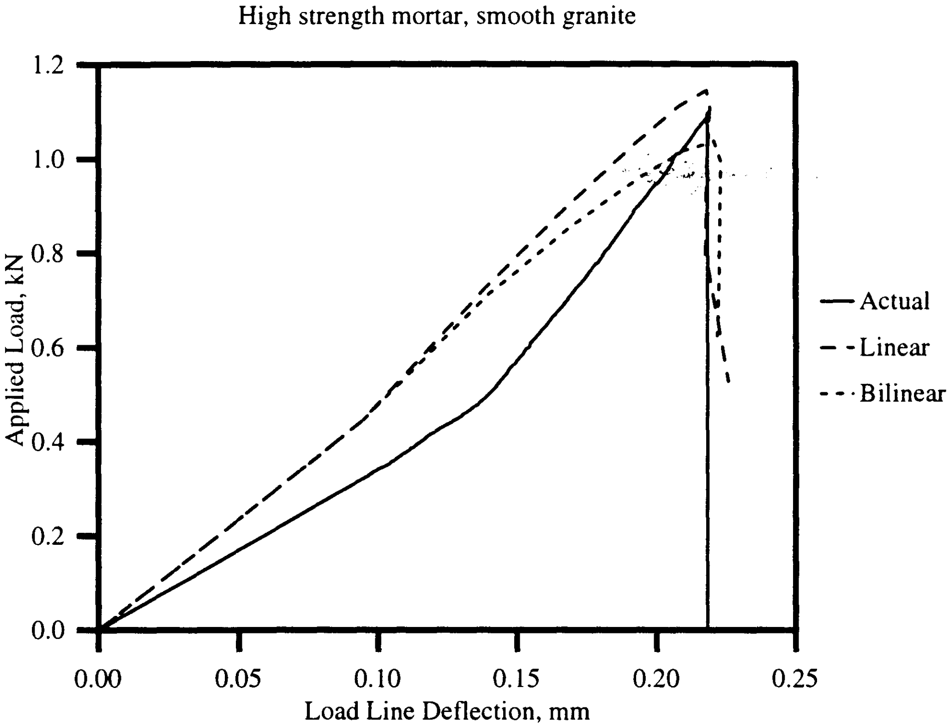

Figure 4-14: High strength mortar/smooth interface in mixed mode loading

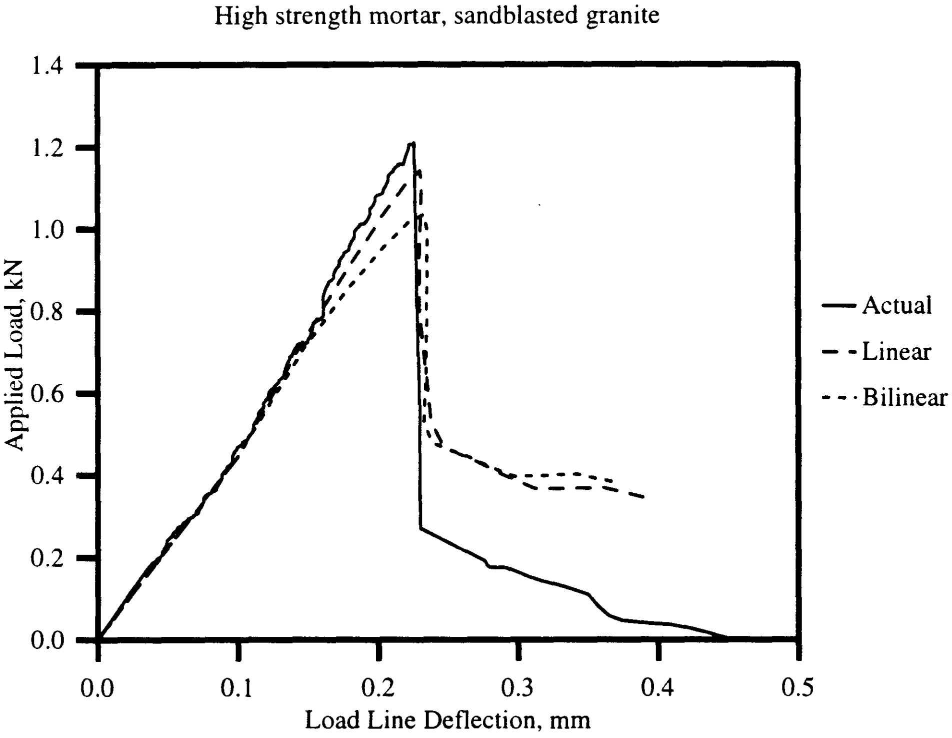

Figure 4-15: High strength mortar/sandblasted interface in mixed mode loading

most accurately model the test results (see Results section 4.5.2). This relationship was used as the mode I constitutive relationship in the mixed mode simulation to investigate the shear cohesive behavior. The load/load-line deflection curves for the mixed mode loading were simulated solely to investigate mode II strain softening behavior. Again both linear and bilinear models were used in the iterative modeling program (see Figure 4-9). The results from the mixed mode simulation are shown on Figures 4-13 through 4-15. In all simulations the mode I constitutive model was held as linear strain-softening. For mode II relationships the linear model was plotted with dashed lines and the bilinear was plotted with dotted lines.

4.5.2 Results

A comparison of the models show the linear relationship achieved a much more accurate simulation of the laboratory specimen behavior. The post peak behavior of the sandwich specimens were modeled well, especially in the mixed mode simulation. For mode I simulations the model suggested greater post peaking behavior than obtained in experimentation. However, a qualitative comparison shows that the behaviorial trends are similar to the experiments; i.e. relative post peak ductility is decreased with higher strength mortar and increased with surface roughness.

Mode II simulations also suggest that the shear stress softening behavior is linear. The brittleness of the interface is therefore significant even in mixed mode loading. Shear ductility was found to increase with the sandblasted surfaces. The effect of sandblasting is more pronounced in mixed mode loading. The rougher surface provides greater shear ship resistance through aggregate interlock; however, the increase in mode I displacements undermines the shear locking. It is theorized that higher shear versus tensile loadings may also increase ductility as well as interfacial strength.

4.6 Discussion

Perhaps most revealing about this investigation is the success of the linear strain-softening relationship. While mortars, aggregates, and even concretes have been

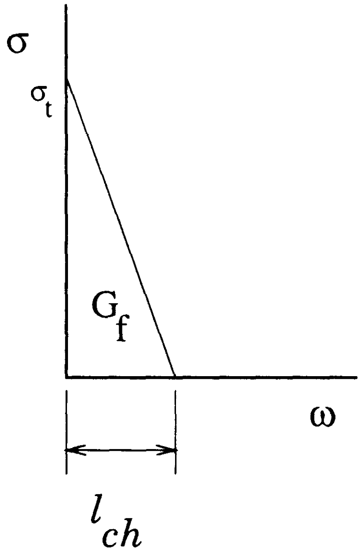

Figure 4-16: Characteristic length for linear contitutive relationship

modeled with bilinear strain softening, the interface of mortar and aggregate is a much less ductile linear relationship. The brittleness in concrete is often attributed to the interface, and here it is shown the relative significance of such a statement.

Since a linear strain softening relationship has successfuly modeled both tensile and shear deformations it is possible to make a quantitative comparison of interfacial brittleness. The success of the linear relationship demonstrates the model's sensitivity to the COD where cohesive forces terminate. This critical COD, defined here as a characteristic length l_{ch}, is a material parameter dependent on the fracture energy and ultimate tensile strength of the interface. For the linear consitutive model shown in Figure 4-16 the length is defined as

$$l_{ch} = \frac{2G_F}{\sigma_t}$$

where G_f, the fracture energy, was measured from the experimental results.

When this length is normalized by the compressive strength of the mortar, the critical crack opening displacement is found to decrease with higher strength mortars. Figure 4-17 shows the decrease in characteristic length with the three tested mortars

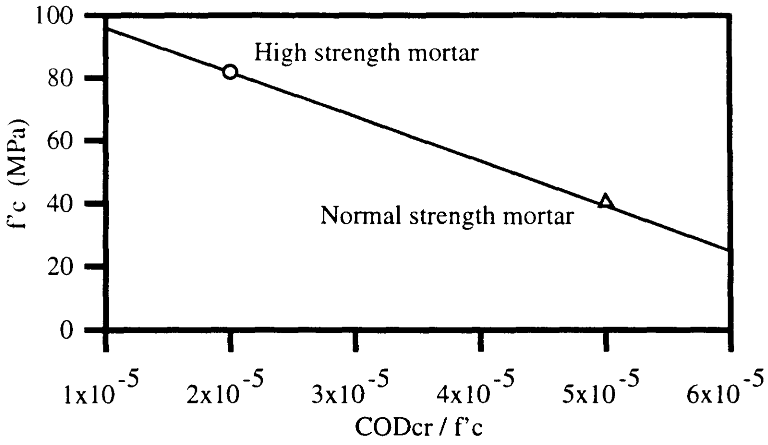

Figure 4-17: Normalized characteristic length and corresponding mortar strength

of this study. A similar comparison can be made for an increase in surface roughness while the mortar strength is held constant. Figure 4-18 plots the characteristic length for high strength mortar with smooth and sandblasted aggregate surfaces. The ductility of the interface and the characteristic length of these combinations increases with rougher aggregate surfaces. It is concluded that rougher aggregates will provide more ductile interfacial fracture.

The shear and tensile forces at one point on a mixed mode loaded interface are plotted with corresponding mode I COD in Figure 4-19. It is interesting to note that in mixed mode crack propagation the shear and tensile forces approach zero at approximately the same mode I COD. This observation points to the conclusion that the COD where cohesive forces reach zero is a good quantitative measure of interfacial brittleness in both shear and tensile tractions. For concrete this measure may be an appropriate description of the brittleness of concrete as a bulk material since the interfacial region is often viewed as the initiation of microcracking.

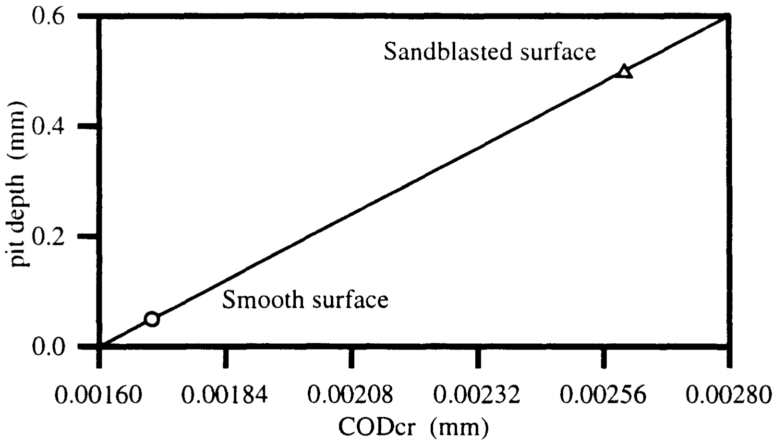

Figure 4-18: Characteristic length and corresponding surface roughness

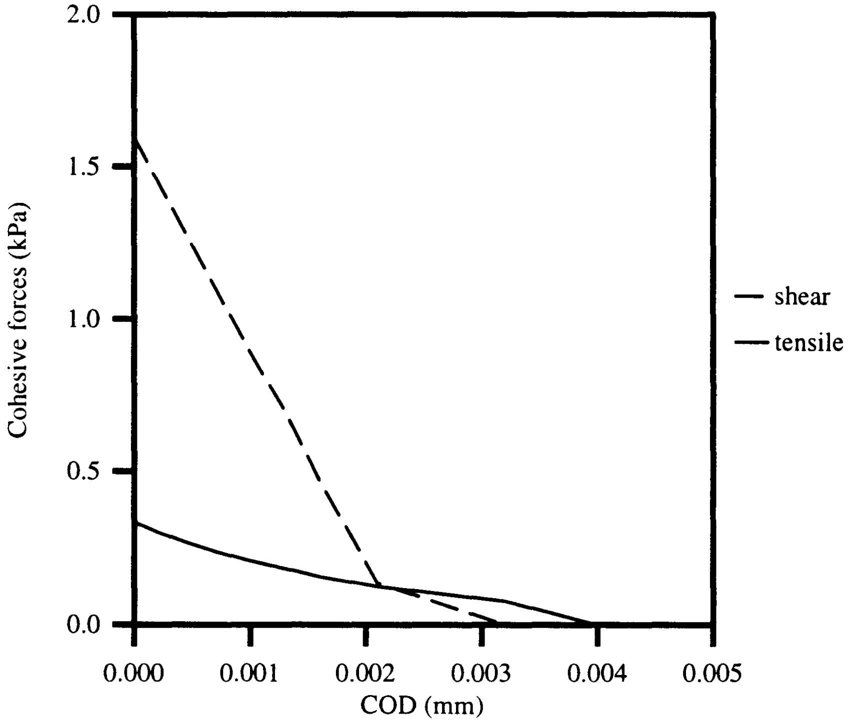

Figure 4-19: Shear and tensile cohesive forces with corresponding COD during fracture

4.7 Summary

The investigation of strain softening behavior resulted in successful modeling of interfacial crack propagation for both tensile (Mode I) strains and mixed mode stresses. Use of a linear strain–softening relationship was proven more accurate than bilinear in modeling both tensile and shear interfacial cohesive stresses. With the linear strain softening model cohesive stresses were studied and the ductility and characteristic length were shown to decrease with higher mortar strengths. Similarly, the ductility and characteristic length were shown to increase with aggregate surface roughness. Based on these findings it is suggested that a characteristic length defined as the mode I COD where tensile cohesion terminates be used as a quantifying measure of brittleness for interfacial crack propagation and perhaps even concrete. Brittleness is shown to decrease with rougher aggregate surfaces and increase with higher strength mortars.

Future work is needed to determine the effect of interfacial fracture properties on the ductility of concrete as a bulk material. Initially, however, the behavior of a crack approaching the interfacial region needs to be investigated to establish the validity of crack propagation criteria in mortar aggregate interfaces.

Chapter 5

Investigation of Interfacial Influence on Composite Beam Behavior

5.1 Introduction

In the pursuit of higher ductility high–strength concrete it is desirable to alter the characteristics of the interface to encourage propagation around the aggregate instead of through it. In doing so, the fracture behavior found in a normal strength concrete would be maintained with a high–strength concrete's mechanical properties, resulting in the desired high performance concrete. The key to altering the fracture behavior lies in the interface; therefore, an investigation of the influence of fracture parameters in this region on the behavior of the material is needed.

Due to a non–linear softening fracture behavior, normal strength concrete is considered a ductile material when compared to other brittle materials such as glass, ceramic, and some rocks. This ductility is attributable to the fracture process zone of the crack front; the process zone in normal strength concrete is due largely by the presence of aggregates. In this failure process, cracks are arrested and deflected to reduce the crack driving force and essence absorb energy. In this mode of failure aggregate properties are important factors [11, 38]. These failure mechanisms occur when the fracture toughness of the aggregate is greater than the fracture toughness of the interface. In high-strength concrete, the fracture toughness of the aggregate is often weaker than the fracture toughness of the interface. The failure mode changes to resemble a uniform material accompanied by brittle fracture. At this point properties of the coarse aggregate will significantly affect the toughening mechanisms in high-strength concrete; if an aggregate with fracture toughness higher than the high-strength interface were used a more ductile failure may be realized.

The process of accurately modeling a two-phase composite such as concrete involves consideration of relative properties of the two materials. It has been shown that crack propagation can be drastically altered from around an aggregate to through an aggregate when the fracture toughness of the interface is greater than that of the aggregate. To accurately represent propagation in concrete a model cannot be limited to considering only propagation through the aggregate; a simulation for propagation around the aggregate is also needed to complete the possible routes of crack propagation.

An analysis method to predict the fracture behavior of concrete based on fracture properties of its constituent materials is needed to evaulate the design of high-performance concrete. Several fracture models have been proposed to characterize the non-linear fracture behavior of concrete. These include the fictitious crack model [24], the crack band model [6], and the two parameter models [32]. These analysis methods and parameters are useful to evaluate the ductility of the softening material. However, there are no appropriate methods to predict the load-deflection curves with multi-phase softening composites such as high-strength mortar matrix with aggregate inclusions. Furthermore, a model for both crack propagation schemes of through the aggregate and around it is also needed.

This study investigates the influence of mortar, aggregate, and interfacial fracture properties on the performance of concrete composites. Relative fracture parameters and how they affect the behavior and ductility of the composite are studied in a combined experimental and analytical research program. For this, a variety of mortars, aggregates, and interfaces are tested through mortar beams with embedded circular aggregate inclusions. Analytical models are employed to simulate the fracture process of the tested physical specimens during failure. The models are used in parametric studies to investigate the influence of relative fracture properties of the mortar, aggregate, and interface on the deformation behavior of the composite.

5.1.1 Experimental Procedure

Introduction

For this study, circular inclusion beam specimens were tested to investigate interfacial fracture in concrete composites under three point bending mode I (tensile stresses). Three different mortar strengths were used with a circular inclusions of limestone and granite placed along the crack path in an initially cracked three–point bending specimen. An initial crack was created in the mortar matrix below the inclusion.

The testing parameters in this study were the mortar strength, the mode of crack propagation, and the aggregate surface roughness. All specimens were made using Type III cement to produce high early strength mortars. Tests were conducted in mode I three point bending. Smooth and sandblasted aggregate surface roughnesses were used to investigate how surface properties of the aggregate affect brittleness in the interfacial zone.

Materials

Three different strength mortars were combined with the aggregate inclusions to create the specimens. The mortars tested had strengths of 40.0 MPa, 58.6 MPa, and 83.7 MPa for low, medium, and high strength specimens. The medium and high strength mortars were made using a naphtalene sulfonate type superplasticizer and condensed silica fume in slurry form. The granite chosen was Chelmsford Granite, quarried by Fletcher Granite Co., Chelmsford, MA and the limestone was from Plymouth Quarries, Plymouth, MA. The mix proportions of the mortars are given in Table 5.1 and the properties of the materials are reported in Table 5.2.

Table 5.1: Mix proportions of mortars

Mix	W/(C+SF)	S/C	SF/C [%]	HRWR/C [%]
Low strength	0.50	2.0	0.0	0.0
Med strength	0.35	2.0	5.0	1.0
High strength	0.283	2.0	10.4	2.2
W-water, C-cement, S-sand, SF-silica fume, HRWR-high range water reducer				

Table 5.2: Material properties

Material	σ_c [MPa]	σ_t [MPa]	E [GPa]	ν	G_f [J/m^2]
Low strength mortar	40.0	2.8	27.8	0.2	39.0
Med strength mortar	48.6	3.2	32.5	0.2	43.2
High strength mortar	83.8	5.0	33.3	0.2	57.0
Granite	123.0	6.2	42.2	0.16	59.7
Limestone	57.5	3.1	34.5	0.18	29.2

The two roughnesses of the granite were characterized optically. Smooth surfaces were acheived solely by the diamond core bit cut; the surface was smooth to the touch with no visible scratches. The sandblasted surface acheived a pit depth of about 0.5 mm with an average grain diameter of about 3.0 mm.

Test Configuration and Loading

The three point bending configuration shown in Figure 5-1 was used. For each series of specimens six testing beams were cast. The dimensions of the single inclusion specimen were 300 mm × 75 mm × 25 mm. The relative initial crack length was held constant at 1/3 the beam depth. This crack was created with a thin diamond saw cut one day before the specimens were tested. The specimens were tested at the age of 7 days on a 1–kip Instron testing machine. The load/load–line deflection curves from this Instron machine were obtained with 0.1 mm accuracy.

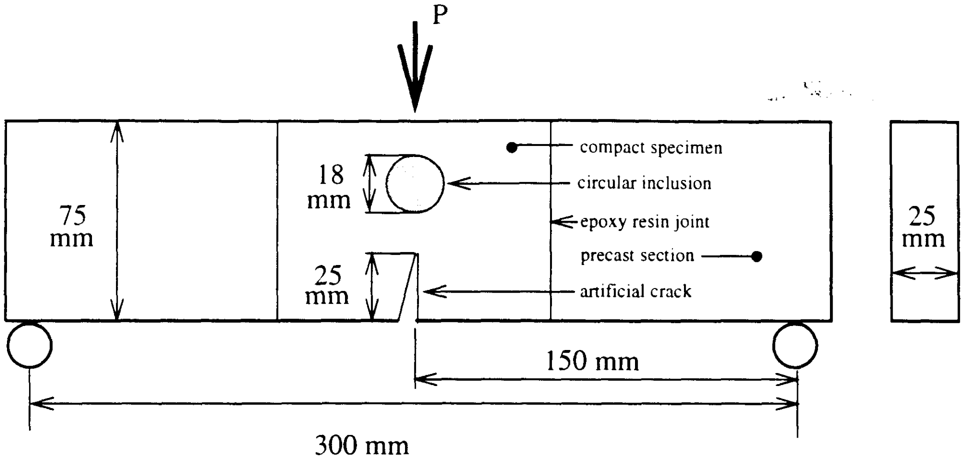

Figure 5-1: Three point bending loading used on circular inclusion specimens

Results of Experimental Program

The average failure loads P_u^{avg} for the valid tests are reported in Table 5.3. A central portion from a sample beam is shown in Figure 5-2. Load/load–line displacement curves for samples from each tested series are shown in Figure 5-4. The post–peak failure shape of these curves provide a qualitative comparison of the ductility of the various interfaces. Load/load–line displacement curves for samples from the specimens with one inclusion are shown in Figure 5-4(a). Central portions from samples of these testing series showing crack deflection and aggregate penetration are shown in Figure 5-3. The loading deflections show a decrease in post peak behavior with stronger mortars; these interfaces can be said to be more brittle. It is also observed that more ductile post–peak behavior is demonstrated by samples with sandblasted surfaces. This behavior may be attributable to the increased shear resistance of the rougher surface. These differences in behaviors of the specimens with different interfacial fracture properties indicate that the interface has a significant influence on the fracture of the concrete composite. To further study this influence, an analytical procedure was conducted.

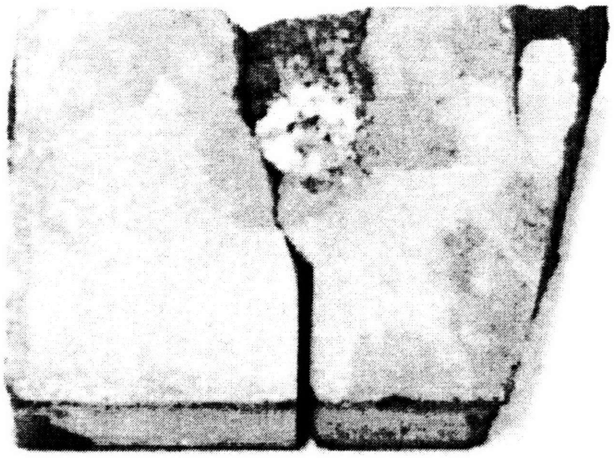

Figure 5-2: Sample specimen from the tested series

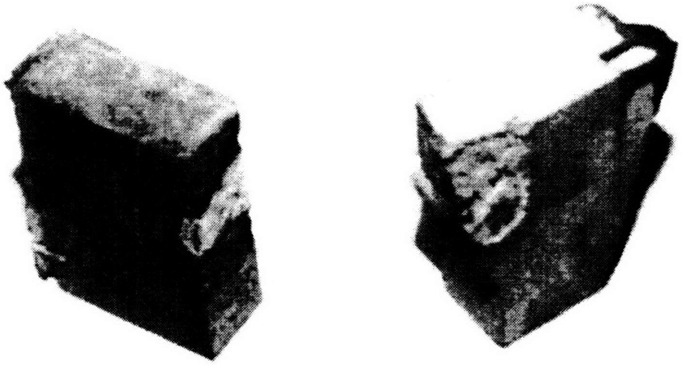

Figure 5-3: Sample specimens from the one inclusion testing series

Table 5.3: Fracture loads of the tested specimens

Series	Type of Aggregate	Mode of Failure	P_u^{avg} [kN]
Low strength/smooth	Granite	Interfacial	0.6150
Medium strength/smooth	Granite	Interfacial	0.6217
High strength/smooth	Granite	Interfacial	0.6377
Low strength/sandblasted	Granite	Interfacial	0.5664
Medium strength/sandblasted	Granite	Interfacial	0.6166
High strength/sandblasted	Granite	Interfacial	0.6655

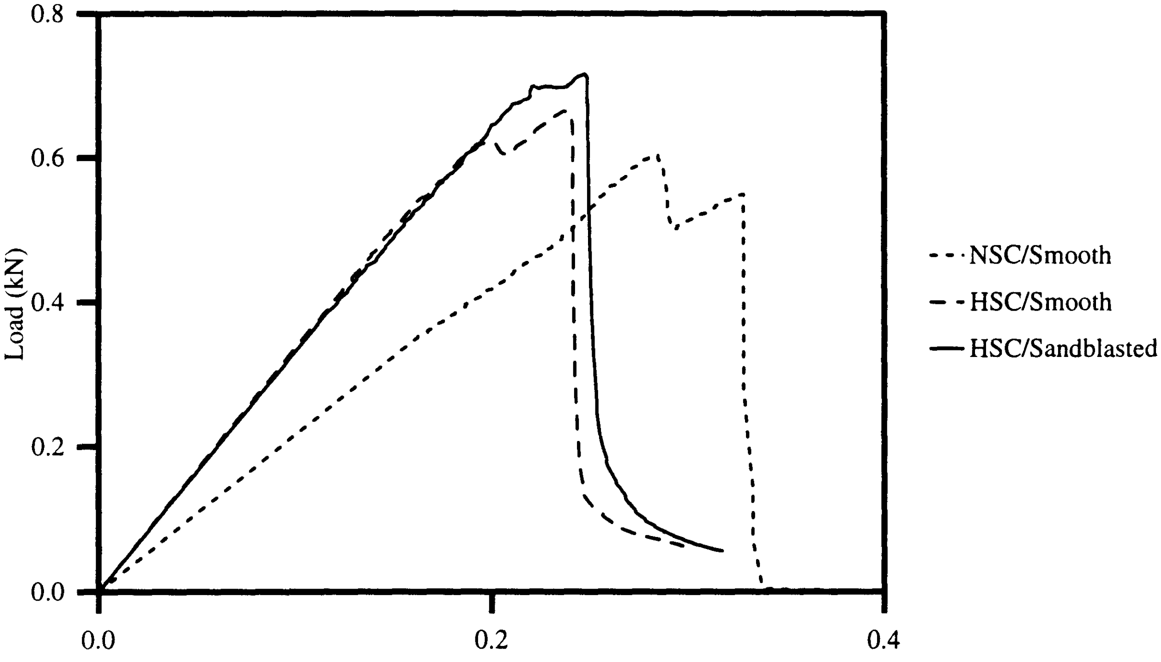

Figure 5-4: Experimental load/load–line deflection diagrams

5.2 Analytical Procedure

A cohesive force model similar to the analysis performed in earlier chapters was used to investigate the influence of interfacial and aggregate fracture properties on the performance of the tested composites. The implementation of a cohesive force model requires stress intensity factors for a series of crack propagation steps that represent a discretization of fracture around a circular inclusion. Each of these 'steps' represents the geometry of a hairline crack along the crack path up to the ending point of the crack. A cohesive force model relies on the integration of fictitious cohesive forces trailing the crack tip in an equilibrium with the external force. Because of this integration, several finite element simulations were conducted to investigate the stress intensities created as a crack propagates around a circular inclusion.

5.2.1 Finite Element Investigation

Over the last decade or so, the finite element method has become firmly established as a standard procedure for the solution of practical fracture problems. A number of techniques have been suggested for evaluating stress intensity factors from finite element results but adequate representation of thes crack tip singularity is a problem common to most of these methods. The use of finite elements in fracture predictions requires two distinct considerations:

> *Crack tip singularity modelling.* Initial studies involving the use of finite element methods in fracture mechanics employing conventional constant stress elements concluded that extremely fine mesh subdivision near the stress concentration was necessary for accurate results. The development of higher–order elements, such as the isoparametric family, permitted the same order of accuracy to be achieved with coarser mesh subdivisions. However, for efficient numerical solutions of fracture problems it is advantageous to develop special crack tip elements which directly model the asymptotic intensity near tip elastic strain field singularity. Though many versions employing both hybrid and displacement formulations have been

> developed to date, it is perhaps more important to note that it is not entirely necessary to completely model the crack tip singularity, as will be seen later.
>
> *Interpretation of the finite element results.* After displacement and stress fields have been determined in the model, a method for calculating the stress intensity factor must be developed. The most obvious approach is to relate the analytical solutions for the near tip stress and displacement fields to the values obtained from the finite element analysis. This technique, employed in this study, requires exrapolation procedures to obtain useful results. Other methods include the strain energy release rate and virtual crack extension methods. Another approach is to derive the stress intensity factors from the value of a path independent intergral. The line integral which has been used most often is Rice's *J-integral.*

The use of these methods has the distinct advantage that an exact modelling of the crack tip stress and displacement fields is not necessary and accurate results can be obtained by the use of relatively coarse meshes of conventional elements.

Displacement Extrapolation

The analytical expressions for the displacement variation along radial lines emanating from the crack tip are given by Equation 5.1

$$\begin{aligned} u &= \frac{K_I}{4\mu}\sqrt{\frac{r}{2\pi}}\left[(2\kappa-1)\cos\frac{\theta}{2}-\cos\frac{3\theta}{2}\right]-\frac{K_{II}}{4\mu}\sqrt{\frac{r}{2\pi}}\left[(2\kappa+3)\sin\frac{\theta}{2}+\sin\frac{3\theta}{2}\right] \\ v &= \frac{K_I}{4\mu}\sqrt{\frac{r}{2\pi}}\left[(2\kappa+1)\sin\frac{\theta}{2}-\sin\frac{3\theta}{2}\right]+\frac{K_{II}}{4\mu}\sqrt{\frac{r}{2\pi}}\left[(2\kappa-3)\cos\frac{\theta}{2}+\cos\frac{3\theta}{2}\right] \end{aligned} \tag{5.1}$$

Substituting the values of u or v and r for nodal points along a radial line emanating from the crack tip as shown in Figure 5-5 allows a plot of K_I and K_{II} against radial distance r. By discarding the results for points very close to the crack tip (where maximum error would be expected) the solutions can be extrapolated to $r = 0$.

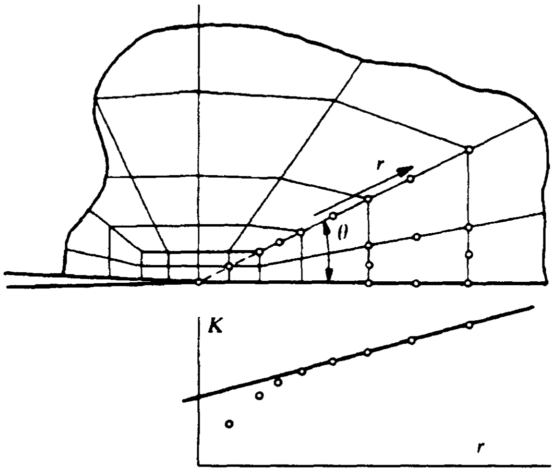

Figure 5-5: Nodes used for displacement extrapolation equations

Implementation

One aspect of this investigation was to develop a computer algorithm to evaluate stress intensity factors based on displacement extrapolation. This technique was employed with conventional isoparametric elements. It has the distinct advantage that combined mode behavior could be separated into K_I and K_{II} components. This ability proved important later. This is also not possible with energy methods or line integral techniques mentioned earlier.

This subroutine evaluates the stress intensity factors and requires definition of radial direction along which extrapolation is to take place. Stress intensity factors are evaluated for each nodel point along the chosen radius; these values are then plotted and extrapolated to $r = 0$. The final algorithm includes this code:

```
   '*** Calculate elastic factor for plane stress or plane strain.
If frmGraphics.optPlaneStress.Value = True Then

   kappa = (3# - pois1) / (1# + pois1)
Else

   kappa = 3# - 4# * pois1
End If

rootp = Sqr(2 * 3.14159)
```

```
   '*** Lefthand side of Equation 5.1.
denmuI = (2# * kappa - 1#) * Cos(theta / 2#) - Cos(1.5 * theta)
denmvI = (2# * kappa + 1#) * Sin(theta / 2#) - Sin(1.5 * theta)

   '*** Calculate transformed displacements.
dispu = pcord(sifnode, 1) * Cos(phi) + pcord(sifnode, 2) * Sin(phi)
dispv = pcord(sifnode, 2) * Cos(phi) - pcord(sifnode, 1) * Sin(phi)

   '*** Define some sort of tolerance and calculate Mode I stress intensity
factor.
If Abs(denmuI) > tol Then sfacuI = 4 * shear * rootp * dispu / (denmuI *
Sqr(b))
If Abs(denmvI) > tol Then sfacvI = 4 * shear * rootp * dispv / (denmvI *
Sqr(b))

   '*** Assure no division by zero.
If theta < .01 Then sfacvI = 0#
If theta > 3# Then sfacuI = 0#

   '*** Mode II stress intensity factor.
denmuII = -(2# * kappa + 3#) * Sin(theta / 2#) - Sin(1.5 * theta)
denmvII = (2# * kappa - 3#) * Cos(theta / 2#) + Cos(1.5 * theta)

   '*** Tolerance.
If Abs(denmuII) > tol Then

   sfacuII = 4 * shear * rootp * dispu / (denmuII * Sqr(b))
Else

   sfacuII = 0#
End If

If Abs(denmvII) > tol Then

   sfacvII = 4 * shear * rootp * dispv / (denmvII * Sqr(b))
Else

   sfacvII = 0#
End If

If theta < .01 Then sfacuII = 0#
If theta > 3# Then sfacvII = 0#
```

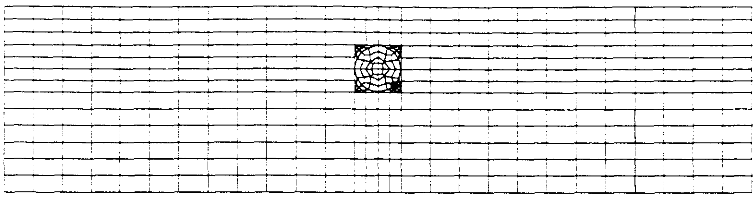

Figure 5-6: Finite element discretization of the circular inclusion specimen

5.2.2 Results of Finite Element Investigation

A cohesive force model requires several integrations of cohesive forces trailing the crack tip along the crack path. For this reason, permutations of finite element simulations was conducted with the mesh shown in Figure 5-6. As the crack progresses around the inclusion stress intensity factors are needed for cohesive forces at each node along the crack path.

Because crack propagation around a circular inclusion is not symmetric, both global forces and cohesive forces will result in mode I and mode II stress intensities at the crack tip. The results of the finite element investigation are presented in Tables 5.4 through 5.8. The results are tabulated into divisions representing various stages of crack propagation around the 8 discretized inclusion nodes shown in Figure 5-7. Simulations for cohesive forces trailing the crack tip are notated by the location of the force (in terms of the degree of the node it is located) and the fracture mode the force represents (*i* for mode I and *ii* for mode II forces). Each entry in these tables represents a separate simulation run on one of MIT's Athena workstations.

A plot of the phase angle with respect to the location of the crack around the inclusion is shown in Figure 5-8. It is interesting to note the increase in mode II

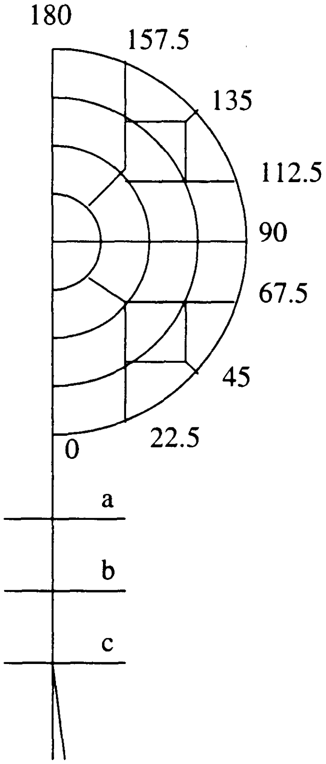

Figure 5-7: Degree notation of the circular inclusion specimen

Table 5.4: Results of finite element investigation (crack position 0°–67.5°)

Crack Position	Load Position	K_I	K_{II}
22.5	0i	2.36	2.77
	0ii	0.67	0.74
	ai	0.67	0.74
	aii	2.36	2.77
	bi	0.49	1.32
	bii	2.23	1.45
	ci	0.64	1.45
	cii	2.02	1.02
	P	0.33	1.41
45	22.5i	1.51	5.32
	22.5ii	0.21	1.10
	0i	2.08	3.96
	0ii	0.94	2.65
	ai	0.94	2.65
	aii	2.08	3.96
	bi	0.81	2.30
	bii	2.09	4.01
	ci	0.92	2.59
	cii	1.99	3.77
	P	0.33	1.41
67.5	45i	1.20	1.42
	45ii	0.99	1.91
	22.5i	1.82	0.61
	22.5ii	0.95	2.04
	0i	1.52	0.50
	0ii	1.47	2.18
	ai	1.431	1.341
	aii	1.478	0.620
	bi	1.250	1.186
	bii	1.633	0.564
	ci	1.268	1.107
	cii	1.648	0.446
	P	0.38	1.12

Table 5.5: Results of finite element investigation (crack position 90°–112.5°)

Crack Position	Load Position	K_I	K_{II}
90	67.5i	1.12	3.46
	67.5ii	0.33	1.59
	45i	1.85	2.34
	45ii	0.90	2.32
	22.5i	1.35	1.15
	22.5ii	1.37	2.81
	0i	0.87	0.22
	0ii	1.74	3.03
	ai	1.74	3.03
	aii	0.87	0.22
	bi	1.56	2.92
	bii	1.06	0.18
	ci	1.54	2.89
	cii	1.10	0.08
	P	0.43	1.19
112.5	90i	1.49	12.85
	90ii	0.55	2.67
	67.5i	1.98	10.84
	67.5ii	1.19	5.00
	45i	1.29	5.11
	45ii	1.73	8.09
	22.5i	0.69	1.06
	22.5ii	2.09	9.68
	0i	0.09	1.76
	0ii	2.13	9.87
	ai	2.13	9.87
	aii	0.88	2.81
	bi	1.93	9.37
	bii	0.30	2.00
	ci	1.89	9.15
	cii	0.35	1.71
	P	0.52	3.16

Table 5.6: Results of finite element investigation (crack position 135°)

Crack Position	Load Position	K_I	K_{II}
135	112.5i	1.53	10.24
	112.5ii	0.14	2.56
	90i	1.67	7.23
	90ii	1.16	5.60
	67.5i	1.06	3.85
	67.5ii	1.68	7.97
	45i	0.39	0.64
	45ii	1.99	8.92
	22.5i	0.26	2.92
	22.5ii	1.99	11.11
	0i	0.77	6.04
	0ii	1.69	8.76
	ai	1.69	7.58
	aii	0.77	5.08
	bi	1.56	6.94
	bii	0.565	3.876
	ci	1.52	6.73
	cii	0.523	3.722
	P	0.49	2.12

Table 5.7: Results of finite element investigation (crack position 157.5°)

Crack Position	Load Position	K_I	K_{II}
157.5	135i	2.33	1.95
	135ii	0.50	2.07
	112.5i	1.98	0.84
	112.5ii	1.51	2.50
	90i	1.30	0.41
	90ii	1.57	6.16
	67.5i	0.50	1.90
	67.5ii	2.57	2.67
	45i	0.38	2.98
	45ii	2.58	1.78
	22.5i	1.15	3.65
	22.5ii	2.24	1.41
	0i	1.62	3.88
	0ii	1.59	1.18
	ai	1.59	0.88
	aii	1.62	3.88
	bi	1.45	0.67
	bii	1.41	4.04
	ci	1.42	0.65
	cii	1.36	4.06
	P	0.50	0.43

Table 5.8: Results of finite element investigation (crack position 180°)

Crack Position	Load Position	K_I	K_{II}
180	157.5i	2.12	4.27
	157.5ii	0.30	2.66
	135i	2.54	3.30
	135ii	2.02	4.10
	112.5i	1.67	1.46
	112.5ii	2.87	4.88
	90i	0.61	0.26
	90ii	3.42	6.04
	67.5i	0.45	2.52
	67.5ii	3.46	3.97
	45i	1.46	4.40
	45ii	3.07	2.37
	22.5i	2.21	6.29
	22.5ii	2.30	0.25
	0i	2.47	6.82
	0ii	1.24	0.09
	ai	1.24	0.09
	aii	2.47	5.90
	bi	1.11	0.12
	bii	2.19	5.84
	ci	1.10	0.13
	cii	1.91	5.78
	P	0.34	0.72

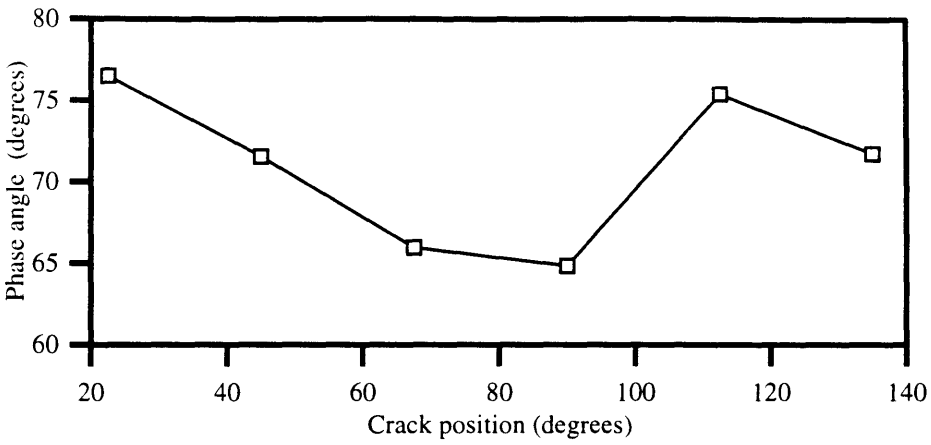

Figure 5-8: Phase angle at discretized nodes around the inclusion

contribution as the crack continues around the inclusion; this may explain why many crack paths 'kink' into the mortar instead of propagating completely around an inclusion. Specifically, note the jump in phase angle at position 135°. Given the fracture toughness curves of most interfaces, this would indicate an increased resistance to propagation along the interface at this point. In fact, kinking out of the interface into the mortar at this point was often observed in testing these specimens. An analysis of the interfacial fracture energy at points along the interface around an inclusion will reveal the point where the crack will kink out due to a lower fracture resistance in the mortar in any geometry.

5.3 Computational Simulation

The investigation of the load–deflection behavior of the circular inclusion testing specimen includes the modified Hillerborg model and both linear and bilinear constitutive relationships for the different phases. Simulations of the load/load-line displacement diagram of circular inclusion specimens in three-point bending is made available through an iterative computer model.

The relation of external load and displacement is obtained by solving the equations of the net stress intensity factor (K_e), the equilibrium of crack opening displacement (COD) at crack surface, and the constitutive function of the COD and cohesive stress. For the calculation of the crack opening displacements a K-superposition method was employed. In the mixed-mode fracture found in the circular inclusion specimens the K-superposition will include both tensile and shear cohesive forces. Figure 5-9 shows that there are three contributions to K_e. One is the stress intensity factor due to the applied load (P), K_p; the others, K_{r_I}, is due to the cohesive tensile forces $\sigma(x)$ and $K_{r_{II}}$, is due to the cohesive shear forces $\tau(x)$ acting across the crack faces in the process zone where the material is softening. Here the external load (P) is divided among load for mode I COD and load for mode II COD. Now the mixed mode stress intensity factor may be expressed as

$$K_e = (K_{p_I} + K_{r_I}) + i(K_{p_{II}} + K_{r_{II}}) \tag{5.2}$$

Following in a similar manner the COD is given by

$$\delta = (\delta_{P_I} + \delta_{r_I}) + i(\delta_{P_{II}} + \delta_{r_{II}}) \tag{5.3}$$

Now equations are needed to relate the mixed mode three point bending load to

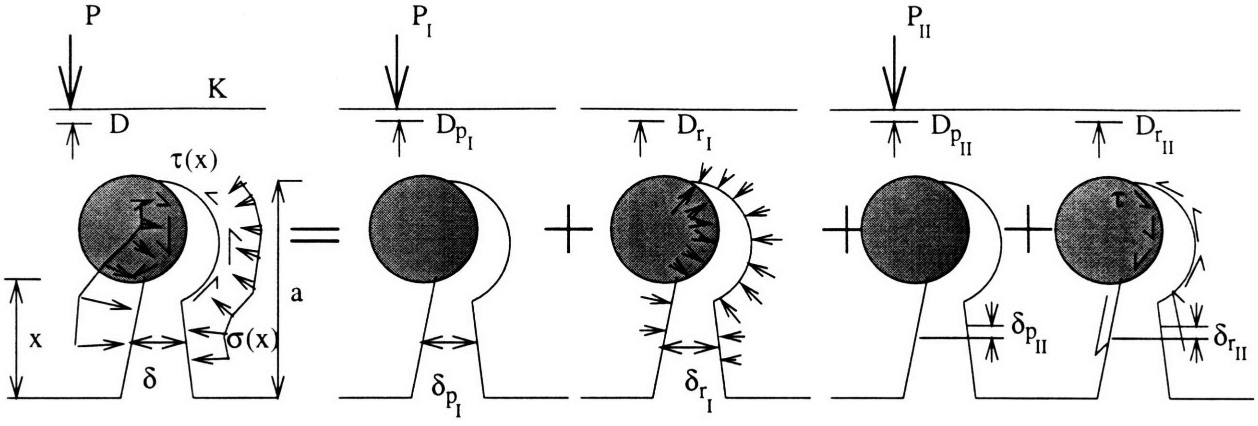

Figure 5-9: Stress intensity superposition for circular inclusion specimens

the cohesive stresses. By substituting the stress intensity equilibrium into the COD equilibrium the relationship between the COD and cohesive stresses is obtained

$$\delta = \delta_I + i\delta_{II} = \frac{2}{E^*}\left[\int_0^a \sigma(a,c)H_I(a,x,c)dc + i\int_0^a \tau(a,c)H_{II}(a,x,c)dc\right] \qquad (5.4)$$

where

$$H_I(a,x,c) = \frac{G_I(a,c)}{F_I(a)}\int_x^a F_I(z)G_I(z,c)dz - \int_c^a G_I(z,x)G_I(z,c)dz$$

and

$$H_{II}(a,x,c) = \frac{G_{II}(a,c)}{F_{II}(a)}\int_x^a F_{II}(z)G_{II}(z,c)dz - \int_c^a G_{II}(z,x)G_{II}(z,c)dz$$

where G_I, G_{II}, F_I, and F_{II} are stress intensity factors given by the finite element investigation described above.

To integrate the stress intensity factors G_I, G_{II}, F_I, and F_{II}, a psuedo–integration was achieved by summing the stress intensity factors for a given crack position multiplied by a tributary area at that position. Cohesive forces existed at the three nodes below the inclusion (which had a tributary area of $\left[\left(2'' - \frac{3}{4}''\right)/2\right]/3 = 0.208''$) and each of the eight nodes around the inclusion (a tributary area of $\left(\pi * \frac{3}{8}''\right)/8 = 0.147''$). This step of the program relied on MATLAB's matrix handling capabilities.

Constitutive relationships for the constituent materials are needed. The tensile relationship and the shear relationship for the interfacial nodes are given by the linear relationship proven successful in the interfacial constitutive relationship investigation, above. A bilinear tensile relationship was used for the mortar and aggregate nodes, as shown successful by Dr. Kitsutaka [35]. Now the crack opening displacements can be solved for a given crack length and cohesive forces.

Again the solution here is iterative in the same manner as all cohesive force simulations. An agreement can be found between the crack opening displacements and the cohesive stresses. When they are in equilibrium the external three point bending load is found as the sum of the load creating mode I stresses and the load creating mode II stresses.

$$P = P_I + P_{II}$$

Similarly the three point bending displacement is found as the sum of the displacement due to mode I tractions and the displacement due to mode II tractions.

$$D = D_I + D_{II}$$

5.4 Results of Analytical Models

The load/load–line deflection curves for the interfacial propagation tests were simulated first. From each set of experimental tests a representative sample was chosen to model. The chosen sample was closest to the fracture load and ductility behavior of the group it came from. From previous experimental work (above) the fracture energy (G_{f_i}) and the rupture stress (f'_{t_i}) of the interface was calculated and the fracture energy (G_{f_m}) and the rupture stress (f'_{t_m}) of the mortar was calculated from material parameters testing in this experimental series. These material constants were used as parameters in the modeling program. The results from the simulations are shown in Figures 5-10 to 5-12. The analytical strain–softening model results are plotted with dashed lines while the experimental results are given as solid lines.

The results of the interfacial simulation program show a good approximation to the experimental model performance. However, in some of the cases is it seen that post–peak behavior is overestimated. This may be attributable to the fact that in many experimental models the crack was observed to 'kink out' at about the 'two o'clock' position on the circular aggregate. In the analytical model the crack was prescribed to continue around the aggregate at this point. Had the crack been simulated to kink out the geometry would have changed drastically because the crack would have propagated vertically upwards, making the specimen extremely more compliant and therefore reducing the post–peak behavior.

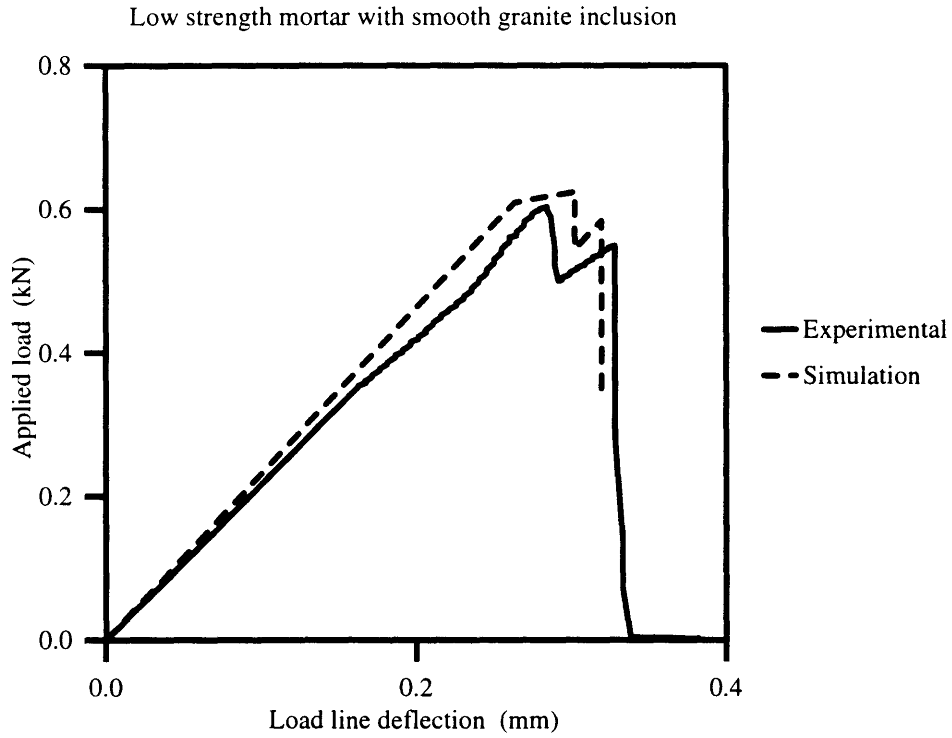

Figure 5-10: Results of simulation applied to normal strength/smooth interface specimen

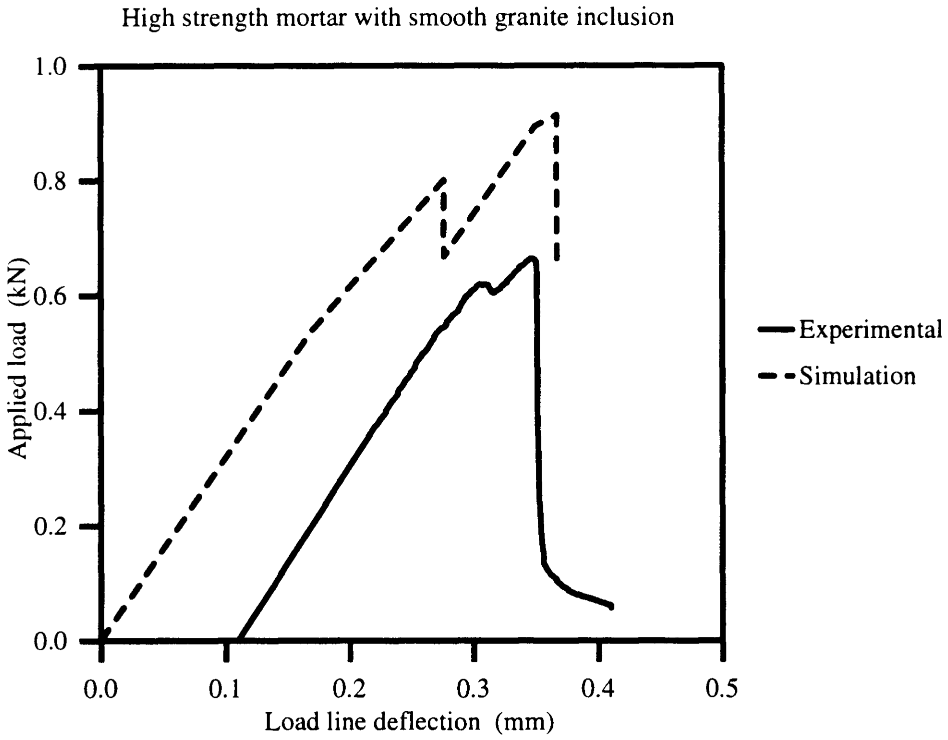

Figure 5-11: Results of simulation applied to high strength/smooth interface specimen

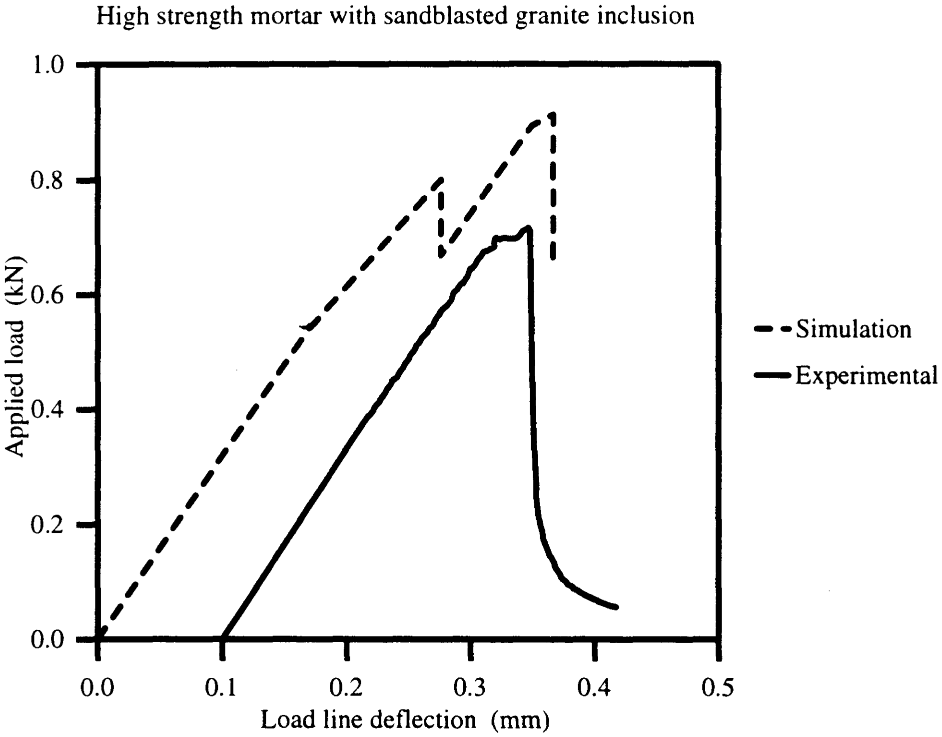

Figure 5-12: Results of simulation applied to high strength/sandblasted interface specimen

5.5 Fracture Parameters Influencing Crack Paths and Ductility

Since the results have been shown to successfully model the physical behavior of the composite specimens, the analytical models may be used to study in a qualitative manner the effect of the material parameters on the composite behavior. Parameters useful to study in the interfacial model include the relative fracture energy of the interface G_{f_i} to that of the mortar G_{f_m} as $P = G_{f_i}/G_{f_m}$ and relative tensile strength of the interface σ_{t_i} to that of the mortar σ_{t_m} as $T = \sigma_{t_i}/\sigma_{t_m}$. Figures 5-13 and 5-14 show the results of such a parametric study for the load/load–line displacement curves of beam specimens with normal strength mortar. In this numerical calculation P and T were varied and interfacial cracking was prescribed for all cases (i.e., $D < D_c$).

As shown in this parametric study, the parameter P directly affects the ductility of the interfacial cracking region of the LLD plot. It can be concluded from the study that a lower relative fracture energy is desirable from the interface. Perhaps this could be achieved through chemical or mechanical means such as less reactive aggregates or an aggregate with a specially treated surface such as the smooth aggregate used in this study.

Also shown in this parametric study is the volatile influence of the parameter T. This parameter drastically affects the performance of the fracture. It may be noted, however, that the values used in the tensile parametric study are more drastic than the values in the energy study; additionally, it can be oberved that some of the tensile strengths used are practically impossible. More work into the study of this parameter

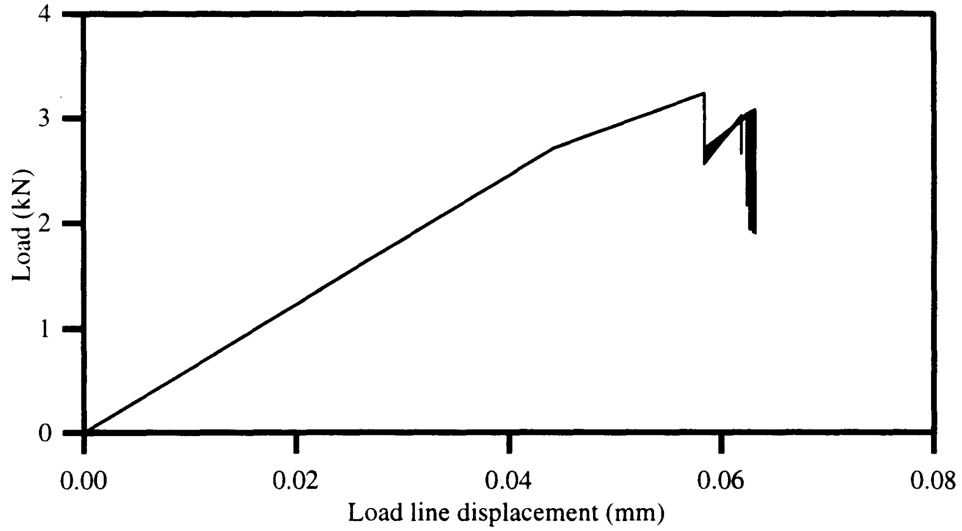

(a) Global values for parametric P study

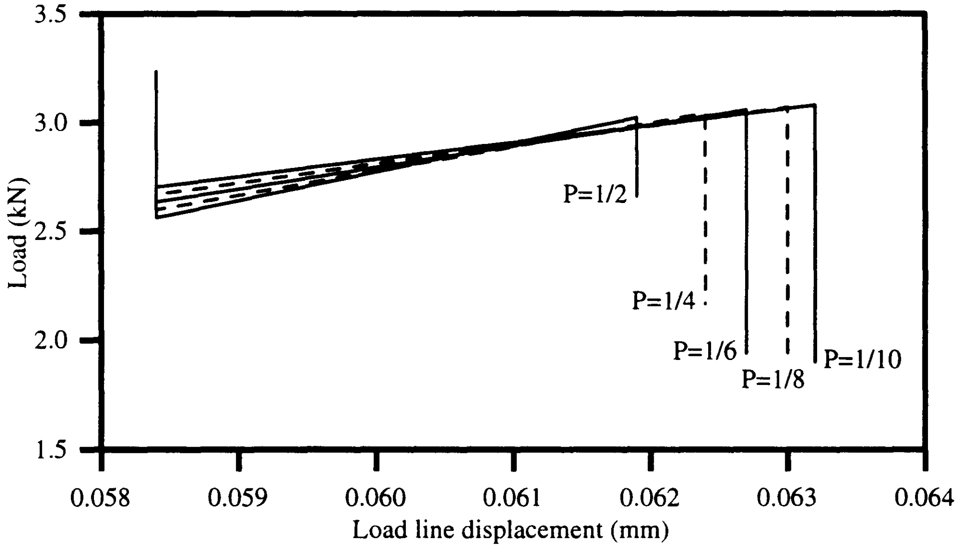

(b) Close–up of the post–peak zone

Figure 5-13: Results of parametric study for parameter P

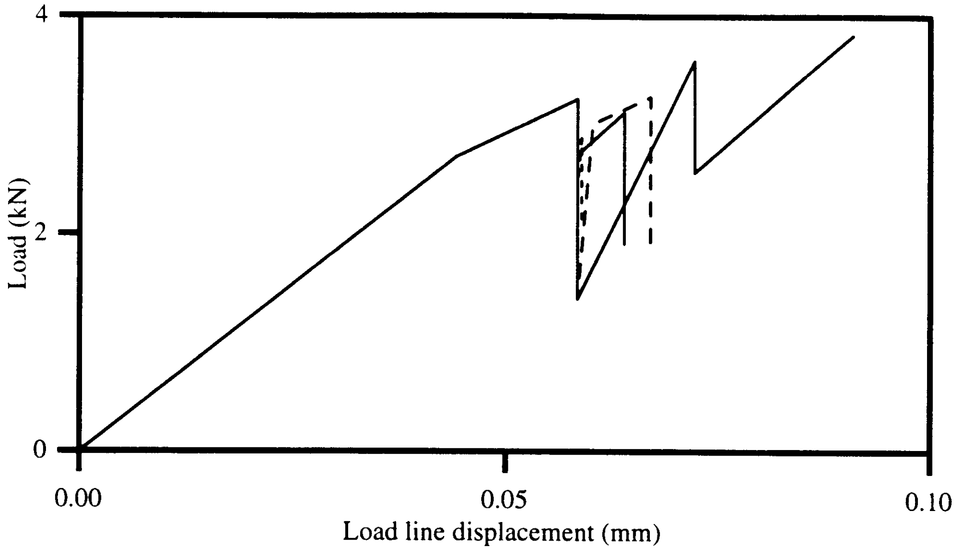

(a) Global values for parametric T study

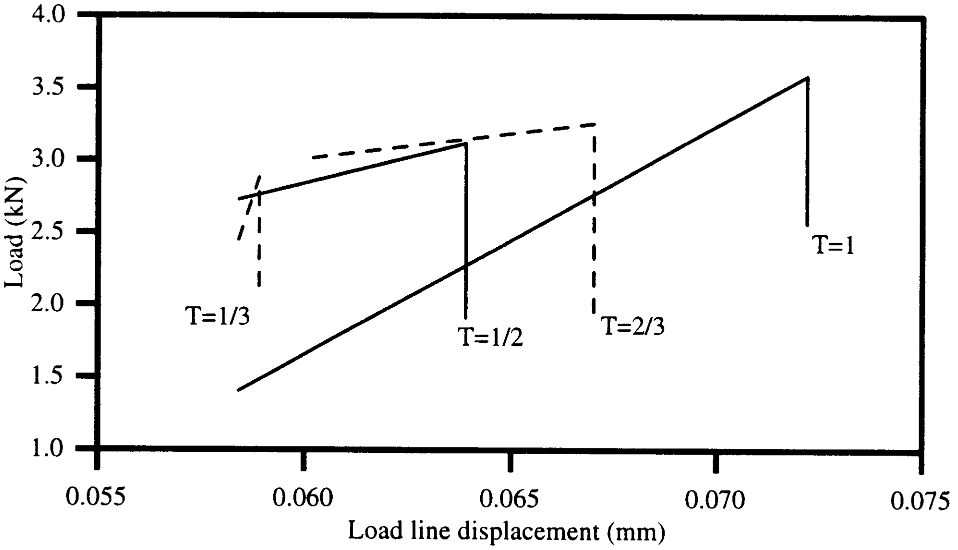

(b) Close–up of the post–peak zone

Figure 5-14: Results of parametric study for parameter T

is needed.

5.6 Summary

The implementation of newly discovered interfacial strain–softening behavior with previously implemented mortar strain–softening behavior resulted in successful modeling of the circular interfacial composite specimen. Use of a linear strain–softening relationship was proven to accurately model the behavior of the interface in the composite. With the linear strain softening model cohesive stresses were studied and the ductility and characteristic length were shown to decrease with higher mortar strengths. Similarly, the ductility was shown to increase with aggregate surface roughness. A parametric study of the relative influence of interfacial fracture parameters shows that the ductility of the composite model is related to the fracture energy and tensile strength of the interface. This analysis method is considered applicable to developing an ideal formulation for high–performance concrete.

Future work is needed to apply these models to real concrete. A comparison should also be made between the relative behavior of the two models to achieve an overall understanding of the behavior of the composite influenced by the relative interfacial and constituent properties. This global model could then be used to optimize a high–performance concrete based on its constituent properties.

Chapter 6

Influence of Mortar–Aggregate Interfaces and Aggregate Properties on Real Concrete

The ductility and failure behavior of cementitious composites have been shown to be affected by the fracture properties of the constituent materials and the properties of the interfaces between these materials. In the previous chapter, composite models were shown to be affected by the properties of the mortar–aggregate interface, while Kitsutaka (1993) has shown that similar models were affected by aggregate properties when fracture propagated through the aggregate. In this chapter, the role of mortar–aggregate interfaces in the development of high strength concrete with optimum strength and ductility will be examined. In light of the limitations inherent in the previous composite model studies, qualitative correlation of the results of the model studies to the behavior of the real concrete will be made. Results and techniques developed from the previous research phases will be extended to assess the influence of constituent material parameters on the performance of real concrete. These parameters include interfacial and constituent fracture energies of the materials and aggregate volume fraction and maximum aggregate size. This chapter describes work performed in conjunction with other researchers [34].

6.1 Material Design of High Performance Concrete

The general purpose of high performance concrete mix designed for a specific contract and use is to select materials and their proportions which will meet, economically, the properties of a desired high performance construction material in both the fresh and hardened states. For concrete in general, the design process has been refined into stages [15]:

1. *Materials Selection*

   To select materials which will combine to give desired behavior of the specified material.

2. *Mix Proportioning*

   To select relative proportions to produce desired characteristics of both wet and dry concrete.

To determine the total quantities of materials and optimize cost based on relative rates of these materials.

To produce batch data for the production of all possible mixes and volumes.

3. *Mix Selection*

   To select the most appropriate mix to meet specified material characteristics, taking account of the latest feedback from the quality control systems.

   To provide additional data for special mix designs not covered above.

High strength concrete is characterized by greater strength and improvements to other properties such as permeability, durability, and stiffness; however, it is also typically more brittle than normal strength concrete, limiting its application in flexural members. In the past, ductility has been improved in concrete through the addition of fibers. However, fiber reinforced concretes are often costly in terms of materials and manufacturing processes; therefore, there is increased interest in the development of a high strength concrete with improved ductility characteristics through control of constituent material properties and admixtures.

6.1.1 Compressive Strength

In recent years, interfaces between the mortar matrix and the aggregates in concrete have been shown to strongly influence the mechanical properties of the global material [26, 48, 10]. In high strength concretes incorporating silica fume the alterations to the mortar–aggregate interfacial zone have been shown to improve the transfer of stresses from the matrix to the aggregate, allowing more contribution from the aggregate to load resistance [38, 14, 56]. It has been shown that these stronger interfaces can enhance the strength, stiffness, and durability of the cementitious material [7]. However, there are many contradictory results and conclusive information on the role of interfaces in concrete compressive strength is not widely available.

Aggregate properties are key elements in determining the compressive strength of concrete. Several studies have been made of the effects of aggregates on the strength and elastic modulus of high strength concrete [43, 2]. However, it is important to recognize that composite behavior of the concrete may also be just as influential. For example, compressive strength decreases with increasing pore size or total porosity and increases with reduced aggregate size, regardless of aggregate type. These effects are generally attributable to large inhomogeneties near the aggregate; the location of the largest aggregate particle is often associated with the largest flaw in the concrete. Since these pores and microcracks are responsible for crack initiation and propagation, the effect of the strength of the aggregate particle may be reduced by its geometric properties.

6.1.2 Tensile Strength

In the 1920's Griffith introduced a crack theory suggesting that cracks in materials will propagate if energy released by crack propagation is larger that the energy required to form new surfaces. The tensile stress of a material was given by

$$\sigma = \sqrt{\frac{\Gamma E}{\pi a}} \tag{6.1}$$

where $2a$ is the diameter of the largest flaw or pore, and Γ and E are the fracture energy and elastic modulus of the material. This equation, when applied to concrete, explains the improvements in strength with smaller flaws which can be controlled with smaller aggregates. It depicts concrete's tensile strength as a function of largest flaw size instead of total porosity. For this reason, many tensile strength equations of concrete as a quasi–brittle material have been introduced in terms of the fracture toughness (K_{I_c}) and a critical crack tip opening displacement ($CTOD_c$) [31, 33]

$$f_t = C_t \frac{(K_{I_c})^2}{E\ CTOD_c} \tag{6.2}$$

where C_t is a coefficient and E is the elastic modulus. This critical crack tip opening displacement is a representation of the material's critical flaw size. It is similar to the characterisitc length, introduced earlier, proposed by Hillerborg in 1980. This material characteristic was derived from a modification to the Griffith crack theory

$$f_t = \sqrt{\frac{\Gamma E}{l_{ch}}} \tag{6.3}$$

where the characteristic length, l_{ch}, now represents the material's critical flaw size. Rewriting this equation yields the characteristic length in terms of other material parameters

$$l_{ch} = \frac{\Gamma E}{(f_t)^2} \tag{6.4}$$

The characteristic length is the most commonly used quantitative measure of ductility in concrete. It relates the fracture energy, the stiffness, and the tensile strength to represent a critical material flaw size. Since it is also a measure of the deformation a concrete ligament can sustain before fracture, it is appropriate as a representation of ductility. It is noted that to improve the ductility of concrete the fracture energy and stiffness must be improved while decreasing the material's tensile strength.

6.1.3 Fracture Toughness

It is generally agreed that as the strength of concrete increases the ductility decreases, becoming more brittle. An increase in the strength of mortar–aggregate bonds may alter the fracture process of the material; crack penetration through the aggregates has been observed in high strength concrete, indicating a less pronounced effect of crack arrest by the aggregates and more global brittle behavior [13, 20]. However, in normal strength concrete the fracture path is generally twisted and tortuous. When a dominant crack intercepts an aggregate, it will most likely deflect around the aggregate because mortar–aggregate interfaces in normal strength concrete are generally weak. Deflection reduces the stress intensity at the new crack tip due to the new orientation, increasing the material toughness.

Introducing good interfacial bonding and smaller sized aggregates may change the mode of crack propagation in high strength concrete back to interfacial deflection. In this case, crack front trapping may occur, increasing the toughness of high strength concrete. Crack front trapping would hinder crack propagation at the particle site. The crack front would bow around the trap site and retard the propagation process. In crack front trapping mechanisms the concrete toughness has been found to increase as the volume fraction of aggregates increases [28]. The criteria governing the propagation of cracks through the aggregate or around in a crack trapping mechanism can be expressed through fracture mechanics, as will be discussed in the next section.

6.2 Crack Propagation at Mortar–Aggregate Interfaces in Real Concrete

It has been suggested that the mechanical properties of concrete are largely attributable to the properties of mortar–aggregate interface regions [21, 37]. Quantitative studies of interfacial fracture processes through interface fracture mechanics concepts offer great potential for the understanding of the global material behavior of concrete. The main objectives of interface fracture mechanics applied to real concrete are to define and assess the fracture energy release rate of mortar–aggregate interfaces and also to quantify fracture criteria for crack path prediction.

In concrete, a crack impinging a mortar–aggregate interface has been shown to advance by either penetrating into the aggregate or deflecting along the interface [7]. Let Γ_i be the toughness of the interface as a function of $\hat{\psi}$ and let Γ_1 be the mode I toughness of the aggregate. The impinging crack is likely to be deflected if

$$\frac{\Gamma_i}{\Gamma_1} < \frac{G_d}{G_p^{max}} \tag{6.5}$$

where Γ_1 and Γ_i are material properties, which can be measured by fracture testing, and G_d is the energy release rate of the deflected crack and G_p^{max} is the maximum energy release rate of the penetrated crack. For complex geometries the ratio G_d/G_p^{max} can be calculated using numerical analyses schemes, but the ratio has been analytically computed for semi–infinite crack problems [22]. It was found that with $\alpha = 0$ and the crack approaching perpendicular to the interface, G_d/G_p is equal to approximately 1/4, indicating that in the semi–infinite crack problem the crack will deflect if the interface toughness is less than a quarter of the aggregate.

From previous testing phases, it has been repeatedly demonstrated that composite specimens with limestone aggregate have generally failed with transgranular aggregate penetration while specimens with granite aggregate have generally failed through interfacial deflection. These failure processes can be verified through application of Equation 6.5, which can be solved for the range of phase angles which will result in interfacial crack propagation during failure of the composite.

$$\Gamma_i(\hat{\psi}) < \left(\frac{G_d}{G_p^{max}}\right)\Gamma_1 \tag{6.6}$$

The results of solutions for G_d/G_p^{max} for semi–infinite crack planes with respect to elastic mismatch parameters [22] are applied with results from previous work in in-

Table 6.1: Ranges of crack tip phase angles resulting in interfacial propagation

Material combination	α	$\hat{\psi}$ for interfacial	Predicted mode of failure
Normal strength/limestone	0.108	$< 53°$	Penetration
Normal strength/granite	0.206	$< 78°$	Interfacial
High strength/limestone	0.018	$< 45°$	Penetration
High strength/granite	0.118	$< 75°$	Interfacial

terfacial fracture energy [9] to compute ranges of phase angles for different material combinations, as shown in Table 6.1. Concrete specimens with granite aggregates were calculated to have a much wider range of crack tip phase angles that result in interfacial crack propagation. Likewise, specimens with limestone were calculated to have a lower range of interfacial crack tip phase angles, indicating that failure through aggregate penetration was more likely to occur.

From Equation 6.5 it is shown that the fracture energy of the interface relative to the aggregate can shift the fracture processes in concrete from interfacial to aggregate penetration, altering the behavior of the material. However, little is known about the quantitative influence this shift and different constituent and interfacial fracture properties will have on the behavior of concrete. Furthermore, the influence of variations in the aggregate volume fraction and size on the behavior of the concrete is not widely known. For these reasons, concrete specimens with strong and weak aggregates were tested with different mortar strengths, aggregate volume fractions, and aggregate sizes to study these influences.

6.3 Experimental Procedure

6.3.1 Scope

General principles governing high strength concrete properties and fracture behavior were reviewed. Limitation on the extent of available knowledge with respect to the design of high strength concrete with improved strength, fracture energy, and ductility have also been highlighted. Specifically, issues that need to be investigated include:

1. The influence of aggregate and interfacial properties on crack propagation and ductility of high strength concrete,
2. How volume fractions and sizes of aggregates and interfacial zones will affect fracture behavior and ductility,
3. How various interfacial and aggregate properties can be adjusted to produce optimum composite performance.

To address these issues a variety of real concretes with varying constituent material properties are proposed and tested. Beam specimens consisting of varying aggregate strengths, sizes, and volume fractions are tested in three point bending. The RILEM Technical Committee 89-FMT on Fracture Mechanics of Concrete–Test Methods proposed in 1990 a recommendation to measure the material fracture toughness using a three point bending beam. These pre–notched beam specimens subjected to three–point bending have been used to measure the mode I fracture toughness and fracture energy of concrete. The beam specimens, shown in Figure 6-1 have a precrack to 1/3 the beam depth in the middle of the span. By testing these specimens the fracture energy G_f and in conjunction with tensile strengths the characteristic length l_{ch} of the material can be measured.

During fracture of the specimens, propagating cracks will impinge an aggregate inclusion and either propagate through the aggregate in transgranular faulre or deflect though the interface in interfacial failure. These different failure modes may strongly influence the fracture toughness of the concrete. Furthermore, variations in aggregate size and volume fraction may also influence the behavior of the concrete. These aspects are studied in an experimental program incorporating concrete beams under three point bending.

6.3.2 Testing Specimen

Concrete physical models were tested to study the influence of interfacial fracture characteristics, aggregate volume fraction, and aggregate size on the behavior of concrete. Beam specimens shown in Figure 6-1 were tested under three–point bending to investigate concrete fracture. The dimensions of beam specimens were 700 mm × 150 mm × 75 mm in accordance with Rilem Technical Commitee 89-FMT Test Methods. Two different mortar strengths were used with aggregates of granite and limestone in initially cracked three–point bending specimens. The properties of the materials are reported in Table 6.2. An initial crack was created in the concrete to 1/3 the depth of the beam.

The testing parameters in this study were the mortar strength, the aggregate strength, the aggregate volume fraction and the aggregate size. Coarse aggregate

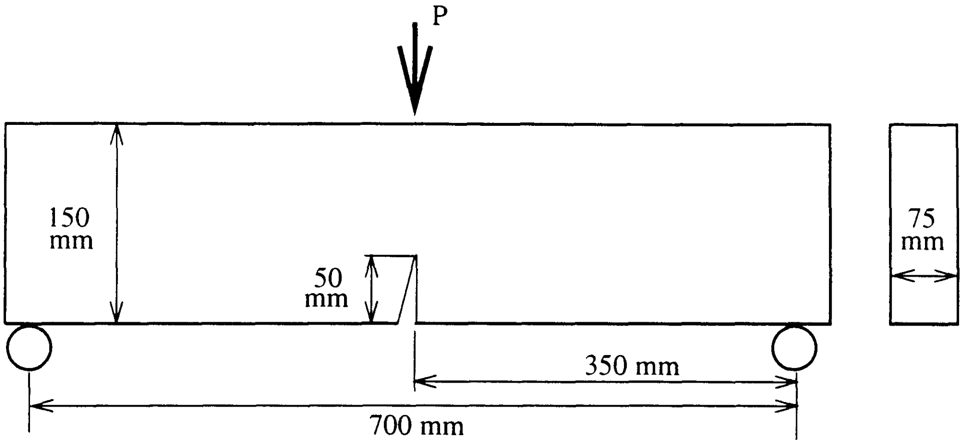

Figure 6-1: Three–point bending loading used on concrete beam specimens

volume fractions of 0.25, 0.35, and 0.45 were tested and maximum aggregate sizes of 3/8", 3/4", and 1" were also tested. All specimens were made using Type III cement to produce high early strength mortars and specimens were tested after 7 days of curing.

6.3.3 Testing Procedure

Three–point bending tests on the beam specimens were performed using an INSTRON machine with a displacement control. During the testing, the ultimate loads and load versus load–line displacement signals were recorded to measure the bending performance of the specimens. Compressive cylinders and split cylinder tests were used to measure the compressive and tensile strengths of the concrete. They were tested using a 60–kip BALDWIN testing machine shown in Figure 6-2.

Table 6.2: Material properties

Material	σ_c [MPa]	σ_t [MPa]	E [GPa]	ν	G_f [J/m^2]
Low strength mortar	40.0	2.8	27.8	0.2	39.0
High strength mortar	83.8	5.0	33.3	0.2	57.0
Granite	123.0	6.2	42.2	0.16	59.7
Limestone	57.5	3.1	34.5	0.18	29.2

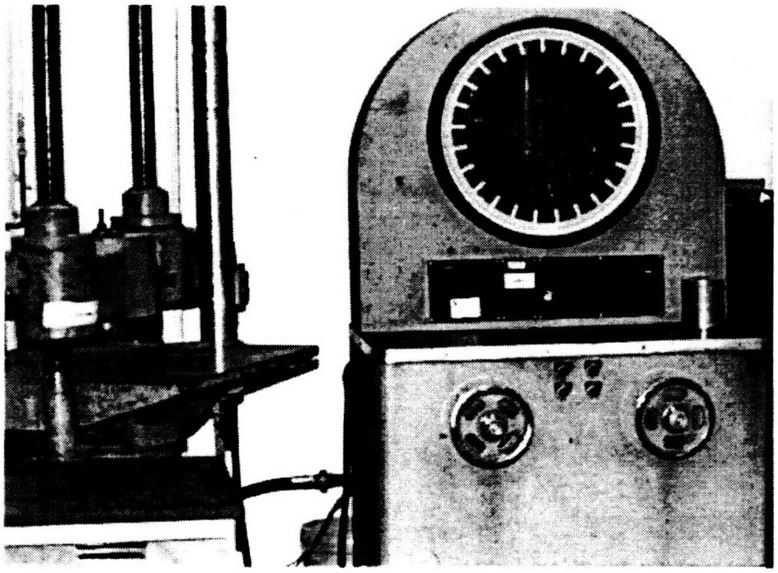

Figure 6-2: 60–kip BALDWIN machine used in the testing series

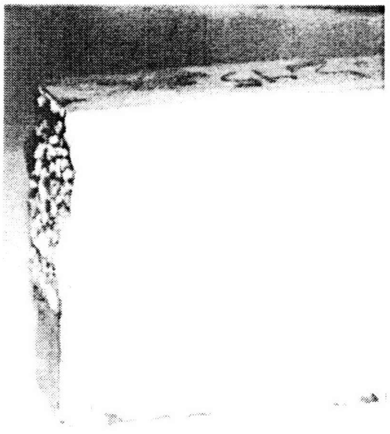

Figure 6-3: Sample specimen containing limestone

6.3.4 Results of Experimental Program

The average failure loads P_u^{avg} for the laboratory tests with normal strength mortars are reported in Table 6.3. In specimens containing limestone aggregate, failure was observed to be brittle and the crack path propagated through the limestone resulting in a planar crack face, as shown in Figure 6-3. However, specimens containing granite often displayed greater damage formation and the crack path deflected around the aggregates through the interface, resulting in a rough crack face with multiple crack paths, as shown in Figure 6-4. In general, the tensile and compressive strengths were higher for mixtures containing granite. Average failure loads for specimens with high strength mortars are reported in Table 6.4. Similar trends were observed, with brittle transgranular crack propagation through limestone aggregates and deflected crack paths through the mortar–aggregate interfaces in specimens containing granite. Higher tensile and compressive strengths were also observed in specimens with granite aggregate.

Table 6.3: Results of experimental program

Series	V_f	MSA	P_{ult}^{avg} [kN]	Failure	K_{I_c} [Pa$\sqrt{m}$]	f_t' [MPa]	f_c [Mpa]	l_{ch} [m]
Normal/limestone	0.25	3/8"	2.724	transgranular	621.9	1.92	36.0	0.1051
Normal/limestone	0.35	3/8"	2.360	transgranular	538.7	1.94	25.1	0.0772
Normal/limestone	0.45	3/8"	2.531	transgranular	577.9	2.16	27.1	0.0719
Normal/limestone	0.25	3/4"	2.953	transgranular	674.1	2.33	34.3	0.0834
Normal/limestone	0.35	3/4"	2.895	transgranular	661.0	2.69	32.7	0.0603
Normal/limestone	0.45	3/4"	2.680	transgranular	611.9	2.62	30.5	0.0544
Normal/limestone	0.25	1"	2.728	transgranular	622.9	2.29	34.2	0.737
Normal/limestone	0.35	1"	2.991	transgranular	682.9	2.61	31.0	0.0685
Normal/limestone	0.45	1"	2.969	transgranular	677.7	2.58	34.5	0.0690
Normal/granite	0.25	3/8"	3.077	interfacial	702.5	2.61	33.1	0.0727
Normal/granite	0.35	3/8"	2.744	interfacial	626.3	2.19	33.6	0.0814
Normal/granite	0.45	3/8"	2.933	interfacial	669.6	2.61	36.8	0.0658
Normal/granite	0.25	3/4"	3.287	interfacial	750.5	2.22	38.4	0.1144
Normal/granite	0.35	3/4"	3.470	interfacial	792.1	3.05	33.8	0.0676
Normal/granite	0.25	1"	2.847	interfacial	650.0	2.59	34.1	0.0628
Normal/granite	0.35	1"	3.002	interfacial	685.3	2.77	67.5	0.0612
Normal/granite	0.45	1"	2.898	interfacial	661.7	2.45	28.2	0.0727

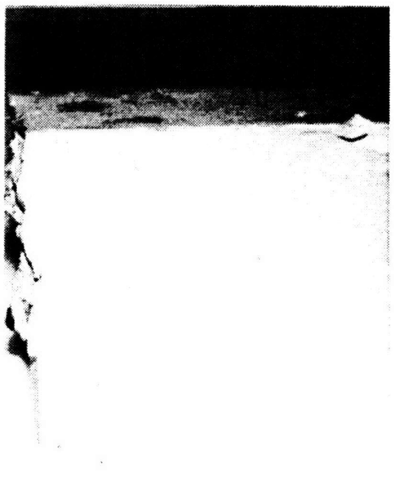

Figure 6-4: Sample specimen containing granite

Table 6.4: Results of experimental program

Series	V_f	MSA	P_{ult}^{avg} [kN]	Failure	K_{I_c} [Pa$\sqrt{m}$]	f_t' [MPa]	f_c [Mpa]	l_{ch} [m]
High/limestone	0.25	3/8"	4.007	transgranular	914.8	3.29	40.8	0.0771
High/limestone	0.35	3/8"	3.542	transgranular	808.6	2.39	49.4	0.1149
High/limestone	0.45	3/8"	3.170	transgranular	723.7	2.08	43.0	0.1214
High/limestone	0.25	3/4"	4.567	transgranular	1042.5	3.20	52.8	0.1060
High/limestone	0.35	3/4"	3.632	transgranular	829.0	2.86	42.6	0.0841
High/limestone	0.45	3/4"	4.135	transgranular	944.0	2.83	47.8	0.1109
High/limestone	0.25	1"	3.220	transgranular	735.2	3.15	43.7	0.0543
High/limestone	0.35	1"	3.243	transgranular	740.4	2.97	36.4	0.0621
High/limestone	0.45	1"	3.456	transgranular	789.1	3.12	50.4	0.640
High/granite	0.25	3/8"	3.725	interfacial	850.5	3.45	58.6	0.0607
High/granite	0.35	3/8"	4.305	interfacial	982.8	3.28	45.4	0.0898
High/granite	0.45	3/8"	4.174	interfacial	952.8	2.87	38.8	0.1101
High/granite	0.25	3/4"	3.592	interfacial	819.9	3.69	35.7	0.0494
High/granite	0.35	3/4"	3.981	interfacial	908.7	3.74	40.3	0.0591
High/granite	0.45	3/4"	3.712	interfacial	847.3	3.51	48.4	0.0583
High/granite	0.25	1"	2.961	interfacial	675.9	3.07	35.7	0.0484
High/granite	0.35	1"	3.988	interfacial	910.5	2.93	43.8	0.0964
High/granite	0.45	1"	3.336	interfacial	761.6	2.75	48.4	0.0767

Several recent works have quantified the ductility of concrete through a characteristic length, a measure proposed by Hillerborg [60, 54, 25]. This measure has also been used to quantify the ductility of glass, rocks, and other materials [60]. The characteristic length relates the fracture energy of the material to the tensile strength

$$l_{ch} = \frac{EG_F}{(f_t')^2} \tag{6.7}$$

where E, G_F, and f_t' is the Young's modulus, fracture energy, and tensile strength of the material, respectively. Equation 6.7 can be extended through the assumptions of linear elastic fracture mechanics to

$$l_{ch} = \left(\frac{K_{I_c}}{f_t'}\right)^2 \tag{6.8}$$

where K_{I_c} is the critical stress intensity, a material property derived from the three–point bending stress intensity factor

$$K_I = \frac{3SP}{2tW^2}\sqrt{a}F_I(\alpha), \qquad \alpha = a/W \tag{6.9}$$

where $F_I(1/3) = 1.08228$, a/W is the relative crack length, t is the specimen width, W is the specimen height, and S is the distance between supports [50].

The ductility of specimens with limestone aggregate was found to decrease with concrete strength, as shown in Figure 6-5(a). This trend agrees with the conclusions of other researchers [60, 54, 25]. Ductility is also shown to decrease with strength for specimens containing crushed granite as aggregate, as shown in Figure 6-5(b), but the slope of the line is significantly less than the specimens with limestone aggregate. This trend may be attributable to the differences in the fracture processes exhibited by the specimens. Specimens with limestone aggregate failed with transgranular fracture and a planar crack face while specimens with granite aggregate exhibited crack deflection resulting in rough crack faces and multiple crack paths. Fracture energy is required for these deflections and formations of multiple cracks in specimens with granite aggregate, resulting in greater ductility than in specimens with the limestone aggregate.

The effects of aggregate volume fraction on the ductility of concrete were also found to depend on the aggregate type. Concretes with limestone, shown in Figure 6-6, were found to decrease in ductility with greater volume fraction, as shown in Figure 6-7(a), while concretes with granite increased in ductility with greater volume fraction, as shown in Figure 6-7(b). This may be attributable again to the differences in fracture processes, with a greater volume fraction providing a greater limestone surface area for transgranular crack propagation. However, larger granite volume fractions increased the crack blunting by the aggregates resulting in a more tortuous crack path, absorbing more energy and resulting in greater ductility. The effect of aggregate size on the ductility of concrete was found to decrease with larger aggregate size (shown in Figure 6-9) regardless of the aggregate type, as shown in Figures 6-8(a) and (b). This trend may be caused by weaker transition zones with larger interfaces and higher probabilities of critical microflaws in larger aggregates [43].

These trends have demonstrated the sensitivity of concrete to its constituent material composition. The causes and effects of these trends were examined further in

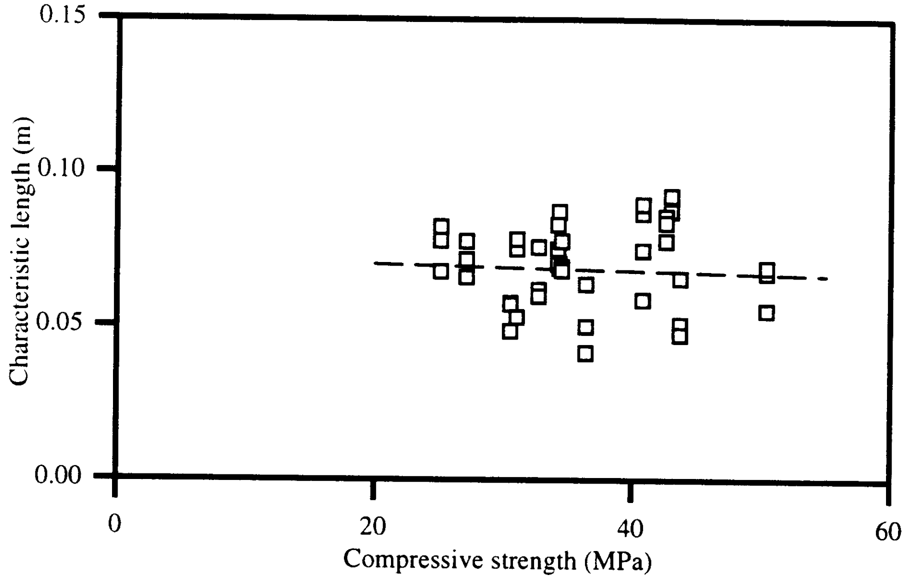

(a) Limestone aggregate

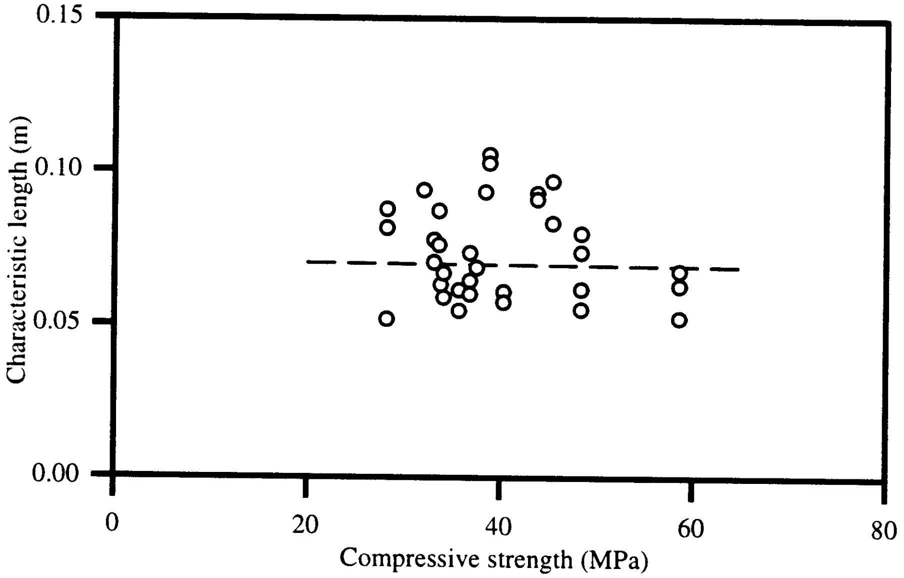

(b) Granite aggregate

Figure 6-5: Effects of concrete strength on the ductility of concrete

Figure 6-6: Specimens with varying coarse aggregate volume fraction

an analytical procedure.

6.4 Analytical Procedure

6.4.1 Correlation to Previous Work

The results of the experimental testing program have demonstrated the sensitivity of concrete fracture behavior to different constituent and interfacial fracture properties. An analytical investigation of the influence these constituent and interfacial fracture properties have on the performance of the concrete was conducted. Results of analytical models are correlated with the results from the experimental testing program.

Kitsutaka et. al. (1993) modeled concrete as a two phase composite consisting of

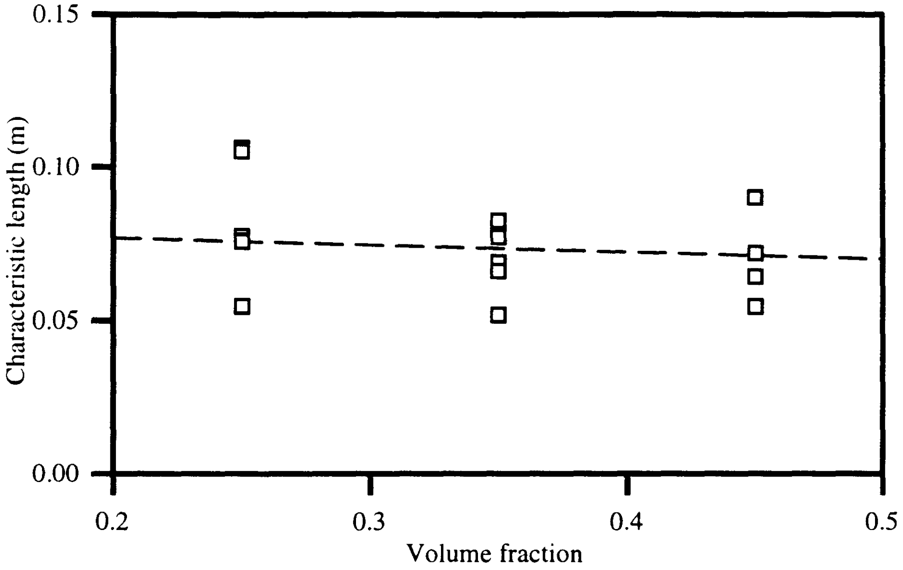

(a) Limestone aggregate

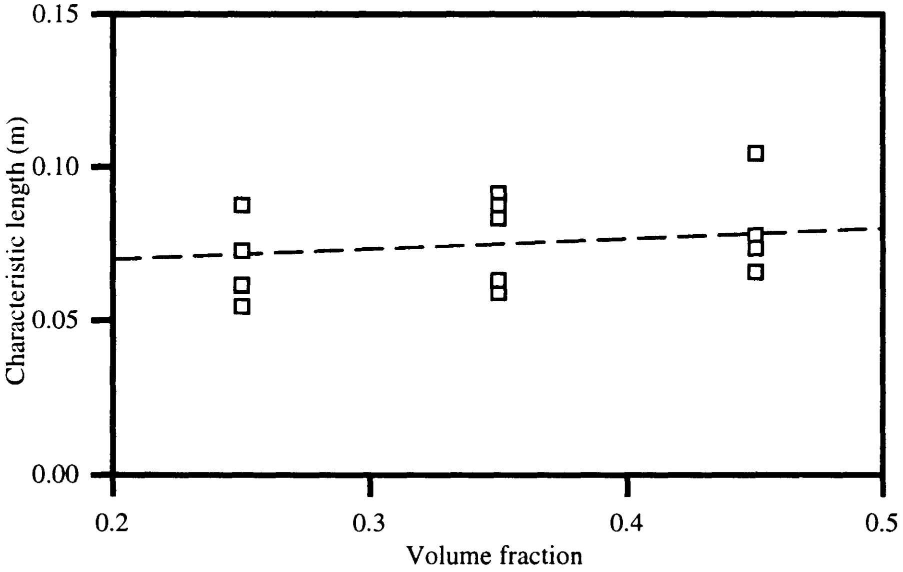

(b) Granite aggregate

Figure 6-7: Effects of aggregate volume fraction on the ductility of concrete

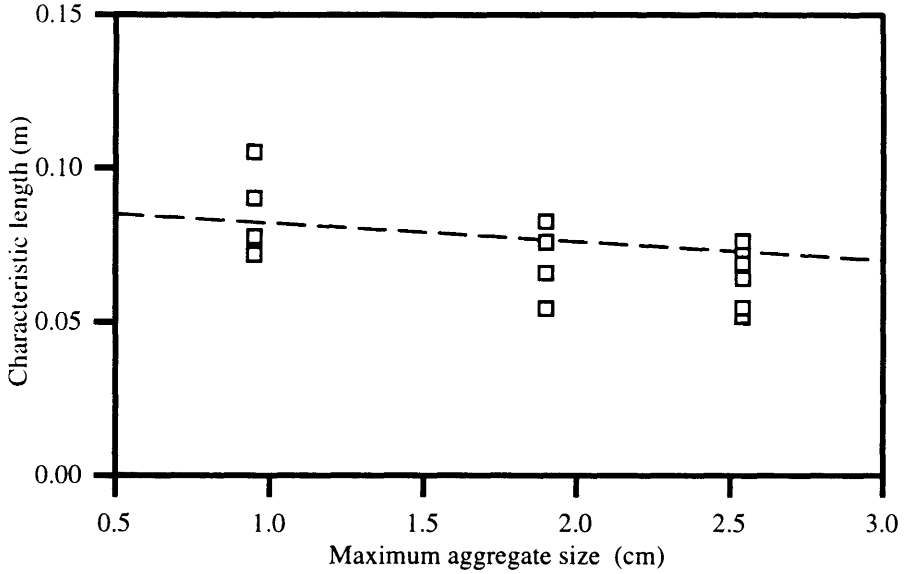

(a) Limestone aggregate

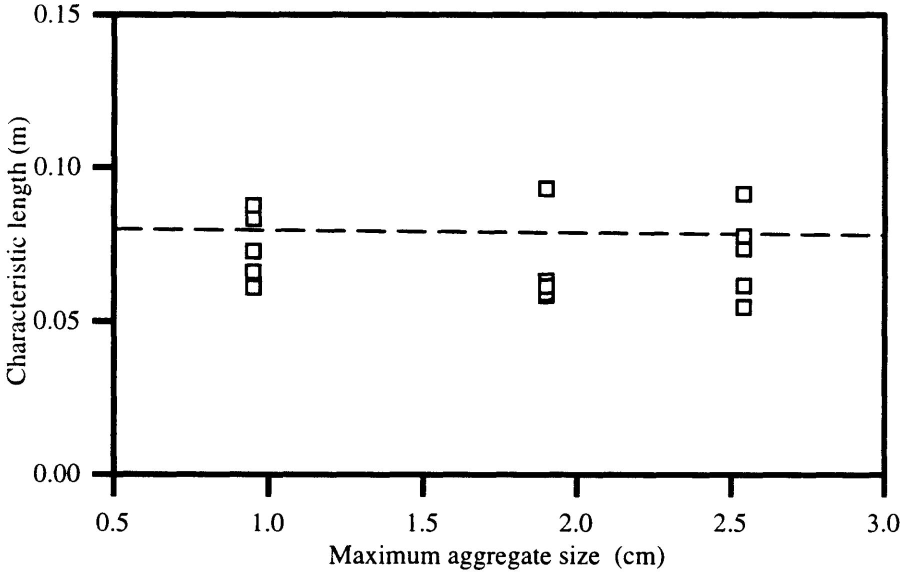

(b) Granite aggregate

Figure 6-8: Effects of maximum aggregate size on the ductility of concrete

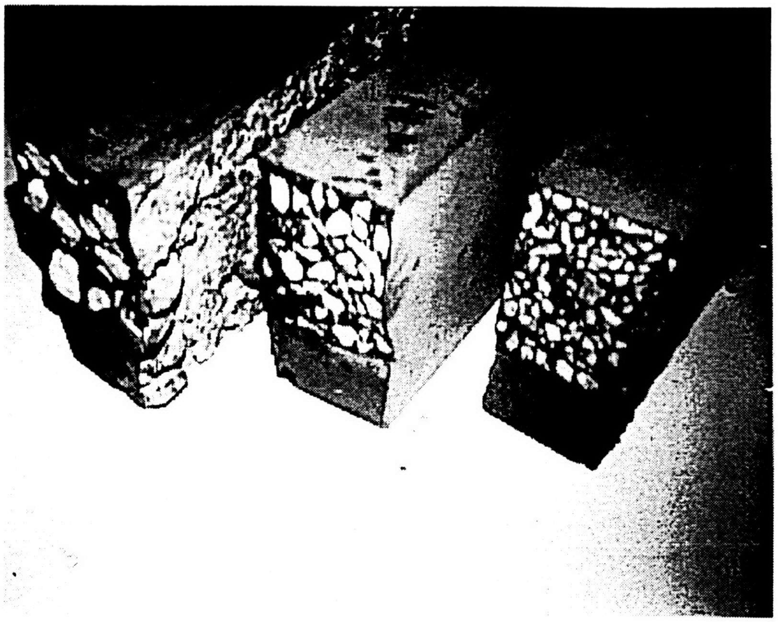

Figure 6-9: Specimens with varying maximum coarse aggregate size

mortar and two circular aggregate inclusions and investigated the transgranular cracking problem through laboratory testing of physical models with a single granite inclusion and numerical analysis using computational cohesive force models. Buyukozturk and Hearing (1996a, 1996b) studied the propagation of interfacial fracture through similar laboratory testing of physical models and numerical analysis using finite element and cohesive force models. The results of these studies led to useful information with respect to the understanding of composite model behavior as affected by interfacial and constituent fracture properties. However, the results obtained in this way are limited due to the idealization and simplifications of the composite models. Hence, there is a need to develop correlation with real concrete studies to verify the results obtained in these analytical procedures.

To correlate the results of the composite model specimens to the experimental program presented in this study it is necessary to identify similar characteristics in terms of fracture processes. As shown earlier in Table 6.1, the material combinations for the experimental specimens were subjected to the crack path fracture criteria given in Equation 6.5. This analysis is supported by the results of the testing series where specimens with granite aggregate were observed to fail through interfacial fracture and specimens with limestone failed with aggregate penetration. It is concluded that the interfacial propagation analytical model of Buyukozturk and Hearing (1996b) will be most applicable to the study of concretes made with granite while the aggregate penetration model of Kitsutaka et. al. (1993) will be most applicable to study concretes made with limestone.

These cohesive force models can be used to simulate fracture behavior in idealized composites with material parameters similar to the experimental program. Table 6.5 shows peak loads obtained with the results of these analytical simulations compared to peak loads obtained from the experimental program. The ratios of high strength mortar to normal strength mortar peak loads from the simulations are shown to agree with ratios from the experimental program. Furthermore, Figure 6-10(a) shows a comparison of load/load–line displacements obtained from cohesive force analytical simulations using normal strength and high strength mortars with a circular granite aggregate inclusion [8]. The peak load and deflection of the system with high strength mortar is shown to be greater than with normal strength mortar, agreeing with the strength and ductility results of the experimental program. Figure 6-10(b) shows a comparison of load/load–line displacements obtained with analytical simulations using normal and high strength mortars with limestone aggregate [35]. Here, the peak

Table 6.5: Comparison of parametric studies to experimental program

(a) Comparison to aggregate penetration analytical model

Material combination	Analytical load [kN]	Experimental load [kN]
High strength/limestone	1.200	3.631
Normal strength/limestone	0.893	2.771
Ratio	1.34	1.31

(b) Comparison to interfacial propagation analytical model

Material combination	Analytical load [kN]	Experimental load [kN]
High strength/granite	1.357	3.800
Normal strength/granite	1.099	3.066
Ratio	1.23	1.24

load of the system is higher with high strength mortar but the deflection is not shown to increase as in the model with granite inclusions. Based on these observations, it is concluded that strong aggregates that yield a low interface to aggregate fracture toughness ratio in Equation 6.5, such as granite, can be used to improve ductility in cementitious composites.

6.4.2 Theoretical Derivation of Composite Fracture Energy

The variety of materials available to manufacture concretes has created a need to optimize the design of concrete with desired ductility properties. The measurement of ductility through the characteristic length and similar quantities has created the need for accurate determination of fracture energy. Recently, several empirical methods to derive the fracture energy of concrete have been proposed. Among others, Hilsdorf

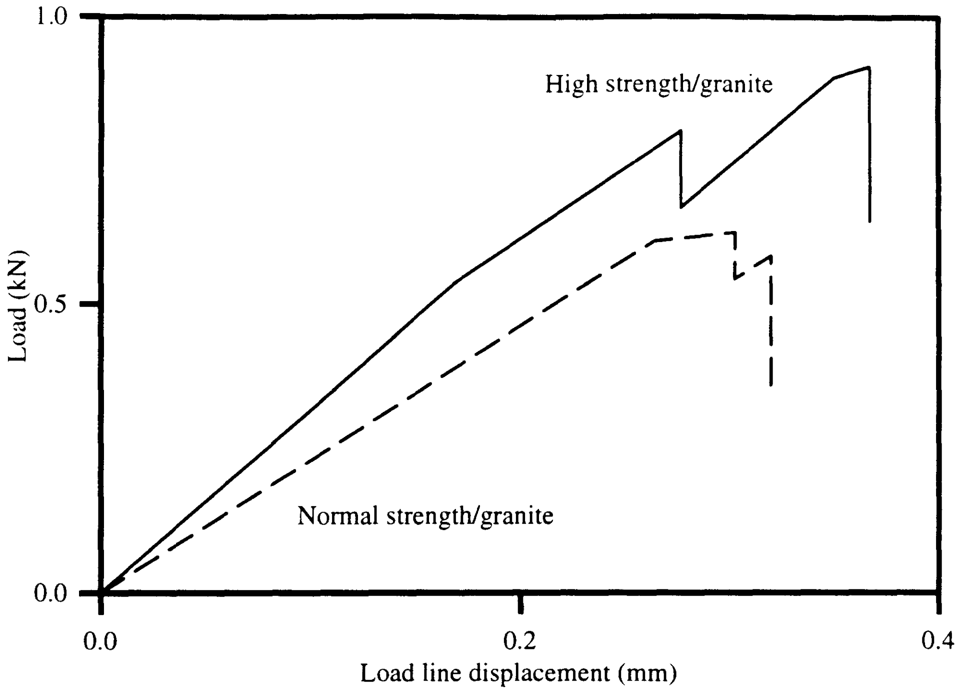

(a) Aggregate penetration model

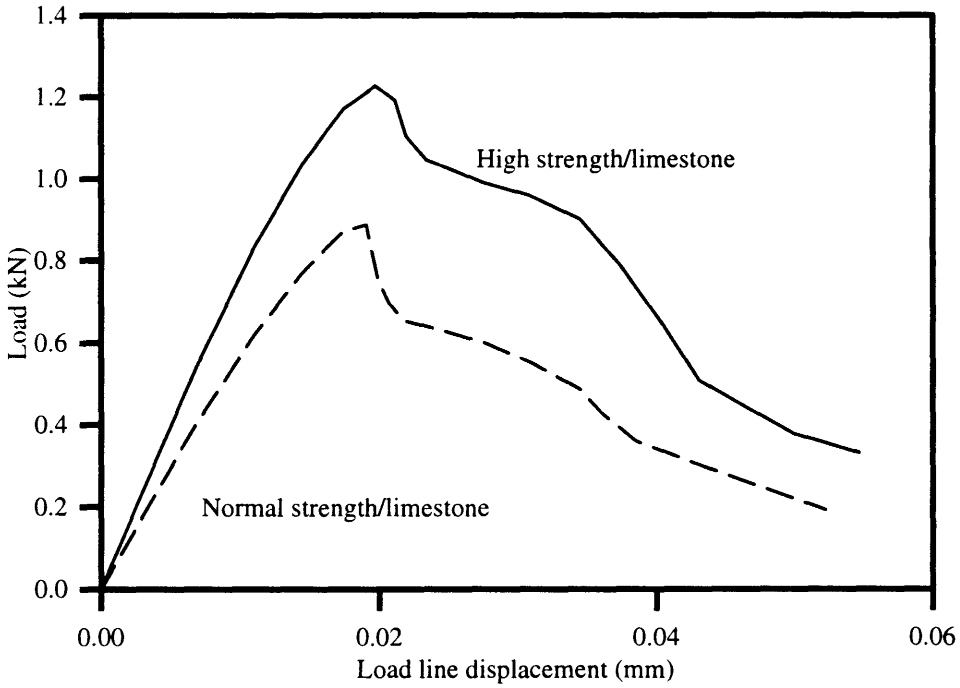

(b) Interfacial propagation model

Figure 6-10: Results of cohesive model simulations and Brameshuber (1991) have related the fracture energy to the compressive strength.

$$G_f = adf_{cm}^{0.7}$$

However, it has been shown in the study that ductility can be altered with respect to the volume fraction of the aggregate. Hence, using Equation 6.4.2 to measure ductility through a characteristic length would not reflect the influence of volume fraction. For this reason, Larrard and Malier (1992) have proposed a relation to characterize the composite behavior with respect to the aggregate volume fraction.

$$G_{I_c} = (1 - v)G_{I_m} + vG_{I_a}$$

In addition to the volume fraction, the size of the aggregate and the advent of interfacial versus transgranular fracture propagation have been shown in this study to affect the resulting fracture energy of the composite. Hence, the fracture energy empirical formula has been further developed.

To account for variations in aggregate size, a factor k_a has been introduced to Equation 6.4.2.

$$G_c = k_a \left[(1 - v)G_m + vG_a\right]$$

Furthermore, the advent of interfacial fracture has been included through the variable k_v

$$G_c = k_a k_v \left[(1 - v)G_m + vG_a\right]$$

Table 6.6: Results obtained from regression of data

Mixture	$G_c^{equation}/G_c^{experimental}$	Standard deviation
Normal strength/Limestone	1.050	0.124
High strength/Limestone	0.980	0.190
Normal strength/Granite	1.280	0.150
High strength/Granite	0.850	0.167

with $k_v = 1$ for transgranular fracture. The values of k_a and k_v have been computed using data from this experimental program [34]. Ratios of predicted values and experimental results with standard deviations are given in Table 6.4.2. Parametric studies using this equation have concluded that concretes with interfacial failure are strongly influenced by the ratio of mortar to interfacial fracture energy, confirming the results of Chapter 5. Additionally, concretes with transgranular fracture are strongly influenced by the fracture properties of the aggregate, confirming the work of Kitsutaka (1993).

6.5 Summary

Development of advanced concrete composite materials with improved toughness and ductility requires a fundamental understanding of cracking scenarios in the interfacial regions. For this purpose analysis of interface fracture and crack propagation is an essential tool. In this chapter, criteria based on energy release rate concepts are reviewed for the prediction of crack growth at the interfaces. An experimental program with concrete specimens is presented for the study of the influence of interfacial fracture properties, aggregate volume fractions, and aggregate size on the ductility of the material. An analytical procedure is conducted for comparison to analytical models and good correlation is found.

It was concluded that strong aggregates that yield a low interface to aggregate fracture toughness ratio can be used to improve ductility in cementitious materials. Furthermore, the influence of the aggregate volume fractions was shown to depend on the fracture scenario of the composite and a decreased aggregate size was shown to improve the composite ductility. The use of a fracture mechanics based methodology was concluded to be applicable to the study of interfacial regions of concrete. This study represents an initial step in using these methods to design improvements in advanced concrete composite material behavior.

Chapter 7

Summary, Conclusions, and Future Work

7.1 Summary

In this thesis, a fundamental study of the influence of mortar–aggregate interfaces on the fracture behavior and performance of concrete was conducted. The study aimed to characterize the fracture behavior of the mortar–aggregate interface, investigate the contributions of the interface to local fracture, and establish the influence of the interface on the fracture behavior of global concrete. These objectives were achieved through experimental and analytical research on two–phase composite models in various forms of physical laboratory specimens. Numerical analyses based on fracture mechanics concepts were also performed to simulate the fracture and failure processes of the specimens.

First, the mechanical properties and fracture behavior of concrete was reviewed.

Influences on the failure processes and current state of the art in characterization of concrete was examined. Mortar–aggregate interfaces were shown to strongly influence the performance of concrete during failure. The application of fracture mechanics to mortar–aggregate interfaces was examined and relevant parameters were highlighted. The oscillatory nature of the near–field stress distribution around the crack tip was discussed, and methods used to measure the interfacial fracture energy were described.

Next, previous work in the ongoing project to which this thesis contributes was reviewed. Size scale effects were shown to be applicable to mortar–aggregate interfaces in concrete composites [55]. Crack behavior approaching the interfacial region was shown to conform to crack deflection and propagation criteria [36]. Finally, interfacial parameters were shown to influence the behavior of simple block specimens under compression loading [45]. These works provided an introduction and motivation for the following work performed by the author.

In this research, novel experimental/numerical methodology based fracture mechanics studies were used to study fracture in concrete composites. Interfacial fracture tests on sandwiched beam specimens were used to derive interfacial fracture toughness K_i and energy release rate G_i parameters as an example for interface fracture in high strength concrete. Interfacial slab inclusion specimens were tested in both mode I and mixed mode loading to investigate load–displacement behavior. The fracture energy of mortar–aggregate interfaces was found to increase with increasing loading phase angles. This is in agreement with earlier findings [36]. Interfacial fracture energy was also found to increase with higher strength concretes. Additionally, interfacial fracture energy was found to increase with rougher aggregate surfaces, especially in higher loading angles. This was attributed to increased shear–slip resistance of the rougher interface.

A Hillerborg–type cohesive force analytical model was used to test different strain softening models in the simulation of the interface during fracture. The model was shown to successfully model interfacial slab inclusion specimens for interfacial propagation under mode I and mixed mode fracture. While bilinear strain–softening models have been shown to successfully model the constituent materials, a linear model was shown to best model interfacial strain–softening behavior. A linear model was also shown to be most applicable to mode II crack propagation, and interfacial ductility was shown to improve with rougher aggregate surfaces through the introduction of an interfacial characteristic length.

Following the strain–softening investigation, circular inclusion physical specimens were created with various mortar strengths and granite inclusions with both smooth and sandblasted surface roughness to investigate the influence of interfacial fracture properties on the behavior of specimens where fracture propagates through the interface. For this reason, specimens with a strong granite inclusion were tested under three point bending load to examine the deformation and fracture behavior of the different interfaces as fracture ocurred through the interface in these specimens. Fracture was observed to propagate around the granite inclusions regardless of surface roughness and mortar strength. However, differences in load–displacement behavior were observed with these different roughnesses and mortar strengths. Ductility of the composite was shown to increase with rougher aggregate surfaces but decrease with higher strength mortars.

The cohesive force analytical model was extended to simulate fracture in the circular inclusion specimens. Implemention of this model involved a finite element investigation into the stress intensities created by a crack propagating around a circular inclusion. The results of the FEM investigations were used in a cohesive type simulation of the circular inclusion specimens. The analytical model was shown to successfully simulate the laboratory circular inclusion specimens through interfacial fracture. Using the analytical model, a parametric study was conducted to investigate the influence of relative interfacial to mortar fracture energies P and relative interfacial to mortar tensile strengths T. The parametric study demonstrated that an increase in composite ductility could be realized with weaker relative interfacial to mortar fracture energy ratios. Furthermore, stronger interfacial tensile strengths were also shown to be influential in improving the ductility of concrete composites.

Based on the results of these parametric studies, an experimental program with real concrete specimens containing strong and weak aggregates with normal and high strength mortars was conducted. The influence of interfacial fracture properties, aggregate volume fractions, and aggregate size on the fracture behavior of the global material was investigated. Interfacial fracture characteristics were shown to influence the fracture processes and global behavior of real concrete. Correlation was demonstrated between results of the parameteric studies conducted earlier and the performance of the real concrete, confirming the applicability of these studies to the material design of high performance concrete. Additionally, a formula was developed to calculate the fracture energy of the concrete based on the constituent volume fractions, aggregate size, and mode of failure. It was also found that the introduction of strong aggregates with a low interface to aggregate fracture toughness ratio resulted in crack deflection through the interface during the fracture of the concrete. For higher strength concretes, this was shown to improve the ductility relative to composites failing through aggregate penetration.

Furthermore, the results of this investigation included the development of guidelines for the mix proportioning and design of concrete with optimum strength and ductility characteristics. A decrease in aggregate size; i. e. the use of smaller coarse aggregates was shown to result in higher compressive strength and greater ductility. The influence of the aggregate volume fraction was found to depend on the fracture scenario of the composite. Concretes with failure through aggregate penetration were found to decrease in ductility with greater volume fraction, while concretes that failed through interfacial deflection increased in ductility with greater volume fractions. These results are useful in the production of high strength concretes with optimum ductility behavior given geographic and physical availabilities of aggregate materials.

7.2 Conclusions

The slab inclusion testing program confirmed the results of previous researchers and helped to establish consistent laboratory techniques. Futhermore, implementation of the analytical model verified the applicability of linear elastic fracture mechanics to mortar–aggregate interfaces. This analytical model proved useful in the study of constitutive relationships, and demonstrated its usefulness as an important research tool. It was concluded from this experimental program that the linear constitutive relationship tested through the analytical model would be most useful in later stages of fracture modeling.

The circular inclusion beam specimen program demonstrated the influence of relative interfacial properties on the fracture behavior of the composite. Using the results of the first experimental procedure, the analytical model and constitutive relationship was shown to be successfully implemented to the circular inclusion specimen. In the process, the use of finite elements modified to investigate interfacial stress intensities was concluded to be an essential tool in the investigation of complex geometries. The analytical model was also useful in the parametric investigations of relative fracture properties on the behavior of the three–point circular inclusion specimen. From this work, it was concluded that the interfacial fracture energy relative to other constituent energies is an important parameter in the optimization of the material behavior.

The experimental program investigating the influence of these parameters on real concrete resulted in the most practical information concerning the design of concrete. Through the variations in the experimental parameters it was concluded that careful attention to the properties of the constituent materials is essential in the design of concrete with a desired range of characteristics. It highlighted the importance of advanced studies on real concrete as a supplement and verification of experimental models and simplified laboratory work. Finally, it is concluded that work in the area of interfacial fracture studies is a relevant and important field in the understanding of the behavior of the global material.

7.3 Recommendations for Future Work

The present research approach is based on linear elastic interfacial fracture mechanics concepts and is considered to be appropriate due to the observed linear elastic behavior and brittle failure of the interfaces. This aspect could be further investigated. Further work is needed to combine the interfacial and transgranular cohesive force models and with a propagation criteria to enable a dynamic prediction of crack paths and cohesive behavior of real concrete. A comparison should be made between the relative behavior of the two models to achieve an overall understanding of the composite as influenced by these scenarios. Size effects of the interface in relation to the size effects of the global material could also be investigated. These aspects should be continued in a comprehensive study focused on the fracture behavior of real concrete and the application of these results and modeling techniques to real concrete.

Bibliography

[1] ACI Special Committee 211. Standard practice for selecting proportions for normal, heavyweight, and mass concrete. *ACI 211.1-81*, 1981.

[2] W. Baalbaki, B. Benmokrane, O. Chaallal, and P. C. Aitcin. Influence of coarse aggregate on elastic properties of high–performance concrete. *ACI Materials Journal*, 88:499–503, October 1991.

[3] Z. P. Bažant. Size effect in pullout tests. *Journal of Engineering Mechanics*, 4:518–535, 1984.

[4] Z. P. Bažant, editor. *Mechanics of Geomaterials.* Wiley, J. and Sons, London, 1985.

[5] Z. P. Bažant and Z. Cao. Size effect in shear failure of prestressed concrete beams. *ACI Materials Journal*, 83:260–268, 1986.

[6] Z. P. Bažant and B. H. Oh. Crack band theory for fracture of concrete. *ASCE Journal of Engineering Mechanics*, 68(8):590–599, August 1983.

[7] O. Büyüköztürk. Interface fracture and crack propagation in concrete composites. In C. Huet, editor, *Micromechanics of Concrete and Cementitious Compos-*

ites, pages 203–212, Lausanne, 1993. Presses Polytechniques Et Universitaires Romandes.

[8] O. Büyüköztürk and B. Hearing. Improving the ductility of high performance concrete through mortar–aggregate interfaces. In S. L. Iyer, editor, *To appear in Proceedings for the ASCE 4th Materials Conference*, New York, NY, 1996. American Society of Civil Engineers.

[9] O. Büyüköztürk and K. M. Lee. Assessment of interfacial fracture toughness in concrete composites. *Cement and Concrete Research*, 15, 1993.

[10] O. Büyüköztürk, A. H. Nilson, and F. O. Slate. Stress-strain response and fracture of a concrete model in biaxial loading. *ACI Journal*, 68(8), 1971.

[11] O. Büyüköztürk, A. H. Nilson, and F. O. Slate. Deformation and fracture of particulate composite. *Journal of Engineering Mechanics, ASCE*, 98(6), 1972.

[12] A. Carpinteri. *Mechanical Damage and Crack Growth in Concrete.* Martinus Nijhoff Publishers, Boston, 1986.

[13] R. L. Carrasquillo, A. H. Nilson, and F. O. Slate. Microcracking and behavior of high strength concrete subject to short–term loading. *ACI Journal*, 78:179–186, May 1981.

[14] S. Chatterji and A. D. Jensen. Formation and development of interfacial zones between aggregates and portland cement pastes in cement–based materials. In J. C. Maso, editor, *Interfaces in Cementitious Composites*, pages 3–12, Toulouse, October 1992. E & FN Spon.

[15] J. D. Dewar and R. Anderson. *Manual of Ready-Mixed Concrete.* Blackie Academic & Professional, New York, 1992.

[16] A. DiTommaso. Evaluation of concrete failure. In A. Carpinteri and A. R. Ingraffea, editors, *Fracture Mechanics of Concrete.* Martinus Nijhoff Publishers, Boston, 1984.

[17] J. Dundurs. Edge–bonded dissimilar orthogonal elastic wedges. *Journal of Applied Mechanics*, 36, 1969.

[18] A. G. Evans and J. W. Hutchinson. Effects of non–planarity on the mixed mode fracture resistance of bimaterial systems. *Acta Metallurgica*, 37(3):909–916, 1989.

[19] Roger M. L. Foote, Yiu-Wing Mai, and Brian Cotterell. Crack growth resistance curves in strain–softening materials. *Journal of Mechanical Physics of Solids*, 34(6), 1986.

[20] K. Gerstle. Material behavior under various types of loading. In *Proceedings of a Workshop on High Strength Concrete*, pages 43–78. National Science Foundation, 1979.

[21] A. Goldman and A. Bentur. Bond effects in high–strength silica fume concretes. *ACI Materials Journal*, 86:440–447, 1989.

[22] M. Y. He and J. W. Hutchinson. Crack deflection at an interface between dissimilar elastic materials. *International Journal of Solids and Structures*, 25:1053–1067, 1989.

[23] B. Hillemeier and H. K. Hilsdorf. Fracture mechanics studies on concrete compounds. *Cement and Concrete Research*, 7(5), 1977.

[24] A. Hillerborg, M. Modéer, and P.-E. Petersson. Analysis of crack formation and crack growth in concrete by means of fracture mechanics and finite elements. *Cement and Concrete Research*, 6(6), 1976.

[25] H. K. Hilsdorf and W. Brameshuber. Code–type formulation of fracture mechanics concepts for concrete. *International Journal of Fracture*, 51:61–72, 1991.

[26] T. T. Hsu, F. O. Slate, G. M. Sturman, and G. Winter. Microcracking of plain concrete and the shape of the stress-strain curve. *ACI Journal*, 60(2), 1963.

[27] Gao Hua, M. W. Brown, and K. J. Miller. Mixed–mode fatigue thresholds. *Fatigue of Engineering Materials and Structures*, 5(1), 1982.

[28] Q. J. Huang. *Micromechanical Modelling of the Fracture Behavior of Second–Phase Concrete and the Shape of the Stress–Strain Curve.* PhD thesis, Massachusetts Institute of Technology, 1990.

[29] J. W. Hutchinson. Mixed mode fracture mechanics of interfaces. In M. Ruhle, A. G. Evans, M. F. Ashby, and J. P. Hirth, editors, *Metal–Ceramic Interfaces*, pages 295–306. Pergamon Press, New York, 1990.

[30] Y. S. Jenq. Non–linear fracture behavior of multi–phase materials. *Cement and Concrete Composites*, 13:79–86, 1991.

[31] Y. S. Jenq and S. P. Shah. Two parameter fracture model for concrete. *ASCE Journal of Engineering Mechanics*, 111(10):1227–1241, 1985.

[32] Y. S. Jenq and S. P. Shah. Two parameter fracture model for concrete. *ASCE Journal of Engineering Mechanics*, 111(10):1227–1241, 1985.

[33] R. John and S. P. Shah. Fracture mechanics analysis of high strength concrete. *ASCE Journal of Materials*, 1:185–198, 1989.

[34] Jeffrey Karam. Fracture in high strength concrete. Master's thesis, Massachusetts Institute of Technology, 1997.

[35] Yoshinori Kitsutaka, Oral Büyüköztürk, and Kwang Myong Lee. Fracture behavior of high strength concrete composite models. *Submitted to ACI Journal of Materials*, 1993.

[36] K. M. Lee. *A Study of Fracture Behavior in High Strength Concrete.* PhD thesis, Massachusetts Institute of Technology, 1993.

[37] K. M. Lee and O. Büyüköztürk. Fracture mechanics parameters influencing the mechanical properties of high performance concrete. In *Proceedings of the Second International ACI Conference on High Performance Concrete*, pages 491–498, Singapore, 1994.

[38] K. M. Lee, O. Büyüköztürk, and A. Oumera. Fracture analysis of mortar–aggregate interfaces in concrete. *ASCE Journal of Engineering Mechanics*, 118(10), 1991.

[39] T. C. Y. Liu, A. H. Nilson, and F. O. Slate. Stress-strain response and fracture of concrete in uniaxial and biaxial compression. *ACI Journal*, 69(5), 1972.

[40] J. LLorca and M. Elices. A simplified model to study fracture behavior in cohesive materials. *Cement and Concrete Research*, 20(1), 1990.

[41] A. K. Maji, J. Wang, and C. V. Cardiel. Fracture mechanics of concrete, rock, and interface. *International Journal of Fracture*, 1985.

[42] B. M. Malyshev and R. C. Salganik. The strength of adhesive joints using the theory of cracks. *International Journal of Fracture*, 5:114–128, 1965.

[43] P. K. Mehta and P. C. Aitcin. Microstructural basics of selection of materials and mix proportions for high–strength concrete. In W. T. Hester, editor, *High–Strength Concrete*, pages 265–286, Berkeley, California, May 1990. ACI SP–121, Second International Symposium on Utilization of High Strength Concrete.

[44] Edward G. Nawy. *Reinforced Concrete*. Prentice Hall International, 1990.

[45] Ayad Oumera. Crack propagation in the aggregate–mortar interface regions of concrete. Master's thesis, Massachusetts Institute of Technology, 1991.

[46] J. R. Rice. Elastic fracture concepts for interfacial cracks. *Journal of Applied Mechanics*, 55:98–103, 1988.

[47] S. P. Shah and R. Sankar. Internal cracking and strain–softening response of concrete under uniaxial compression. *ACI Materials Journal*, 84(3), 1987.

[48] S. P. Shah and G. Winter. Inelastic behavior and fracture of concrete. In *Causes, mechanism, and control of cracking in concrete.* SP-20, American Concrete Institute, 1966.

[49] Surendra P. Shah, Stuart E. Swartz, and Chengsheng Ouyang. *Fracture Mechanics of Concrete.* John Wiley and Sons, Inc., 1995.

[50] John E. Srawley. Wide range stress intensity factor expressions for ASTM E 399 standard fracture toughness specimens. *International Journal of Fracture*, 12, 1976.

[51] H. Stang, Z. Li, and S. P. Shah. Pullout problem: Stress versus frature mechanical approach. *Journal of Engineering Mechanics*, 116(10), 1990.

[52] L. Struble, J. Skalny, and S. Mindess. A review of the cement–aggregate bond. *Cement and Concrete Research*, 10(2), 1980.

[53] Z. Suo and J. W. Hutchinson. Sandwich test specimen for measuring interface crack toughness. *Materials Science and Engineering*, A107, 1989.

[54] C. Tasdemir and M. A. Tasdemir. Effects of silica fume and aggregate size on the brittleness of concrete. *Cement and Concrete Research*, 26(1):63–68, 1996.

[55] Uwe Trende. Interface fracture of high strength concrete: Size effect and aggregate roughness. Master's thesis, Massachusetts Institute of Technology, 1995.

[56] Uwe Trende and Oral Büyüköztürk. Size effect and influence of aggregate roughness in interface fracture of concrete composites. *Accepted for publication in ACI Journal of Materials*, 1995.

[57] K. J. Wang, C. L. Hsu, and H. Kao. Calculation of stress intensity factors for combined mode bend specimens. *Proceedings of ICF 5*, 2, 1977.

[58] E. Yamaguchi and W.-F. Chen. Microcrack propagation study of concrete under compression. *Journal of Engineering Mechanics, ASCE*, 117(3), 1991.

[59] M. H. Zhang and O. E. Gjorv. Microstructure of the interfacial zone between lightweight aggregate and cement paste. *Cement and Concrete Research*, 20:610–618, 1990.

[60] F. P. Zhou, B. I. G. Barr, and F. D. Lydon. Fracture properties of high strength concrete with varying silica fume content and aggregates. *Cement and Concrete Research*, 25(3):543–552, 1995.

Appendix A

Cohesive Simulation Script

This script was used with MATLAB to simulate mixed mode propagation in sandwich specimens with variations in material properties and constitutive behavior.

```
% This is a script for introductory functions
    clear all;
    global FINITE
    disp('Now in Introfunctions')
    n = 20;
    spo = ao/n;
    sp = (d-ao)/n;
    ae(1) = ao + sp;
    ac(1) = ae(1) - sp/2;
    for k = 2:n
    ae(k) = ae(k-1) + sp;
    ac(k) = ae(k)-sp/2;
    end

    E1 = 29200;
    G1 = E1/(2*(1+0.22));

    for j = 1:n
    a = ae(j)/d;
    FVALI = ffunci(a);
    FI(j) = FVALI;
    FVALII = ffuncii(a);
    FII(j) = FVALII;
    for k = 1:j
    b = ac(k)/ae(j);
    GVAL = gfunc(a,b);
    G(j,k) = GVAL;
    GVALII = gfuncii(ae(j),ac(k));
    GII(j,k) = GVALII;
    end
    end

    VDPOI = 0;
    VDPOII = 0;
    DVOI = 0;
    DVOII = 0;

    for k = 1:ao/spo
    a = k*spo/d;
    FVALI = ffunci(a);
    FVALII = ffuncii(a);
    DVI = (FVALI2̂)/E1;
    DVII = (FVALII2̂)/G1;
    INTVDI = spo*(DVOI+DVI)/2;
    INTVDII = spo*(DVOII+DVII)/2;
    VDPOI = VDPOI+INTVDI;
    VDPOII = VDPOII+INTVDII;
    DVOI = DVI;
    DVOII = DVII;
    end

    VDPOI = (VDPOI*1.6*25.4/(d1̂.5)) + (s2̂)/(6*E1*d);
    VDPOII = (VDPOII/(d0̂.5));

    INTVPOI = DVOI;
    INTVPOII = DVOII;
    INTVROI = zeros(n,1);
    INTVROII = INTVROI;
    VDROI = INTVROI;
    VDROII = VDROI;

    for i = 1:n

    % KPI and KPII

    KPI(i) = FI(i);
    KPII(i) = FII(i);

    % VDPI and VDPII

    INTVPI = (FI(i)2̂)/E1;
    DVDPI = (1.6*25.4/(d1̂.5))*sp*(INTVPOI+INTVPI)/2;
    VDPI(i) = VDPOI + DVDPI;
    VDPOI = VDPI(i);
    INTVPOI = INTVPI;

    INTVPII = (FII(i)2̂)/G1;
    DVDPII = (1/(d0̂.5))*sp*(INTVPOII+INTVPII)/2;
    VDPII(i) = VDPOII + DVDPII;
    VDPOII = VDPII(i);
    INTVPOI = INTVPII;

    % VDRI, VDRII, and KR

    for k = 1:i
    KRI(i,k) = (2*sp/(3.14159*ae(i))0̂.5)*G(i,k);

    KRII(i,k) = 2*sp*((ae(k))0̂.5)*GII(i,k)/(3.141590̂.5);

    INTVRI = FI(i)*G(i,k)/E1;
    DVDRI = (2*1.6*25.4/(((3.14159*ae(i))0̂.5)*(d1̂.5)))*(sp2̂)*(INTVROI(k)+INTVRI)
    VDRI(i,k) = VDROI(k)+DVDRI;
    VDROI(k) = VDRI(i,k);
    INTVROI(k) = INTVRI;

    INTVRII = FII(i)*GII(i,k)*((ae(i))0̂.5)/G1;
    DVDRII = (2/((3.141590̂.5)*(d0̂.5)))*(sp2̂)*(INTVROII(k)+INTVRII)/2;
    VDRII(i,k) = VDROII(k)+DVDRII;
    VDROII(k) = VDRII(i,k);
    INTVROII(k) = INTVRII;
    end
    end



    % Mixed mode crack propagation simulation. Brian Hearing
3/95
    clear all
    figure(1);
```

```
    clg;
    %figure(2);
    %clg;

    global KPI KRI INTCPOI CPOI INTCROI INTCROII CROI
CROII HI E1 ae ac
    global sp FINITE ao s d t FI G KPII INTCPOII CPOII G1
FII GII KRII

    ao = 25; % Specimen dimensions (mm)
    s = 225;
    d = 75;
    t = 25;

    %*** Mode I interfacial properties ***

    %FtI = 2.040424; % M3/Smooth
    %GfI = 2.946159; % M3/Smooth
    %FtI = 1.594395; % M1
    %GfI = 1.798901; % M1
    FtI = 2.036704; % M3/Sand
    GfI = 2.935426; % M3/Sand
    %FtI = 1.194494; % M2
    %GfI = 1.009679; % M2

    %*** Mode II interfacial properties ***

    %FtII = 0.425088; % M3/Smooth
    %GfII = 0.212342; % M3/Smooth
    %FtII = 0.332166; % M1
    %GfII = 0.129654; % M1
    FtII = 0.424313; % M3/Sand
    GfII = 0.211568; % M3/Sand
    %FtII = 0.248853; % M2
    %GfII = 0.072772; % M2

    E1 = 29200; % M1 Modulus
    v = 0.22; % M1 Poisson's
    G1 = E1/(2*(1+v)); % Shear Modulus

    MGW = (2.2*d*t*s/1000000)*0.5*9.8; % Self-weight term
    FINITE = 0.984; % Convergence tolerance
    n = 20; % Number of discretized steps

    disp('You must have run Introfunctions.m before this.')
    load Stan.mat % Load in the introductory functions

    sp = (d-ao)/n; % Spacing of each discretized step

    % — Introduction —

    INTCPOI = zeros(n,1);
    CPOI = zeros(n,1);

    INTCPOII = INTCPOI;
    CPOII = CPOI;

    INTCROI = zeros(n);
    INTCROII = INTCROI;
    CROI = zeros(n);
    CROII = CROI;

    alpha = 0.333; % Bilinear tension softening
    beta = 0.16; % parameters

    %***** MODE I *****

    % — Bilinear Properties —

    %WCI = 2*GfI/FtI/(alpha + beta)/1000; % Bilinear Critical
width
    %WMI = WCI*beta; % Bilinear Data
    %M1I = FtI * (1-alpha)/beta/WCI; % Zone 1, Bilinear
    %N1I = FtI;
    %M2I = FtI * alpha / (1-beta) / WCI; % Zone 2
    %N2I = FtI * alpha / (1-beta);
    %M3I = 0; % Zone 3
    %N3I = 0;

    % — Linear Properties —

    WCI = 0;
    WMI = 2*GfI/(FtI*1000);
    M1I = FtI/WMI;
    N1I = FtI;
    M3I = 0;
    N3I = 0;

    %***** MODE II *****

    alpha = 0.333;
    beta = 0.16;

    % — Bilinear Properties —

    input('Linear (l) or Bilinear (b)','s');
    if ans == 'b'

    WCII = 2*GfII/FtII/(alpha + beta)/1000; % Bilinear Criti-
cal width
    WMII = WCII*beta; % Bilinear Data
    M1II = FtII * (1-alpha)/beta/WCII; % Zone 1, Bilinear
    N1II = FtII;
    M2II = FtII * alpha / (1-beta) / WCII; % Zone 2
    N2II = FtII * alpha / (1-beta);
    M3II = 0; % Zone 3
    N3II = 0;

    % — Linear Properties —
    elseif ans == 'l'

    WCII = 0;
    WMII = 2*GfII/(FtII*1000);
    M1II = FtII/WMII;
    N1II = FtII;
    M3II = 0;
    N3II = 0;
    end

    % — MAIN PROGRAM —

    for i = 1:n

    % ***** MODE I *****

    HI = hfunci(i);

    IT = 0;
    if i ¿ 1
    MI(i) = MI(i-1);
    NI(i) = NI(i-1);
    else
    MI(1) = M1I;
    NI(1) = N1I;
    end

    iter = 0;

    while IT == 0
    iter = iter + 1;
    IT = 0;
    for l = 1:i
    SUM = 0;
    for c = 1:i
    if c == l PLUS = 1;
    else PLUS = 0;
    end
    A(l,c) = MI(c) * HI(l,c) + PLUS;
    SUM = NI(c) * HI(l,c) + SUM;
    end
    C(l) = SUM;
    end

    BI = inv(A) * C'; % Simultaneous equation solution

    SUMI = 0;
    for L = 1:i
    if BI(L) ¡ WMI
    MEVI = M1I;
    NI(L) = N1I;
    else if BI(L) ¡ WCI
    MEVI = M2I;
    NI(L) = N2I;
    else MEVI = M3I;
    NI(L) = N3I;
    end
    end
    if abs(MEVI-MI(L)) ¡ 0.001 SUMI=SUMI+1;
    else MI(L) = MEVI;
    end
    end

    if SUMI == i IT = 1;
    end

    if iter ¿ 15 IT = 1;
    disp('I Hung up.')
    end
    end
    % ***** MODE II *****

    HII = hfuncii(i);
```

```
IT = 0;
if i ¿ 1
MII(i) = MII(i-1);
NII(i) = NII(i-1);
else
MII(1) = M1II;
NII(1) = N1II;
end

iter = 0;

while IT == 0
IT = 0;
for l = 1:i
SUM = 0;
for c = 1:i
if c == l PLUS = 1;
else PLUS = 0;
end
A(l,c) = MII(c) * HII(l,c) + PLUS;
SUM = NII(c) * HII(l,c) + SUM;
end
C(l) = SUM;
end

BII = inv(A) * C'; % Simultaneous equation solution

SUMI = 0;
for L = 1:i
if BII(L) ¡ WMII
MEVII = M1II;
NII(L) = N1II;
else if BII(L) ¡ WCII
MEVII = M2II;
NII(L) = N2II;
else MEVII = M3II;
NII(L) = N3II;
end
end
if abs(MEVII-MII(L)) ¡ 0.001 SUMI=SUMI+1;
else MII(L) = MEVII;
end
end

if SUMI == i IT = 1;
end
iter = iter +1;
if iter¿15 IT = 1;
disp('II Hung up.')
end
end

% — CRACK OPENING DISPLACEMENTS —

for L = 1:i
CODI(i,L) = BI(L); % Crack opening displacement
CFI(i,L) = -MI(L)*BI(L)+NI(L); % Cohesive stress (center
point)
CODII(i,L) = BII(L);
CFII(i,L) = -MII(L)*BII(L)+NII(L);
end
% — LOAD —

SUMI = 0;
SUMII = 0;
for k = 1:i
SUMI = SUMI + CFI(i,k)*KRI(i,k);
SUMII = SUMII + CFII(i,k)*KRII(i,k);
end

SIGI = SUMI/KPI(i);
SIGII = SUMII/KPII(i);
PI(i) = (((2*(d1̂.5)/(1.6*25.4))*SIGI)-MGW)*0.0254;
if PI(i) ¡ 0.0 PI(i) = 0.0;
end
PII(i) =(((2*(d0̂.5))*SIGII)-MGW)*0.0254;
P(i) = PI(i) + PII(i);

% — VERTICAL DEFORMATION —
SUMI = 0;
SUMII = 0;
for k = 1:i
SUMI = SUMI + CFI(i,k)*VDRI(i,k);
SUMII = SUMII + CFII(i,k)*VDRII(i,k);
end

VDI(i) = (SIGI*VDPI(i)-SUMI);
if VDI(i) ¡ VDI(i-1)
VDI(i) = VDI(i-1);
end
VDII(i) = (SIGII*(VDPII(i))-SUMII);

VD(i) = VDI(i) + VDII(i);
VD(i) = VD(i) * 0.0254;

% — PLOTS —
if i ¿ 1
VDplot = VD(i-1);
Pplot = P(i-1);
else
VDplot = 0;
Pplot = 0;
end

figure(1);
hold on;
if i ¿ 1
plot([BIold BI(1)],[CFII(i-1,1) CFII(i,1)],'g');
plot([BIold BI(1)],[CFI(i-1,1) CFI(i,1)],'r');
end

text(VD(i),P(i),int2str(i))
BIold = BI(1);

if CFII(i,1) == 0
stop
end
end
```